Very high energy gamma ray observations of southern hemisphere blazars

Mark R. Dickinson

Very High Energy Gamma Ray Observations of Southern Hemisphere Blazars

Mark R.Dickinson, B.Sc.

Ph.D. Thesis, University of Durham, 1997

Abstract

This thesis is concerned with very high energy γ-ray observations of blazars observable from the southern hemisphere. The data presented were obtained using the recently deployed University of Durham Mark 6 high sensitivity Čerenkov telescope. Chapters 1 and 2 are introductory; the subjects of γ-ray astronomy, extensive air showers, Čerenkov light production, the development of the atmospheric Čerenkov technique and the current status of TeV astronomy are discussed. Chapter 3 introduces the telescopes operated by the University of Durham. The Mark 6 telescope, designed to have a low threshold energy and a high resolution imaging system, is discussed in detail. Chapter 4 presents the calibration and analysis techniques routinely applied to data obtained with the Mark 6 telescope. The chapter concludes with a set of moment parameter selections designed to reject a significant fraction of the cosmic ray cascades, while retaining the majority of γ-rays cascades. These selections have resulted in a 5σ detection of PSR 1706-44. Chapter 5 discusses active galactic nuclei and in particular blazars. Topics included are recent high energy observations; the differences between the radio/X-ray selected BL Lacs and flat spectrum radio quasars; the infrared background; high energy flux variability and γ-ray production mechanisms within these objects. The chapter concludes with a list of possible very high energy γ-ray emitting blazars observable with the Mark 6 Čerenkov telescope. Chapter 6 presents the results from four of these very high energy γ-ray blazar candidates; PKS 0548-322, PKS 1514-24, PKS 2005-489 and PKS 2155-304. There is no evidence for γ-ray emission from these sources, either in the form of a steady flux or variable activity. Three sigma integral flux upper limits above 300 GeV are produced for these objects and the implications of these observations are discussed. The conclusions are presented in Chapter 7 as well as ideas for future work.

Very High Energy Gamma Ray Observations of Southern Hemisphere Blazars

Mark R.Dickinson, B.Sc.

A thesis submitted to the University of Durham in accordance with the regulations for admittance to the degree of Doctor of Philosophy.

Department of Physics
University of Durham

October 1997

Contents

1 Gamma Ray Astronomy **1**

1.1 Introduction 1

1.2 γ-Rays Production Mechanisms 2

1.2.1 Elementary Particle Decay 3

1.2.2 Synchrotron Radiation 4

1.2.3 Bremsstrahlung Radiation 4

1.2.4 Inverse Compton Scattering 4

1.2.5 Curvature Radiation 6

1.3 VHE γ-Ray Attenuation Mechanisms 6

1.4 Gamma Ray Detection Techniques 9

1.4.1 Low - High Energy (0.511 MeV $\rightarrow$ 30 GeV) 9

1.4.2 VHE energy (30 GeV $\rightarrow$ 50 TeV) 13

1.4.3 Ultra High Energy ($>$ 50 TeV) 13

1.5 Summary 14

2 EAS, Čerenkov Radiation and TeV Astronomy **15**

2.1 Introduction 15

2.2 Development of Extensive Air Showers 16

2.2.1 Photon Initiated Showers 16

2.2.2 Hadronic Initiated Showers 20

2.2.3 Differences between photon and hadron initiated EAS 23

2.3 Čerenkov Radiation 24

2.3.1 Čerenkov Radiation from EAS 27

2.3.2 Lateral Distribution 29

2.3.3 Images of Čerenkov Radiation from EAS 31

2.4 TeV Telescopes 32

2.4.1 Design Principles 34

2.4.2 Current VHE γ-Ray Experiments 37

2.4.3 Current TeV γ-Ray Source Catalogue 37

2.5 Summary 39

3 The University of Durham Atmospheric Čerenkov Telescopes **41**

3.1 The Bohena Site 41

3.1.1 Timekeeping 42

3.2 Mirror Construction and Properties 43

3.3 The Mark 3 Telescope 45

3.4 The Mark 5 Telescope 46

3.5 The Mark 6 Telescope 46

3.5.1 Detector Packages 47

3.5.2 Electronics and Trigger Criteria 49

3.5.3 Steering 50

3.5.4 Environmental Monitoring and Telescope Performance Stability 53

3.5.5 Data Treatment 55

3.6 Observing Techniques 55

3.7 Threshold Energy Determination 56

4 Calibration and Analysis Techniques **60**

4.1 Data Calibration 60

4.1.1 Pedestal Determination 61

4.1.2 Software Padding 62

4.1.3 PMT Gain Determination 64

4.1.4 Steering Offset 65

4.2 EAS Imaging 67

4.2.1 Moment Analysis 68

4.2.2 Bivariate Gaussian Fitting 70

4.3 Analysis Of DC Emission 75

4.4 Searching For Pulsed Emission 75

4.4.1 Phase Sensitive Analysis 77

4.5 Parameter Selections 79

4.6 Summary 82

5 γ-Ray Production in Blazars **83**

5.1 Introduction 83

5.1.1 EGRET Observations 84

5.1.2 Review of Previous TeV Detections 87

5.2 Infrared Attenuation 91

5.3 Blazar Characteristics 94

5.3.1 BL Lacs and OVV Quasars 95

5.3.2 X-Ray and Radio Selected BL Lacs 97

5.4 Production Mechanisms 103

5.4.1 Synchrotron Self Compton 103

5.4.2 External Compton 104

5.4.3 Hadronic Production 105

5.4.4 Example Model 107

5.5 Blazar Variability 113

5.5.1 TeV Variability 115

5.6 Southern Hemisphere Candidate Sources 121

6 Blazar Observations **124**

6.1 Introduction 124

6.2 Observations 125

6.2.1 PKS2005-489 125

6.2.2 PKS2155-304 131

6.2.3 PKS0548-322 136

6.2.4 PKS1514-24 140

6.3 Interpretation of these Observations 144

7 Summary and Future Work **148**

7.1 Summary 148

7.2 Future Work 150

7.2.1 Southern Hemisphere Blazars 150

7.2.2 PSR 1706-44 150

7.2.3 Simulations 151

7.2.4 Hardware Upgrades 151

8 References **154**

Preface

All of the work described in this thesis has been associated with the atmospheric Čerenkov telescopes in operation at the University of Durham Gamma Ray Observatory in Narrabri, New South Wales, Australia.

The author took part in six observing sessions using these telescopes. Each session lasted three weeks. Whilst at this site he undertook a number of telescope upgrades, which included the installation of opaque shielding surrounding the superstructure of the Mark 6 telescope, thereby reducing the amount of ambient light detected by the photomultipliers; the fitting of a torque limiter to the Mark 6 azimuth drive system which is designed to stop damage from excessive forces; the extension of the Ethernet site network to allow improved data transfer between the Mark 6 and Mark 5 telescopes. The author also made a number of measurements of the point spread function of the central Mark 6 mirror. This measurement has been of particular importance in the development of appropriate imaging criteria. In addition, he carried out a set of experiments to investigate methods of reducing the loss of duty cycle through freezing mirrors during the winter months. This was primarily tested with the application of fans fitted to the Mark 6 superstructure. During the observing runs, the author collected data from a variety of objects, including pulsars, X-ray binaries, AGNs and cataclysmic variables using all three Čerenkov telescopes operated by the University of Durham.

In Durham, the author was involved in a number of aspects of data pre-processing, calibration and analysis. He studied the effect of various calibration methods on the image parameter distributions. In particular, he has investigated variations in the Mark 6 telescope triggering performance during observations and the subsequent systematic biases, if any, introduced when performing event parameter selections. Factors under investigation included temperature variations (both of a diurnal nature and that produced within the detectors during operation), condensation, ambient illumination and the effect of relative movement of the three detector packages. He also played an important role in the updating of the telescope position

reconstruction software, to enable the use of the 14 bit shaft encoder information recorded within each event. The use of this information has enabled an improvement of greater than a factor of four in the calculated telescope pointing position to be obtained. This accurate pointing information has been of particular importance when using the orientation of Čerenkov images as possible evidence for very high energy γ-ray emission.

The author has analysed the data from a large number of objects. In particular he has been involved in the development of a set of moment parameter selections applicable to data obtained with the Mark 6 telescope. These parameter selections were designed to reject a large fraction of the background events while retaining the majority of any γ-rays present. This has involved the study of results produced from recent Monte Carlo simulations of the Mark 6 telescope and the analysis of data obtained from the γ-ray emitting pulsar, PSR 1706-44.

The author undertook an extensive study to search for possible extragalactic very high energy γ-ray sources observable from the southern hemisphere. This study involved the combination of both recent published observations (including results which are publicly available via the Internet) and theoretical models. This work revealed a number of X-ray selected BL Lacs as strong candidates for very high energy γ-ray emission. As a consequence the observing schedule for the Mark 6 telescope was changed from one which was based towards mainly galactic objects to one which allowed significant observation time of these candidate sources. This thesis contains the results from the analysis of data from four southern hemisphere blazars, considered to be possible very high energy γ-ray sources.

None of the material presented in this thesis has been submitted previously for admittance to a degree in this or any other university, except where due reference is made.

Acknowledgments

I would like to thank everyone who have helped and encouraged me with my work while at the University of Durham.

Professors D. Bloor and B. Tanner are thanked for the use of the facilities of the Department of Physics. The University of Durham is also thanked for the provision my studentship.

I would like to thank my supervisor, Dr Paula Chadwick, for her invaluable ideas, comments and support during my time at Durham. I would also like to express my thanks to all the other members of the Gamma Ray group at Durham, including Ian Roberts, Jamie Holder, Simon Shaw, Ed Dickinson, Mike Roberts, Steve Tummey, Steve Rayner, Tim Kendall, Ken Tindale, Susan Hilton, Nigel Dipper, Ted Turver, Keith Orford, Lowry McComb and Pete Edwards.

Finally, I wish to thank Sarah and Hannah for so many things for which I will be always in debt.

To the memory of Dorothy Turner

Chapter 1

Gamma Ray Astronomy

1.1 Introduction

The field of γ-ray astronomy has historically been closely linked to that of cosmic ray physics. Since the discovery of cosmic rays by Hess (1912), much effort has been directed towards determining the origins of these particles. These cosmic ray particles consist of mainly protons, nuclei and a small fraction of electrons. Determining the possible production sites of cosmic rays is severely hampered by the charged nature of these particles. As the cosmic rays pass through the interstellar medium, the galactic and intergalactic magnetic fields remove any spatial information regarding their origin. This results in an isotropic radiation field detected at the Earth.

The interactions of these energetic particles close to the production site is predicted to produce a flux of γ-rays and neutrinos detectable at the Earth. These uncharged particles will arrive at the Earth undeflected and will have therefore retained information regarding their origin. The field of neutrino astronomy is still in its infancy, but many ingenious experiments have been developed to overcome the extremely low cross-section for interaction of these particles.

This thesis is primarily concerned with γ-rays of energies between 30 GeV and 50 TeV, normally referred to as the very high energy (VHE) region. The atmospheric

Čerenkov technique (ACT) was developed as a method for detecting GeV and TeV primary particles (Galbraith and Jelley, 1953). This technique utilises the cascades of particles initiated by VHE γ-rays on entering the atmosphere. Unfortunately, the cosmic ray particles also initiate similar cascades, forming the vast background using this technique. Discrimination methods are applied to reject a significant fraction of the hadronic background, therefore enhancing any γ-ray signal. Work in the field suffered for a number of decades from the lack of an observed 'standard candle'. The difficulty in reproducing the claimed detections during this period severely hampered efforts towards improving the sensitivity of the ACT.

The detection of the Crab nebula as a steady source of TeV γ-rays revolutionized the field of VHE γ-ray astronomy (Weekes *et al.* 1989). With this detection, large improvements in the signal to noise ratio have been attainable through developments in particle cascade discrimination techniques. During the last five years many advanced telescopes utilising the ACT have been deployed. These telescopes are currently providing vital information regarding production mechanisms and physical parameters within objects such as neutron stars and active galactic nuclei (AGNs).

1.2 γ-Rays Production Mechanisms

The term 'γ-ray' is often used to define a photon which has an energy greater than the rest mass of an electron, 0.511 MeV. The production of VHE photons is dominated by particle acceleration and particle decay processes. At lower γ-ray energies, two other production mechanisms contribute to the overall flux; the transitions between nuclear energy levels (e.g. the 1.809 MeV line from radioactive ^{21}Al) and particle-antiparticle annihilation. The mechanisms relevant to the production of VHE γ-rays will be outlined in this section. For further details on these processes see Longair (1992, 1994) and Blumenthal and Gould (1970).

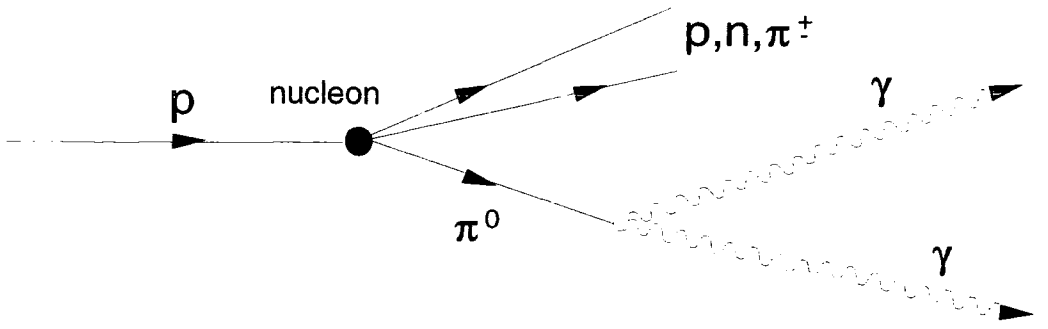

Figure 1.1: γ-ray production via π^0 decay

1.2.1 Elementary Particle Decay

The interaction of high energy nucleons will result in the production of neutral pions, see Figure 1.1

$$p + p \rightarrow p + p + \pi^0.$$

The neutral pions decay rapidly (mean lifetime of 7.6×10^{-17} s) into two photons, each of energy $\epsilon_0 = 68$ MeV within the pion's rest frame

$$\pi^0 \rightarrow 2\gamma.$$

In the observer's frame, these γ-rays are produced with energies in the range

$$\epsilon_0 \left[\frac{(1-\beta)}{(1+\beta)}\right]^{\frac{1}{2}} \quad \text{and} \quad \epsilon_0 \left[\frac{(1+\beta)}{(1-\beta)}\right]^{\frac{1}{2}}$$

where β is the initial pion velocity divided by the speed of light. This results in a spectrum of γ-ray energies centered upon ϵ_0. This process is expected to be of particular importance in possible cosmic ray production sites, as relatively large densities of energetic nucleons are expected to be present.

Pions can also be produced through photo-pion production. In this process, ultra high energy protons ($> 10^{20}$ eV) collide with photons of the 2.7 K cosmic microwave

background, producing a flux of pions and photons. The very low flux of these ultra energetic particles makes this process relatively unimportant.

1.2.2 Synchrotron Radiation

A charged particle which passes through a transverse magnetic field will move in a circular path. This acceleration causes the particle to radiate (see Figure 1.2). This process was shown to be the dominant emission mechanism within the Crab nebula (Shklovsky, 1953). In the case of very high energy particles, relativistic aberrations between the particle's and observer's frames of reference results in the synchrotron emission appearing beamed and strongly doppler shifted.

The power radiated by this mechanism is proportional to the inverse square of the particle mass. It is therefore expected that electrons will dominate the emission of synchrotron radiation. Synchrotron emission is therefore a clear signature of a population of high energy electrons (within the Crab nebula these electrons are observed to extend up to 10^{16} eV, Nolan *et al.*, 1993).

1.2.3 Bremsstrahlung Radiation

Electrons passing through the electrostatic fields surrounding ions and nuclei will become accelerated and as a result, radiation will be emitted (see Figure 1.3). The energy of this emitted radiation will be a function of the deflection angle of the electron. In the case of relativistic particles, one third of the electron's energy is on average transferred to the emitted radiation.

1.2.4 Inverse Compton Scattering

The inverse Compton scattering process is an extremely efficient mechanism of producing high energy photons. In this process an electron transfers energy to a photon

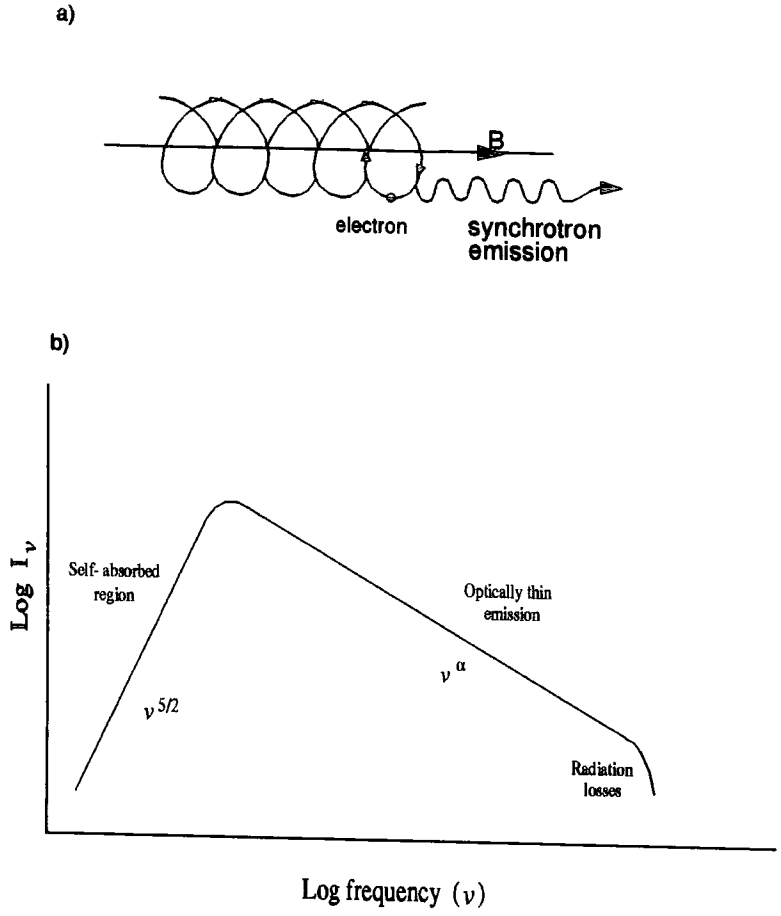

Figure 1.2: a) A schematic representation of the synchrotron emission process; b) A typical synchrotron radiation spectrum.

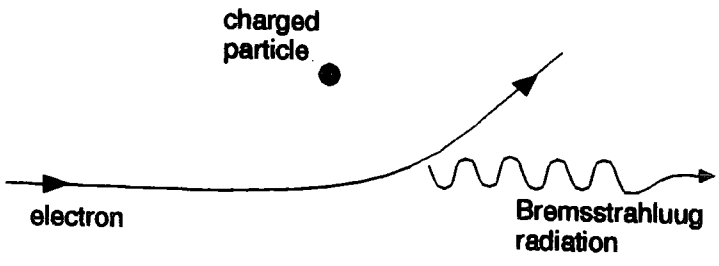

Figure 1.3: Emission of Bremsstrahlung radiation

through a collision (see Figure 1.4). The maximum energy transfer between the electron and photon occurs in a head-on collision and is given by

$$(\hbar\omega)_{max} = (\hbar\omega_0)\gamma^2(1 + \frac{v}{c})^2 \simeq 4\gamma^2\hbar\omega_0$$

leading to the important result

$$\nu \simeq \gamma^2\nu_0. \tag{1.1}$$

This enables factors of $10^6 \rightarrow 10^8$ increase in the primary photon energy to be obtained. The inverse Compton process becomes an inevitable drain of energy for high energy electrons whenever they pass through a region in which there is a large photon density.

1.2.5 Curvature Radiation

The curvature radiation mechanism was first suggested by Sturrock (1971) to explain the emission from pulsars. Charged particles moving along the curved magnetic field lines close to a pulsar will radiate emission in the forward direction (see Figure 1.5). This mechanism is analogous to the synchrotron process, except that for curvature radiation it is the strong magnetic fields forcing the electrons to follow a curved path which produces the radiation, rather than the circling around weaker fields. For γ-rays to be emitted through this process magnetic fields approaching 10^{12} gauss are required.

1.3 VHE γ-Ray Attenuation Mechanisms

The dominant attenuation process for VHE γ-rays in the atmosphere is the production of an electron-positron pair in the field surrounding a particle or a nucleus.

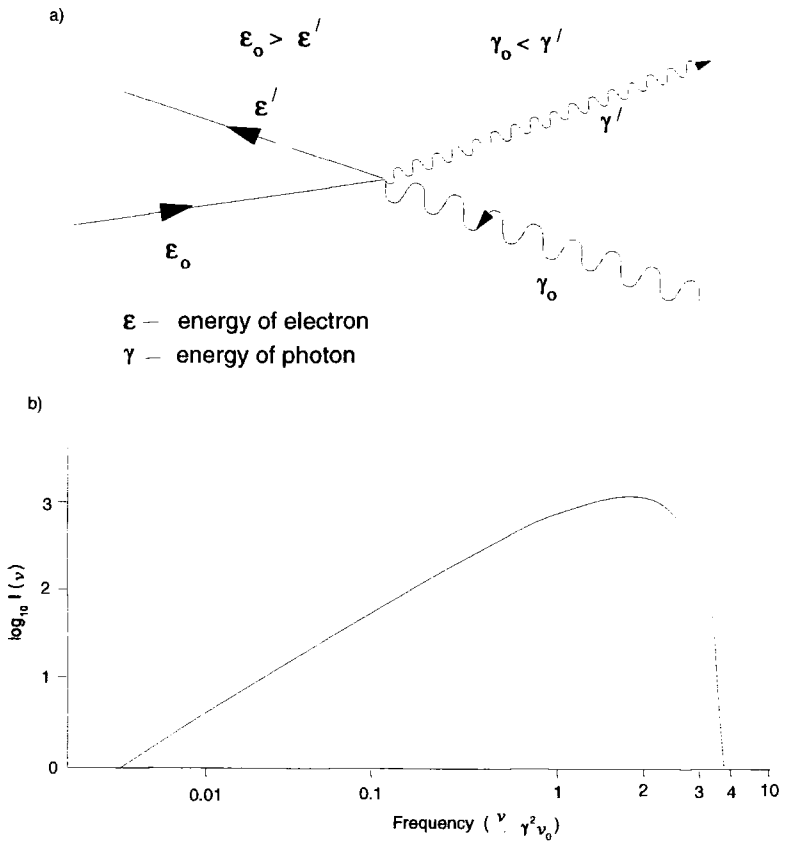

Figure 1.4: a) A schematic representation of the inverse Compton process; b) A typical spectrum produced by inverse Compton scattering (ν_0 - unscattered frequency), from Blumenthal and Gould (1970).

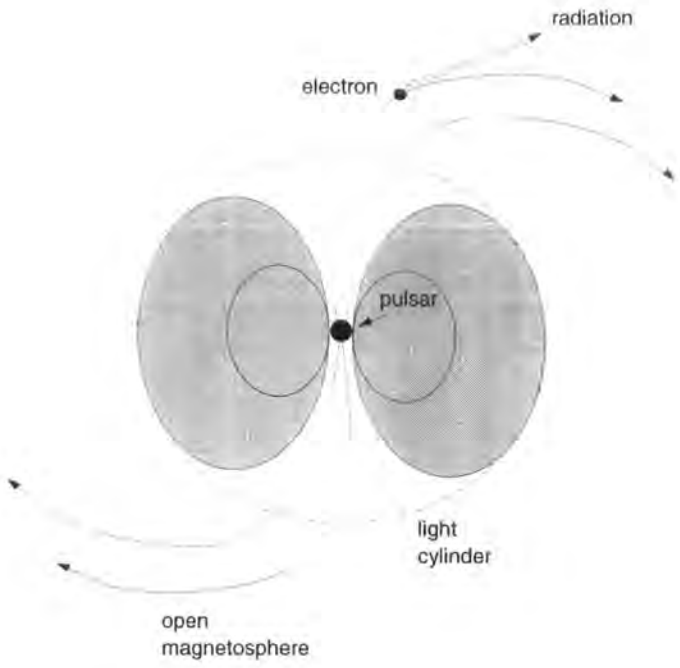

Figure 1.5: Curvature radiation produced by electrons moving along the very strong magnetic field lines surrounding a pulsar.

This process is relatively unimportant for γ-rays propagating through the interstellar medium, due to the low density of target particles.

However, the interaction of γ-rays with soft photon fields (such as optical or infrared photons) through the pair production process is not negligible

$$\gamma + \gamma \rightarrow e^+ + e^-.$$

Figure 1.6, shows the relative transparency of γ-rays to various soft photon fields. The initial calculation of γ-ray attenuation was provided by Stecker (1971). It was shown that the Universe is relatively transparent for TeV photons up to distances of 10^9 light years ($z \approx 0.1$, assuming $H_0 = 70$ km s^{-1} Mpc^{-1}). This is therefore only of importance when observing distant extragalactic objects (this subject will be returned to in Section 5.2).

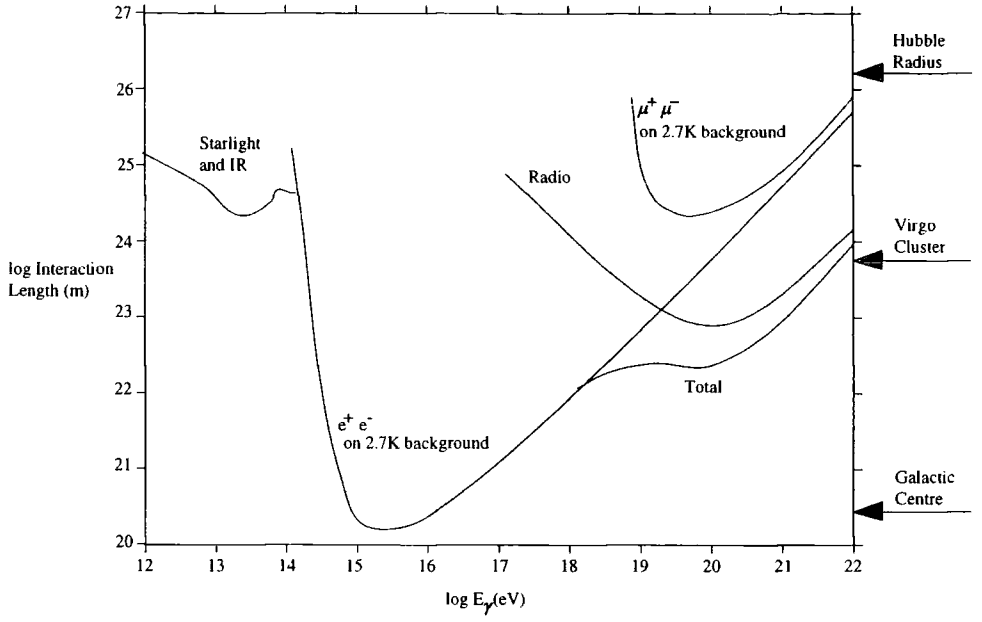

Figure 1.6: Mean free path for γ-rays against various background photon fields as a function of energy. After Ramana Murthy & Wolfendale (1986).

1.4 Gamma Ray Detection Techniques

As the γ-ray region of the electromagnetic spectrum covers over 14 orders of magnitude, a variety of detection methods have had to be developed. Typical γ-ray sources have steep spectral indices resulting in a flux of photons which decreases rapidly with energy. Detectors are therefore required with large collecting areas and relatively high duty cycles. In this section, the γ-ray spectrum has been divided into three regions, the detection techniques employed within each of these will be described.

1.4.1 Low - High Energy (0.511 MeV $\rightarrow$ 30 GeV)

At these energies γ-rays are efficiently absorbed within the atmosphere and therefore detectors have had to be placed on high altitude balloons or satellites. These have included the very successful SAS-II and COS-B satellites, the latter having detected 25 discrete γ-ray sources during its $6\frac{1}{2}$ year lifetime.

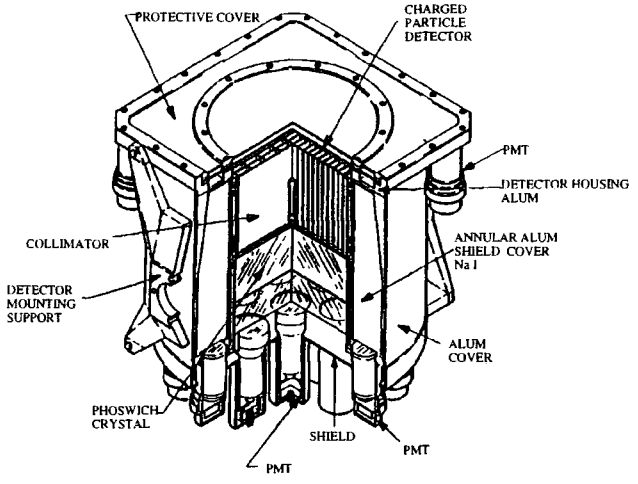

Figure 1.7: An OSSE detector (from Cameron *et al.*, 1992).

In April 1991, the Compton Gamma Ray Observatory (CGRO) was launched, one of NASA's 'great observatories'. This satellite revolutionised the field of space based γ-ray astronomy. The satellite encompasses four experiments, the combination of which allows complete coverage of the low and high energy regimes, at a sensitivity ten times that of any γ-ray experiment flown before. Each of these four experiments will be briefly described.

Oriented Scintillation Experiment (OSSE)

This detector is designed to provide observations in the 0.1 to 10 MeV range. It consists of four NaI(Tl)-CsI(Tl) scintillators, providing a 3.8° × 11.4° field of view (see Figure 1.7). It has an energy resolution of 8% at 0.661 MeV. The detectors are normally operated in co-axial pairs, with one detector pointing towards the source while a second monitors the background by pointing a few degrees away from the source position. Timing accuracy of 0.125 ms provides the resolution required for monitoring pulsars.

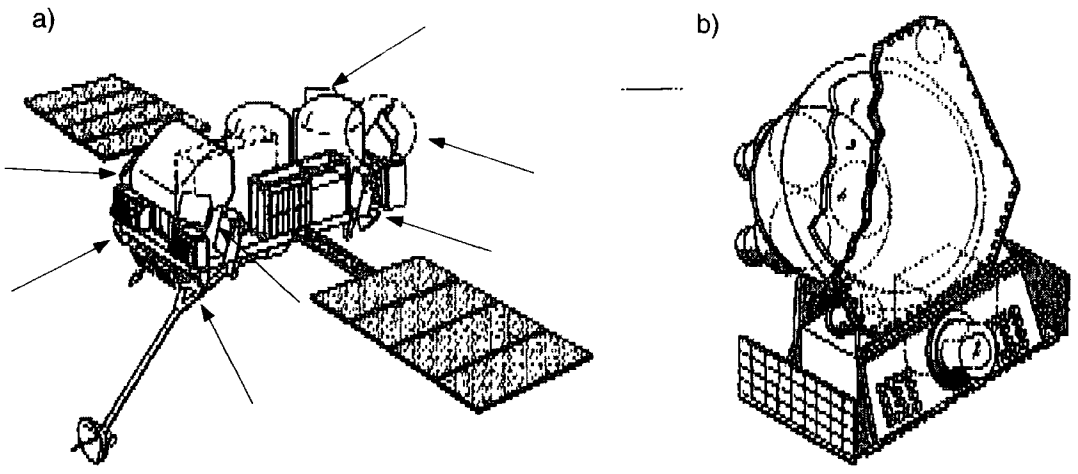

Figure 1.8: a) The CGRO satellite with the positions of seven of the eight BATSE detectors shown b) A BATSE detector

Burst and Transient Sources Experiment (BATSE)

Consisting of eight detectors, each positioned at one of the corners of the satellite, this experiment provides full sky coverage with the ability to measure brightness variations on timescales down to several ms. Each detector package consists of a 2025 cm^2 disk of uncollimated NaI(Tl) crystal providing sensitivity over the 30 $\rightarrow$ 1900 keV range and a 127 cm^2 detector which has a 15 keV $\rightarrow$ 110 MeV range. The primary purpose of this experiment has been the study of γ-ray bursts. A burst signal from BATSE will trigger the other experiments aboard CGRO to move into a burst data taking mode and through the BACODINE network observatories world wide are alerted of the position of a burst within 15 seconds.

The Imaging Compton Telescope (COMPTEL)

The COMPTEL experiment employs a two stage detection technique. An incoming γ-ray will cause a Compton scattering collision to occur in one of the upper plane modules of the detector containing a liquid scintillator. A second interaction then takes place in one of the lower planes of the detector consisting of an NaI(Tl) crystal

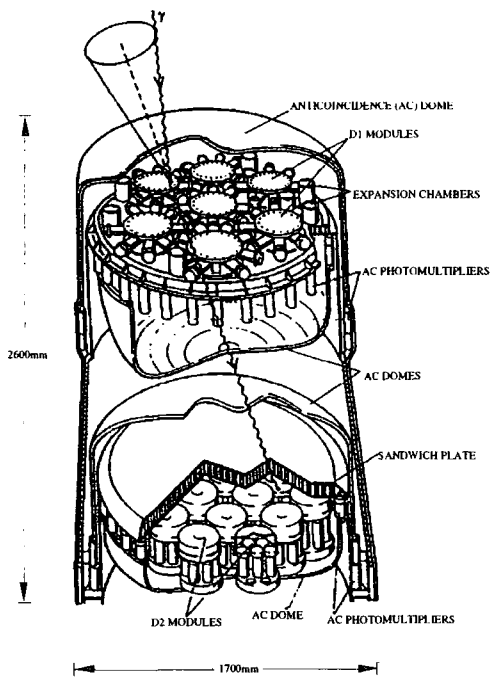

Figure 1.9: The COMPTEL detector (from den Herder *et al.*, 1992).

(see Figure 1.9). Time of flight measurements and an anticoindence shield are used to reject background events. The COMPTEL detector has a 1 steradian field of view combined with a 1 degree angular resolution. During observing phase I, COMPTEL completed a full sky survey in the energy range $1 \rightarrow 30$ MeV.

Energetic Gamma Ray Experiment (EGRET)

This experiment detects γ-rays through electron-positron pair production within a series of thin metal foils in an upper spark chamber. The path of the electron positron pair indicates the arrival direction of the photon (see Figure 1.10). A NaI(Tl) crystal at the base of the detector package acts as a calorimeter and has an energy resolution of approximately 15%. An anticoindence shield provides rejection of background events. This experiment is sensitive over the 20 MeV to 30 GeV range and has a angular resolution of less than one degree for a 1 GeV γ-ray. To date, this experiment has detected over 100 discrete γ-ray sources.

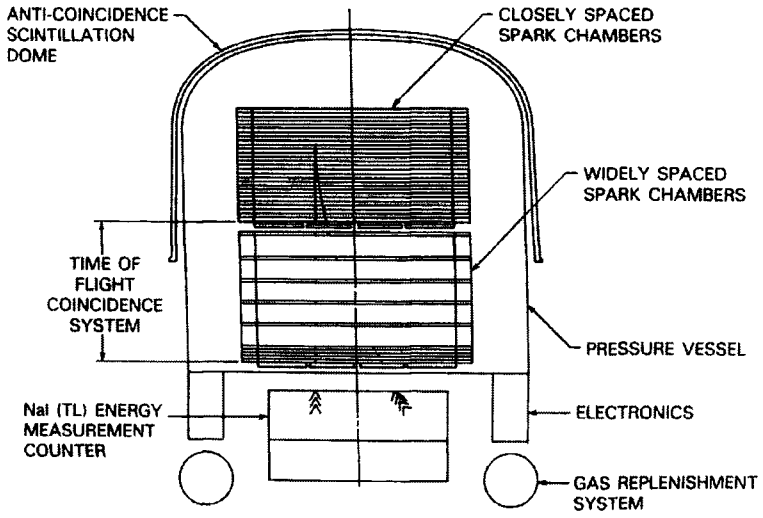

Figure 1.10: The EGRET detector (from Kanbach *et al.*, 1988)

1.4.2 VHE energy (30 GeV $\rightarrow$ 50 TeV)

Above 30 GeV the flux of γ-rays becomes too small to use satellite based detectors. For observations in the VHE range telescopes have had to be situated at ground level, detecting particles through the atmospheric Čerenkov technique. VHE photons will initiate a cascade of particles when entering the atmosphere, which results in a brief flash of Čerenkov light detectable at ground level. A number of current ground based telescopes utilising this technique have minimum threshold energies of approximately 200$\rightarrow$300 GeV. This technique will be the subject of Chapter 2.

1.4.3 Ultra High Energy ($>$ 50 TeV)

Above 50 TeV the cascade of particles initiated by a γ-ray will maximise deep within the atmosphere, resulting in a flux of particles which is detectable at mountain altitudes. These experiments normally consist of an array of scintillation detectors (numbering in the tens or hundreds), allowing large collecting areas to be obtained and a duty cycle close to 100%. The signals within the individual detectors allows the shower core location and primary energy to the determined. The density of muons within the showers provides discrimination between the hadronic initiated

background and the γ-ray cascades.

1.5 Summary

With the advent of the EGRET experiment onboard the CGRO satellite, the high energy γ-ray sky was revealed. This has a particular pertinence to the field of VHE astronomy with the two energy regimes being adjacent. The EGRET observations to date have been reviewed by Fichtel (1996) and can be summarised as the detection of:

1. Seven high energy γ-ray pulsars
2. Over 50 blazars
3. A number of high energy γ-rays associated with γ-ray bursts
4. Over 40 unidentified sources

A large number of these sources have spectra which if extending to 300 GeV would have fluxes detectable at the current sensitivities of VHE ground based telescopes. This prompted the design and construction of a new generation of atmospheric Čerenkov telescopes, utilising high resolution detectors and low threshold energies. This has included the University of Durham Mark 6 telescope (see Section 3.5).

The number of blazars detected by the EGRET experiment was unexpected, in view of the results from previous high energy γ-ray experiments (e.g. the COS-B and SAS-II satellites). This has led to observations of these objects in the VHE regime, with the resulting detection of two blazars in the northern hemisphere. The VHE observations are providing vital information regarding the physical characteristics of these astrophysical systems, possible γ-ray production mechanisms and the density of the extragalactic infrared background. This thesis will present the observations of a number of southern hemisphere blazars obtained with the University of Durham Mark 6 telescope (Chapter 6).

Chapter 2

EAS, Čerenkov Radiation and TeV Astronomy

2.1 Introduction

Observations of high energy photons (UV, X-ray and γ-rays) have required the use of balloons and satellites, due to the absorption effects of the atmosphere. The limitations on the physical size of these detectors has meant that observations above 10 GeV are severely limited, with a typical flux at this energy of only one photon per square metre per day. This has led to the need to return to ground based telescopes for the observations of very high energy γ-rays, utilising the atmospheric Čerenkov technique (ACT).

Particles above approximately 10 GeV have enough energy to initiate a cascade of particles when entering the atmosphere. The secondary particles within these cascades often have ultrarelativistic velocities, resulting in a brief emission of optical light via the Čerenkov effect. These cascades of particles develop within the atmosphere and in the case of hadrons can have a lateral extent of many hundreds of metres. This has led to these cascades of particles being termed extensive air showers (EAS). The Čerenkov light resulting from a cascade arrives at the Earth's

surface in a thin wavefront, typically only 5 ns in width, but with a large lateral spread (typically $10^5\,m^2$ at ground level); with the use of a fast detection system it is possible to resolve this brief but faint optical flash above the other sources of extraneous optical emission (e.g. starlight). The physics involved in the shower development from a photon primary is sufficiently different from that of a cosmic ray primary (which forms the vast background/noise in the measurements) that it is possible to make some form of discrimination between these two types of showers from the analysis of the resultant Čerenkov light.

The fundamental principle of the ACT is that the atmosphere becomes an intrinsic component of the detector system. The atmosphere acts as both a target for the incoming particle and as a calorimeter. The size of the flux collecting area is now determined not by the physical collecting area of the telescope system but by the size of the Čerenkov light pool produced from the EAS.

In this chapter, an outline of the physical processes within the shower development for both photons and the much more numerous cosmic ray particles will be presented (Section 2.2). Čerenkov light production will be discussed (Section 2.3), as well as its application to EAS (Section 2.3.1). The design principles behind a telescope utilising the ACT will be introduced and a review of current systems in operation will also be given (Section 2.4).

2.2 Development of Extensive Air Showers

2.2.1 Photon Initiated Showers

A photon entering the atmosphere will interact with the Coulomb field surrounding an oxygen or nitrogen atom and undergo pair production:

$$\gamma + \text{Coulomb field} \rightarrow e^+ + e^-. \tag{2.1}$$

The electrons produced will continue in the direction of the initialising photon. After some distance these electrons will undergo Bremsstrahlung, producing a secondary population of high energy photons. The shower of particles which follows is electromagnetic in nature with the dominant loss processes coming from Bremsstrahlung and pair production. The very small photonuclear cross-section means that the cascade will be very meson and nucleon poor. Above 84.2 MeV (the critical energy ε_c), the dominant loss mechanism for electrons is Bremsstrahlung rather than ionisation, and is of the form

$$-\frac{dE}{dX} = \frac{E}{X_0} \tag{2.2}$$

where X_0 is the termed the 'cascade' or 'radiation' length. This 'cascade length' is defined as the distance that an electron travels through a medium for its energy to be reduced by a factor of e^{-1}. Within air the Bremsstrahlung cascade length is 37.7 g cm^{-2}. The interaction lengths for both photons and electrons within the atmosphere are very similar with the total probability for pair production per unit 'cascade length' given by

$$\frac{1}{\lambda_{pp}} = \frac{7}{9}.$$

The electromagnetic cascade is schematically represented in Figure 2.1. The pair production and Bremsstrahlung processes continue until the energy of the electrons within the shower falls below the critical energy ε_c. Below this energy ionization becomes the dominant loss mechanism for electrons and the number of particles within the shower begins to decrease rapidly. A small number of muons are also produced via photon-pion production; the probability of a photon undergoing this process is only 2.8×10^{-4} relative to that for pair production.

Heitler (1948) provided a simple model of the electromagnetic cascade. In this model each photon travels a distance $X_0 \ln 2$ ('shower unit') and then pair produces. The electrons from this process continue for the same 'shower unit' distance and then radiate half their energy via Bremsstrahlung (these simple assumptions are sometimes termed as 'Approximation A'). Within this model the atmosphere is

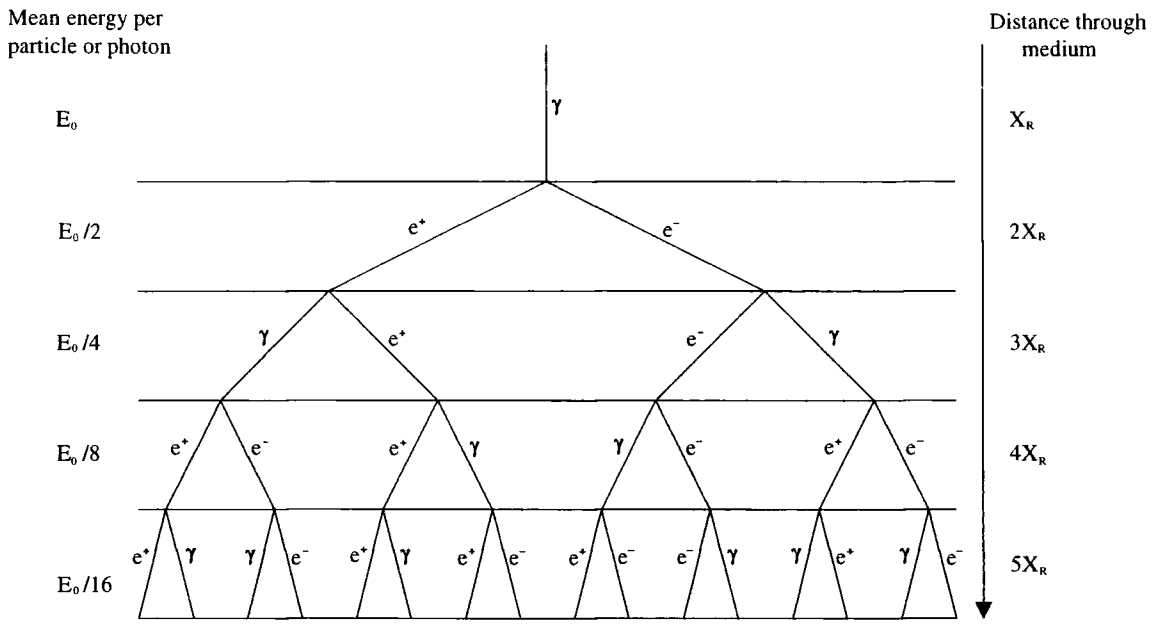

Figure 2.1: A simple model of an electromagnetic cascade. From Longair (1992).

approximately 40 shower units deep. Although it is a very simple model it does predict some important features of the cascade:

1. The number of particles within the shower will increase exponentially, until reaching shower maximum (where the energy of the electrons falls below ε_c). Below this energy the number of particles will decay exponentially through ionization effects.

2. The number of particles within the shower (N) from a primary of energy E_0 is given by

$$N = \frac{E_0}{\varepsilon_c}$$

3. The height at which the shower maximises within the atmosphere (t_{max}) in terms of shower units is given by

$$t_{max} = \ln \frac{E_0}{\varepsilon_c} \tag{2.3}$$

A more detailed analysis reveals that in the energy range 0.1 $\rightarrow$ 1.0 TeV the prediction made in (2) overestimates the number of particles within the shower by a factor of 10. A better approximation is given by

$$N \simeq E_o(\text{TeV}) \times 10^3. \tag{2.4}$$

A more rigorous model was provided by Rossi (1952), which included ionization losses of $\simeq$ 80 MeV per radiation length (termed 'Approximation B'). Greisen (1956) provided an improved description of the longitudinal development, given by

$$N(E_0, t) = \frac{0.31}{\sqrt{t_{max}}} \exp(t(1 - 1.5 \ln s)) \tag{2.5}$$

where t_{max} is defined in equation 2.3 and the shower age (s) is given by

$$s = \frac{3t}{t + 2t_{max}}. \tag{2.6}$$

The shower age parameter is equal to 0 when the primary enters the atmosphere, 1 at shower maximum and 3 when there is less than one particle in the shower. This predicts that once past shower maximum an electromagnetic cascade will attenuate rapidly with a characteristic length, $\lambda_{em} \simeq 130$ g cm^{-2}. For example, a 1 TeV photon is expected to reach shower maximum (t_{max}) after 9.4 cascade units, with $N_{max} = 1200$ particles.

The lateral spread of an electromagnetic shower is dominated by Coulomb scattering. The RMS angle through which an electron of energy E is scattered over one radiation length is given by

$$< \theta >_{RMS} \simeq (\frac{E_s}{E})^2$$

where $E_s = m_e c^2 \sqrt{\frac{4\pi}{\alpha}} = 21 MeV$. The corresponding scattering angle from pair production and Bremsstrahlung is of order $\frac{m_e c^2}{E}$. The Coulomb scattering of a 100 MeV electron would be $\approx 4.4 \times 10^{-2}$ radians, while the same electron would be deflected by only $\approx 5 \times 10^{-3}$ radians from the pair production and Bremsstrahlung processes.

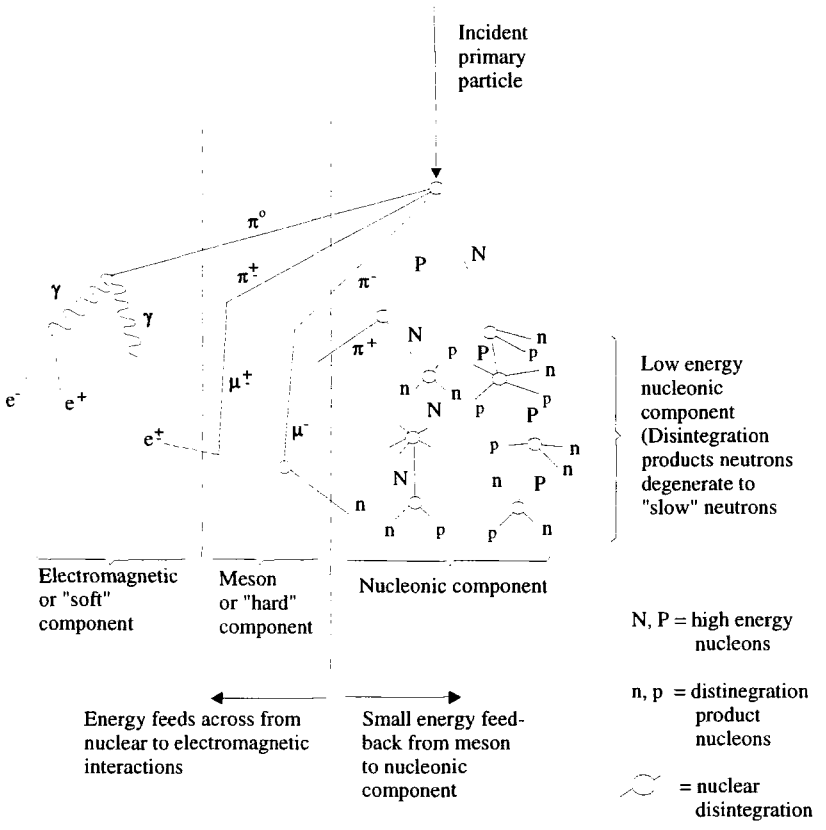

Figure 2.2: A schematic representation of a proton initiated EAS. The three components of the cascade are shown. From Simpson *et al.* (1953)

2.2.2 Hadronic Initiated Showers

A cosmic ray entering the atmosphere will interact with an air molecule to produce an EAS. The cascade produced by a hadron will have three major components, nucleonic, electromagnetic and muon (see Figure 2.2).

The interaction length λ_N, for a hadron containing N nucleons with the atmosphere is given by

$$\lambda_N = \frac{m_p}{A\sigma_{N-air}} \tag{2.7}$$

where $A = 14.5$ in air (the average atomic mass of an air molecule), m_p is the

mass of a proton and σ_{N-air} is the primary cross-section for air. The cross-section can be parameterized by

$$\sigma_{N-air} = \pi R_0^2 (14.5^{\frac{1}{3}} + N^{\frac{1}{3}} - \delta) \tag{2.8}$$

where $\delta = 1.12$ and $R_0 = 1.47$ fm (Westfall *et al.*, 1979).

The interaction length for a proton within the atmosphere is inversely proportional to its energy, and can be described by

$$\lambda_p = 67.2 (\frac{E(TeV)}{100})^{-0.065} \text{ g cm}^{-2} \text{ (Dawson, 1985).} \tag{2.9}$$

The interaction length for heavier nuclei is shorter than that for a proton; iron for example is energy independent with $\lambda_{Fe} = 13 \text{ g cm}^{-2}$. Equation 2.9 estimates that a 1 TeV proton will have a mean free path of 90 g cm^{-2}, approximately 8% of the atmospheric depth.

A collision between the primary particle and an air molecule produces pions and kaons, a process which is termed pionization. These pions and kaons provide the electromagnetic and muon components of the shower. After the initial collision the primary particle or fragments of the target nucleus continue and collide with further nucleons to produce the nuclear component of the EAS. This will continue until the energy of these secondary particles falls below that needed for multiple pion production ($\approx$ 1GeV). Below this energy the number of particles decreases rapidly, the energy being lost due to ionization. The very high Lorentz factor when converting from the centre of momentum to the observer's frame results in a collimated beam of particles along the direction of the incoming cosmic ray.

The uncharged pions produced within the shower decay rapidly (mean life time 7.6×10^{-17} s)

$$\pi^0 \rightarrow \gamma + \gamma.$$

This mode of decay forms the majority of the electromagnetic component within the

shower. The physics of the resulting electromagnetic cascade has been discussed in Section 2.2.1. However, the charged pions can decay by the following modes (mean life time 2.6×10^{-8} s)

$$\pi^+ \rightarrow \mu^+ + \nu_\mu$$

$$\pi^- \rightarrow \mu^- + \overline{\nu}_\mu$$

forming the muon component of the air shower. These muons will lose energy at a rate of 2 MeV/g cm^{-2} though ionization. They can also decay by the following modes (mean life time 2.2×10^{-6} s)

$$\mu^+ \rightarrow e^+ + \nu_e + \overline{\nu}_\mu$$

$$\mu^- \rightarrow e^- + \overline{\nu}_e + \nu_\mu.$$

The electrons produced by these decay modes will form a minor contribution to the electromagnetic component of the cascade. If the muons have Lorentz factors greater than approximately 20 (corresponding to an energy of $\simeq 10^9$ eV), then they will reach ground level without decaying and will be detectable by ground based air shower arrays. The low cross section for interaction results in the muons containing the majority of the energy of a shower at ground level.

The lateral distribution of muons within air showers is considerably broader in extent than the electromagnetic component. This is due to the height at which the muons are produced and the large transverse momenta of the pions before they decay (typically pions generated within a shower have transverse momenta of the order 400 MeV/c). Coulomb interactions which dominate the scattering of electrons are negligible for muons due to their relatively high mass. An analytical form of the lateral distribution for muons with energies greater than 1 GeV has been provided by Greisen (1960)

$$\rho_\mu(r) \propto r^{-0.75}(1 + \frac{r}{\kappa(s,\theta)})^{-2.5} \tag{2.10}$$

where κ is a function of both the zenith angle and shower age (for the definition of shower age see equation 2.6).

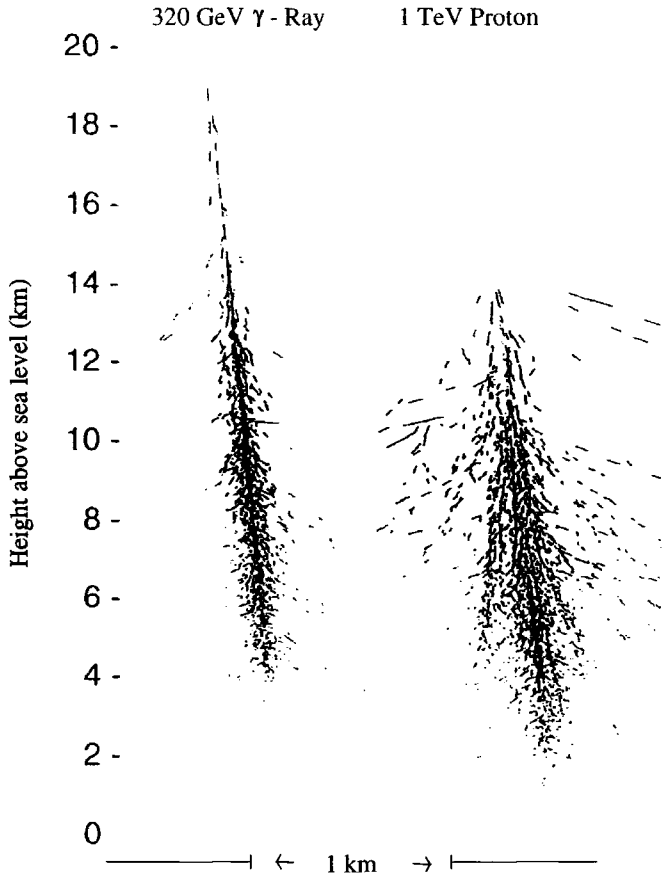

Figure 2.3: Simulations of the shower development for both a γ-ray and proton initiated EAS. The lateral scale has been expanded by a factor of five and the picture is thinned down by showing each track as a sparsely dashed line. From Hillas (1996a).

2.2.3 Differences between photon and hadron initiated EAS

Although of similar form, the hadronic and electromagnetic cascades have a number of important differences. Observations of these characteristics allows a degree of discrimination to be made concerning the cascade's initiating particle. Figure 2.3 shows simulations of the shower development for both a proton and a photon primary.

A proton will interact at a greater atmospheric depth than a photon of the same energy, due to its longer interaction length. The lateral spread of particles within a shower will also be larger for a hadronic primary than for a photon. This is due to

two processes:

1. The overall electromagnetic component of a hadronic shower is a superposition of a number of electromagnetic cascades initiated by uncharged pions produced in nuclear interactions. This produces a broad and fluctuating lateral distribution. Conversely, a photon initiated cascade will only produce a single electromagnetic cascade.
2. The nuclear components of the hadronic shower will have large transverse momenta compared to that of the electrons within a electromagnetic cascade.

A electromagnetic cascade will be relatively muon poor, with approximately 50 muons being produced from a 1 TeV primary photon. The number of muons produced within a hadronic shower is approximated by

$$N_\mu \simeq 10(\frac{E_0}{m_\pi c^2})^{0.83} \quad \text{(Gaisser, 1990).} \tag{2.11}$$

This predicts that a hadronic primary will produce a factor of 300 more muons than that produced within a photon initiated cascade of the same energy.

2.3 Čerenkov Radiation

At the beginning of this century workers in radioactivity noted a faint blue emission from transparent materials when placed near a radioactive source. This optical emission was extensively investigated by Čerenkov (1934) and as a consequence bears his name. The correct theoretical interpretation of this process was provided by Frank and Tamm (1937).

The following qualitative description of the Čerenkov effect follows that of Jelley (1958). A charged particle passing through a dielectric material will polarise the surrounding atoms. At low velocities the field produced by the passage of the charged

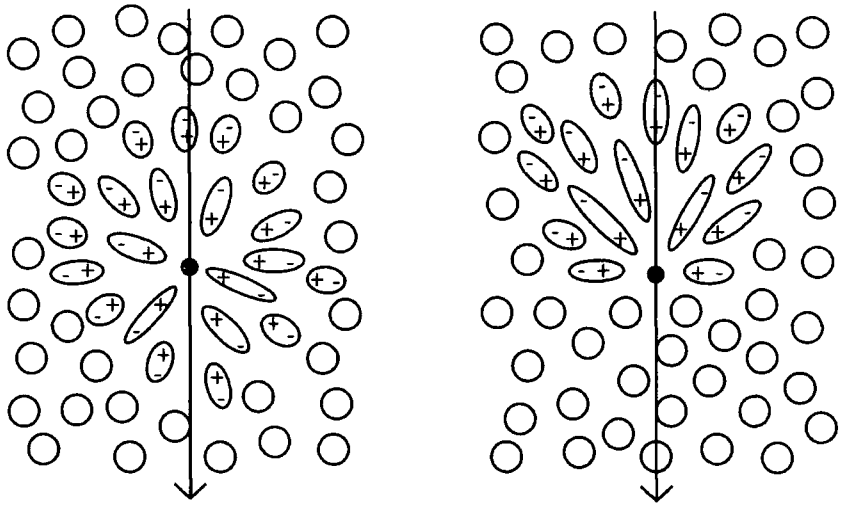

Figure 2.4: The polarization of the atoms within a dielectric medium from a slow moving charged particle (left) and a fast moving particle (right)

particle will be symmetric, but as the velocity of the particle approaches c the induced field from the polarization will no longer be symmetric but will form a dipole in the direction of particle travel (see Figure 2.4).

At velocities below the phase velocity of the dielectric medium ($v < \frac{c}{n}$) the radiation from the dipole will interfere destructively resulting in no net emission being visible. If the charged particle has a velocity greater than that of the phase velocity for that medium, it is possible for the radiation to interfere constructively, resulting in the emission of a coherent plane wave (this can be seen from the Huygens construction in Figure 2.5). From this simple illustration of the Čerenkov emission process a number of important conclusions can be drawn:

1. The angle of the coherent plane wave with respect to the direction of particle motion is given by the Čerenkov relation

$$\cos\,\theta = \frac{1}{n\beta} \tag{2.12}$$

2. No radiation will be emitted when

$$\beta < \frac{1}{n}$$

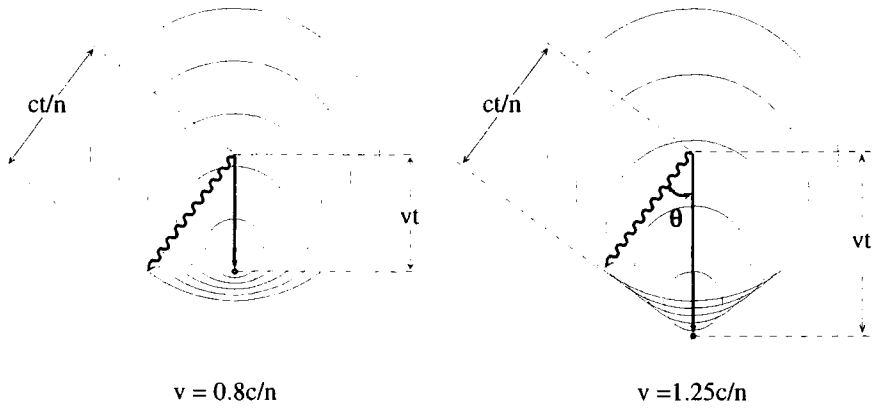

Figure 2.5: The Huygens construction for the propagation of the Čerenkov wavefront

3. In the ultrarelativistic limit ($\beta \rightarrow 1$) the Čerenkov angle tends to θ_{max} where

$$\theta_{max} = \cos^{-1} \frac{1}{n}$$

4. No Čerenkov radiation can be produced from a medium in which the real componant of the complex refractive index is less than one. This limits the minimum wavelength of Čerenkov light in air to within the UV.

Frank and Tamm (1937) showed that for an electron moving through a uniform dielectric medium the energy radiated over the path length dl is given by

$$\frac{dE}{dl} = 2\pi\alpha \int \left\{1 - (\frac{1}{n\beta})^2\right\} \omega.d\omega = \frac{\pi z^2 e^2}{\varepsilon_0} \int \left\{1 - (\frac{1}{n\beta})^2\right\} \frac{d\lambda}{\lambda} \quad \mathrm{J\,m^{-1}} \qquad (2.13)$$

integrated over the range $n\beta > 1$, where α is the fine structure constant, z is the charge on the particle, e is the electronic charge and ε_0 is the permittivity of free space. The photon production rate between λ_1 and λ_2 from a singly charged electron (neglecting dispersion) is given as

$$\frac{dN}{dl} = 2\pi\alpha \int \left\{1 - (\frac{1}{n\beta})^2\right\} \frac{d\lambda}{\lambda} = 2\pi\alpha(\frac{1}{\lambda_2} - \frac{1}{\lambda_1}) \sin^2\theta \quad \mathrm{photons\,m^{-1}}. \qquad (2.14)$$

It can be seen that the number of photons per unit path length per $d\lambda$ is an inverse square function of λ, while the energy per unit length per $d\lambda$ is an inverse cube function of λ. This results in a preference for the Čerenkov light spectrum to peak at short wavelengths (resulting in the light appearing blue).

2.3.1 Čerenkov Radiation from EAS

The possibility of Čerenkov light being produced as a result of an EAS was first suggested by Blackett (1948); and was detected four years later by Galbraith and Jelley (1953). Unlike air shower detectors which sample shower densities at a fixed point within the atmosphere, the Čerenkov emission is a product of the complete shower history (development). This provides vital information regarding the identity of the primary particle and the amount of energy dissipated within the atmosphere during shower development. Hillas (1996a) has provided a recent review of Čerenkov radiation from EAS.

A vital component in understanding the Čerenkov emission from EAS is the atmosphere. The atmosphere determines the EAS development and provides the medium to allow Čerenkov emission as well as acting as an attenuator of Čerenkov light through scattering and absorption processes. For simplicity the atmosphere can be assumed to be isothermal, with the pressure at an atmospheric height x_ν being given by

$$x_\nu = x_0 \exp \frac{-h}{h_0} \tag{2.15}$$

where x_0 is the pressure at sea level ($1033\,\mathrm{g\,cm^{-2}}$) and h_0 is termed the scale height of the atmosphere

$$h_0 = \frac{m\,g}{k\,T} \simeq 7.1\,\mathrm{km}.$$

Equation 2.15 can be written in terms of the refractive index of the medium (n), where $n = 1 + \eta$

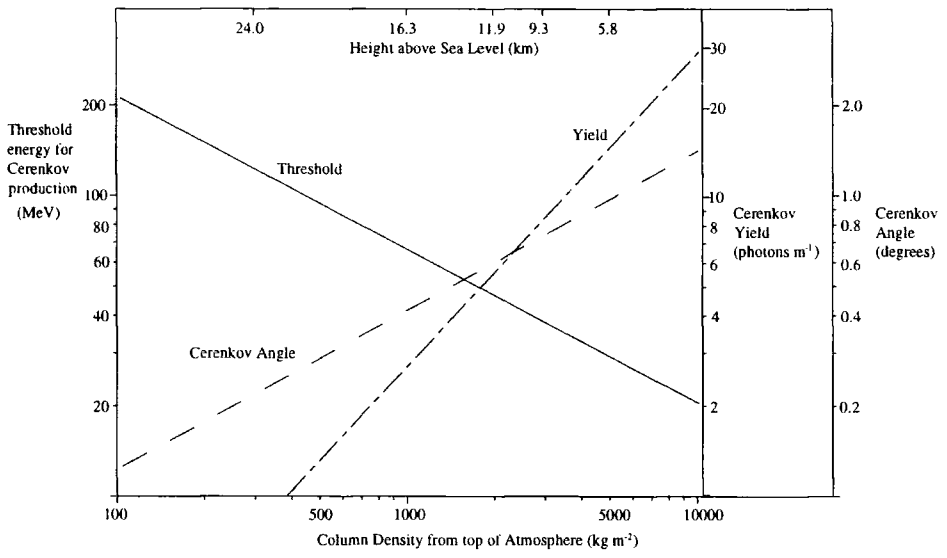

Figure 2.6: The properties of Čerenkov radiation from electrons as a function of atmospheric depth. From Ramana Murthy and Wolfendale (1986).

$$\eta = \eta_0 \exp \frac{-h}{h_0} \qquad \eta_0 = 2.9 \times 10^{-4}. \tag{2.16}$$

The minimum threshold energy for Čerenkov emission and maximum Čerenkov angle is therefore

$$E_{min} = \frac{m_0 c^2}{\sqrt{2\eta}} \qquad \theta_{max} = \sqrt{2\eta} \text{ radians.}$$

The small refractive index of the atmosphere requires particles to have relatively large energies to emit Čerenkov radiation (see Table 2.1). The majority of the Čerenkov light from an EAS as a result originates from the electrons within the shower, due to their relatively small mass. The properties of the Čerenkov emission from relativistic electrons within the atmosphere are summarised in Figure 2.6

The number of photons produced by an electron can be estimated by making an approximation to equation 2.14

$$\frac{dN}{dl} \simeq 780\,\eta \quad \text{photons cm}^{-1} \tag{2.17}$$

Table 2.1: Minimum particle energy for Čerenkov emission at sea level ($n = 1.00029$)

Particle	Minimum Energy (GeV)
Electron	0.021
Muon	4.3
Proton	39

From this approximation it can be seen that an electron at sea level will, on average, produce 22 photons per metre. As the Čerenkov photons propagate through the atmosphere a number of attenuation mechanisms are important. These include Rayleigh scattering, ozone absorption and aerosol scattering. As a result of these processes, approximately half the Čerenkov photons produced within an EAS will be 'lost'.

2.3.2 Lateral Distribution

As the light pool defines the collecting area of a ground based Čerenkov detector, the lateral distribution of the photons within this light pool is obviously of great interest. A very fast particle travelling along the shower axis will produce Čerenkov light at the characteristic angle (θ_c), which at an 8 km altitude is approximately 1.0°. As a particle approaches sea level, θ_c increases to 1.5°. This results in a rather flat light distribution out to 120m from the shower core where a region of enhanced photon density is present, termed the Čerenkov 'ring'. This 'ring' is a product of the increase in θ_c as the particle moves into the denser atmosphere closer to ground level. This results in a focusing of the Čerenkov light at around 120-150 m from the shower core (schematically shown in Figure 2.7). In practice multiple coulomb scattering of low energy electrons results in this 'ring' becoming blurred.

Monte-Carlo simulations have been used to determine the shower characteristics for both photons and cosmic ray primaries. These have revealed that photon initiated showers generally have rather flat lateral light distribution extending out to

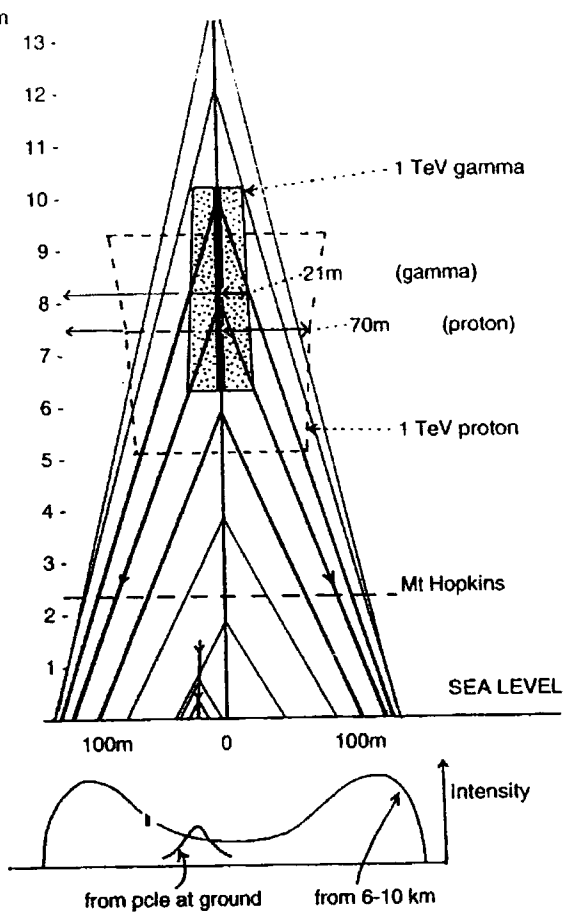

Figure 2.7: Geometry of Čerenkov rays in air showers. The stippled box contains the main region of emission of light in the γ-ray showers: 25% is emitted above the top of the box and 25% below the bottom. The median altitude is 8.1 km. At these heights, half the emission at radial distances is within the box. The dashed line box indicates the corresponding main region of emission in proton showers of the same energy. Čerenkov light is emitted from ultra-fast particles travelling along the axis at the same angle shown, resulting in a peak of intensity on the ground just beyond 100m from the centre. From Hillas (1996a).

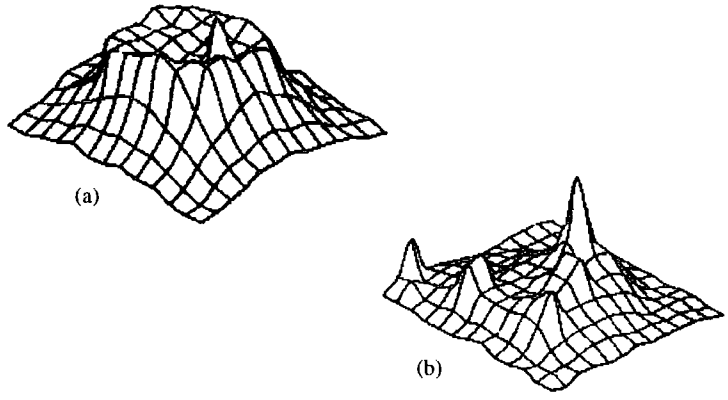

Figure 2.8: The simulated lateral light distributions from (a) a 320 GeV γ-ray and (b) a 1 TeV proton. The shower axis is at the centre of the grid. The grid spacing is 50m. From Hillas and Patterson (1987).

approximately 120-150 m from the shower core. Beyond this point the Čerenkov 'ring' is observed, followed by a $\frac{1}{r^2}$ fall off. Little shower to shower variation is seen. Cosmic ray initiated showers show a steeper fall off in the lateral light distribution than that seen for photons. Instead of a flat light pool distribution sharp peaks are seen, which are due to Čerenkov light emitted from locally penetrating particles (mainly muons). Simulated lateral light distributions for both a photon and a proton are shown in Figure 2.8.

2.3.3 Images of Čerenkov Radiation from EAS

As discussed in Sections 2.3.1 and 2.3.2 there are intrinsic differences between both the shower development and resultant Čerenkov radiation from γ-ray and cosmic ray initiated cascades. These differences can be used as a discriminator between primary initiating particles and hence improve the signal to noise ratio when looking for VHE γ-ray sources. In practice this is achieved by recording the image of the Čerenkov flash from an EAS (normally with a simple 'camera' consisting of an array of photomultipliers). It is useful to review the characteristics we expect for the Čerenkov emission from both γ-ray and hadron primaries:

- γ-**rays**: As seen in Section 2.2.1 a photon primary will initiate an electromagnetic cascade high in the atmosphere. This cascade will travel forward along the arrival direction of the initial photon and will be highly constrained in its lateral extent. Except for the very highest energy photons, the cascade will die out a number of km above ground level (4 km for a 400 GeV primary photon). The Čerenkov emission from the electrons in the shower will form an elliptical 'image' when viewed from the ground. Due to perspective effects the major axis of this ellipse will be aligned along the arrival direction of the initial photon, normally a point source in the sky. This results in a relatively small elliptical image which should be aligned in the direction of the γ-ray source.

- **Cosmic Ray**: Section 2.2.2 showed that a proton will initiate a hadronic cascade at a greater atmospheric depth than for a photon of the same energy. The pions produced within the shower have large transverse momenta, which results in the lateral development of the shower becoming large. Local penetrating particles at ground level, such a muons, will produce local peaks of enhanced Čerenkov emission within the light pool. The Čerenkov 'image' from a cosmic ray will generally be broad and irregular in shape with no preferred orientation.

2.4 TeV Telescopes

The first observations of Čerenkov light emitted from an EAS were made by Galbraith and Jelley (1953). Their early attempts involved a photomultiplier tube at the prime focus of a 25cm diameter parabolic mirror. This system was triggered in coincidence with a local air shower array.

The first prediction that TeV γ-rays should be observable from a discrete astrophysical object was made by Cocconi (1959). It was suggested that the Crab nebula should be a strong TeV γ-ray source (the predicted flux was a factor 1000 larger

than that actually measured three decades later). Stimulated by this suggestion, the first serious attempts at TeV astronomy were undertaken by the Crimea group from the Lebedev Institute in Moscow (Chudakov *et al.*, 1965). The experiment consisted of 12 telescopes each with a 1.7 m^2 collecting area. This system relied on the detection of directional anisotropies above the hadronic background as an indicator of a discrete source of TeV γ-rays. This experiment produced an upper limit from the Crab nebula two orders of magnitude below that predicted by Cocconi. Although unsuccessful, this work prompted a number of groups to join this field, primarily in the USA, Ireland and India.

Interest in the Crab nebula was further encouraged with the suggestion by Gould (1965) that the spectrum from the radio through to X-rays was due to synchrotron emission. It was further suggested that inverse Compton scattering of these synchrotron photons would produce a detectable flux of TeV photons. Fazio *et al.* (1972), with the new Whipple 10m telescope at Mt.Hopkins detected the Crab nebula with a 3σ significance, which at the time was treated as an upper limit. The subsequent lack of any firm evidence for TeV emission frustrated the field for many years.

It was clear that large improvements in telescope sensitivities were required for the field to progress. With the advent of faster computers, simulations of EAS were possible. These revealed the fundamental differences between hadronic and γ-ray initiated showers, as seen in Section 2.2.3. Weekes and Turver (1977) suggested that at low energies γ-rays ($\leq$ 100 GeV) become far more efficient at producing Čerenkov light than hadrons. It was suggested that an array of detector elements would allow the angular spread and direction of the Čerenkov light from an EAS to be determined. This idea was developed by Hillas (1985) to give the atmospheric imaging technique. Detector packages consisting of an array of 37 photomultiplier tubes were developed for the Crimean Astrophysical Observatory and the Whipple telescope. Telescopes utilising these crude imaging cameras are sometimes referred to as second generation telescopes. The Durham and South African groups also pioneered the observations of periodic objects (pulsars, X-ray binaries and cataclysmic

variables), using the periodicity as a powerful tool in searching for γ-ray signals.

The Whipple collaboration published the first evidence for the Crab nebula as a steady source of TeV γ-rays (Weekes *et al.*, 1989). Using the newly developed imaging technique this source was detected with a 9σ significance. This detection produced the much sought after 'standard candle' at TeV energies and allowed further refinements to the background rejection techniques to be made.

2.4.1 Design Principles

This section follows the arguments presented by Cawley and Weekes (1995). The basic requirement for the design of a telescope which utilises the ACT is the ability to record the brief flash of Čerenkov light produced by an EAS while keeping the number of background sky photons to a minimum. It is obvious that a telescope design should be based around the characteristics of the Čerenkov flash, using both its brief duration and emission spectrum.

Background light can originate from a number of sources, including star light, diffuse galactic emission and atmospheric scattering. A typical value of the total background is given as 10^{12} photons $m^{-2}s^{-1}$ sr^{-1}, in the 330-450 nm band. This value can vary considerably between sites and with atmospheric conditions. The typical Čerenkov flash from a 1 TeV photon will produce a flux of approximately 50 photons m^{-2} within a duration of 5 ns at a distance of up to 150 m from the shower core.

The telescope system should have an 'acceptance time' which allows the full Čerenkov flash to be recorded. The aperture should be matched to the angular spread of this flash, typically $1 \rightarrow 2^{o}$. This system should therefore allow the recording of the Čerenkov flash while keeping the background level to only a few photons. As seen in Section 2.3, the spectrum of the Čerenkov light is peaked toward the blue and near UV, therefore a detector system which has a high quantum efficiency in this region is an obvious advantage. In practice an array of photomul-

tiplier tubes are used as the detector system, due mainly to their fast response time and relatively low cost.

By attempting to optimise the signal to noise ratio the basic principles of a telescope utilising the ACT can be seen. For a simple system consisting of a mirror and a PMT the night sky noise fluctuations are given by

$$N = \sqrt{\int_{\lambda_1}^{\lambda_2} B(\lambda)\,\varepsilon(\lambda)\,\Omega\,t\,d\,d\lambda} \tag{2.18}$$

where $B(\lambda)$ is the background light flux as a function of λ, $\varepsilon(\lambda)$ - quantum efficiency, Ω - solid acceptance angle, t - integration time, d - mirror area and $\lambda_1 - \lambda_2$ is the wavelengths over which the detector system is sensitive. The Čerenkov signal from an air shower is given by

$$S = \int_{\lambda_1}^{\lambda_2} C(\lambda)\,\varepsilon(\lambda)\,\Omega\,d\,d\lambda \tag{2.19}$$

where $C(\lambda)$ is the Čerenkov photon flux in photons $\mathrm{m}^{-2}\mathrm{sr}^{-1}$. The signal to noise ratio at wavelength, λ, is therefore given by

$$\frac{S}{N} = C\sqrt{\frac{\varepsilon\,\Omega\,d}{B\,t}}. \tag{2.20}$$

It is useful to determine the minimum flux sensitivity at the effective energy threshold. The background comes from the isotropic cosmic ray flux and noise fluctuations

$$N = \sqrt{k_b\,E_b^{-1.7}\,A_b(E_b)\,\Omega\,T}$$

and the signal is given by

$$S = k_g\,E_g^{-G}\,A_g(E_g)\,T$$

where E_g is the γ-ray energy threshold, E_b - cosmic ray energy threshold, G - the integral power law exponent of the γ-ray source, $A_g(E_g)$ - the collecting area for γ-rays, $A_b(E_b)$ - collecting area for cosmic rays, Ω - detector solid angle, T - observation

time, k_b and k_g are constants which characterise the flux levels of the source and background. The signal to noise can be expressed as a function of the number of standard deviations, N_{sig} (σ). Assuming that A_g and A_b are independent of energy above the threshold energy then

$$N_{sig} \propto \frac{A_g T^{\frac{1}{2}} E^{0.85-G}}{\sqrt{A_b \Omega}}. \tag{2.21}$$

Therefore to increase N_{sig} and as a consequence the sensitivity of a telescope system a number of parameters can be optimised:

1. Increase the collecting area for γ-rays
2. Increase the observing time
3. Operate at an optimum energy threshold (normally this energy is as low as possible, except for the very hardest γ-ray spectra)
4. Minimise the effective collecting area for cosmic rays ($A_b(\Omega)$), using discrimination techniques.

The γ-ray collecting area can be increased by optimising the solid acceptance angle of the telescope. The flat lateral light distribution from a γ-ray, which is typically 250 metres in diameter, will determine this optimum acceptance angle. A shower whose light pool just reaches the telescope will subtend the largest angle within a detector. An acceptance angle larger than this value will just record extra background light. A smaller acceptance angle would mean that the telescope is not fully utilising the whole Čerenkov light pool. The optimum value of Ω is typically $3 \rightarrow 4^o$. For the vast majority of objects the optimum energy threshold for a telescope to operate at is simply the lowest possible (the only exception is for a source which has a source spectral index, $G < 0.85$). Reducing the effective collecting area for background showers has been by far the most successful method of increasing the sensitivity of the ACT. This has been achieved mainly through the development of powerful discrimination techniques, such as imaging. These techniques will be described in Section 4.2.

A characteristic of the Durham Čerenkov telescopes is the 3-fold coincidence triggering system employed (the telescopes are fully described in Chapter 3). This is achieved with the use of three co-axial flux collectors positioned on a single mount. The triggering requirement is that a signal must be detected from each of these flux collectors within a short gate time (normally 10 ns). This allows the photomultiplier tubes to be operated at significantly higher noise rates (resulting in higher gain) compared to a single triggering dish, with no increase in the accidental trigger rate. This 3-fold system also benefits from the absence of triggers due to muons passing through the detector packages. There is also a vastly reduced probability of triggering on local muon Čerenkov rings, than for a single triggering dish (these muon triggers start to become the dominant noise factor at low threshold energies for a single flux collector).

2.4.2 Current VHE γ-Ray Experiments

The high resolution Čerenkov telescopes that are currently operational are listed in Table 2.2. The Durham Mark 6 and CANGAROO telescopes are located in the southern hemisphere. Low resolution and timing telescopes are not included in this table; for a current list of all the Čerenkov telescopes currently operational see Weekes (1996).

2.4.3 Current TeV γ-Ray Source Catalogue

The TeV sources detected using the imaging technique are shown in Table 2.3. Historically, a large number of other sources have been reported as TeV detections, including pulsars, cataclysmic variables and X-ray binaries. These sources were characterised by their transient nature. With the recent improvements in telescope sensitivities it should be possible to make observations of these objects which will confirm or refute their existence as VHE γ-ray sources.

Table 2.2: Current operational high resolution imaging VHE Čerenkov telescopes

Name	No. of Telescopes	Site alt (m)	Threshold (TeV)	Collecting area (m^2)	No. of Pixels	Resolution (degrees)
CAT [1]	1	1650	0.2	17.5	588	0.12
CANGAROO [2]	1	160	1.0	12	220	0.12
Durham Mk 6 [3]	1	250	0.25	120 (3 dishes)	109	0.24
HEGRA [4]	5	2200	0.5	8.5	271	0.24
Whipple [5]	1	2320	0.25	70	151	0.25
Telescope Array [6]	7	1600	0.6	6	256	0.25

(1) - Barrau *et al.* (1997); (2) - Kifune *et al.* (1993); (3) - Chadwick *et al.* (1995); (4) - Daum *et al.* (1997); (5) - McEnery *et al.* (1997); (6) - Aiso *et al.* (1997).

Table 2.3: TeV γ-ray sources detected using the high resolution imaging technique

Source name	Object type	Variable emission	Periodic emission	Detection
Crab Nebula	SNR	NO	NO	Whipple, Sandia, Crimea, ASGAT HEGRA, Themis, CAT, CANGAROO, Telescope Array
PSR1706	SNR	NO	NO	CANGAROO, Durham
Mrk 421	AGN	YES	NO	Whipple, HEGRA, CAT, Telescope Array
Mrk 501	AGN	YES	NO	Whipple, HEGRA, CAT, Telescope Array

2.5 Summary

In this chapter the principles of extensive air showers, the Čerenkov effect and their application to TeV astronomy have been introduced. The low flux levels of VHE γ-rays has necessitated the need for a design of telescope with an inherently large collecting area. This has been possible with ground based telescopes utilising the atmospheric Čerenkov technique.

Photons of a high enough energy will initiate a cascade of particles within the atmosphere. These particles will emit brief flashes of Čerenkov light. This light is emitted within a narrow cone in the direction of travel of the primary particle. The resultant light pool from this emission is typically spread over 5×10^4 m^2 at sea level. A flux collector detecting this Čerenkov emission will therefore have an effective collecting area equivalent to the size of this light pool, thus allowing very low flux levels to be sampled. Severely hampering the detection of photon initiated cascades are the abundant cosmic ray particles (cosmic rays typically outnumber γ-rays by 1000 to 1). These protons and charged nuclei (as well a small fraction of electrons) also initiate cascades of particles resulting in Čerenkov emission.

The cascade of particles formed from a photon will be almost entirely electromagnetic in nature. Conversely, cosmic ray initiated cascades will also have an electromagnetic component but will be dominated by hadronic and muon components. The physical interactions during the shower development result in the cosmic ray initiated cascades having a large lateral extent within the atmosphere compared to the purely electromagnetic cascades formed by γ-rays. This large lateral distribution and general nonuniformity is reflected in the Čerenkov emission detectable at ground level. Photon initiated cascades are seen to be narrowly confined during development with the resultant Čerenkov emission observed to be uniform in its lateral extent at ground level.

These differences in cascade development and Čerenkov emission characteristics have allowed discrimination techniques to be developed. By forming an image of the Čerenkov flash with the use of a mirror and crude camera it is possible to determine

simple shower features. These cameras are generally constructed from photomultiplier tubes, whose response time is matched to the duration of the Čerenkov flash ($\sim$10 ns). By only accepting this brief Čerenkov flash it is possible to reduce the ambient background light collected during this period to only a few photons per m^2. Selecting Čerenkov images with characteristics that are close to those expected for a γ-ray initiated cascade allows vast improvements in the signal to noise to be made.

During the last five years a new generation of telescopes utilising this imagining discrimination technique have become operational. These telescopes are characterised by high resolution cameras, with typically between 91 and nearly 600 photomultiplier tubes. In an effort to reduce the energy thresholds of these systems and improve the background hadronic rejection a number of different techniques have been employed. For example, the HEGRA collaboration have installed an array of five identical high resolution telescopes. This allows the Čerenkov light from an air shower to be sampled at a number of different points within the light pool. With a number of different measurements of an individual shower's characteristics it has been possible to almost eliminate the background cosmic ray events. The CAT collaboration has employed a very high resolution camera combined with a very fast system of electronics. The speed of the electronics has reduced the amount background light detected, allowing extremely faint Čerenkov images (from low energy initiating primaries) to be resolved.

The techniques employed in the design and construction of the University of Durham Mark 6 telescope in order to achieve a low threshold energy and improved discrimination power will be described in Chapter 3.

Chapter 3

The University of Durham Atmospheric Čerenkov Telescopes

In this chapter the three atmospheric Čerenkov telescopes operated by the University of Durham will be introduced. A brief review of the Mark 3 and Mark 5 telescopes will be presented as well as a detailed summary of the Mark 6 telescope. The determination of the threshold energy for the Mark 6 telescope will also be discussed.

3.1 The Bohena Site

The University of Durham atmospheric Čerenkov telescopes are located at the Bohena settlement, near Narrabri, New South Wales, Australia (30° 28′ 20.6″ S, 149° 39′ 36.5″ E, alt 260 m). A southern hemisphere site was chosen due to the large number of relevant astronomical objects observable, including the majority of the galactic plane (and as a result a large number of important galactic objects such as pulsars, X-ray binaries and supernova remnants) and the Large and Small Magellanic Clouds. A site in Australia generally provides good weather conditions for the majority of the year and low levels of man made background light pollution (in the case of the Bohena site the nearest town is over 20 km away).

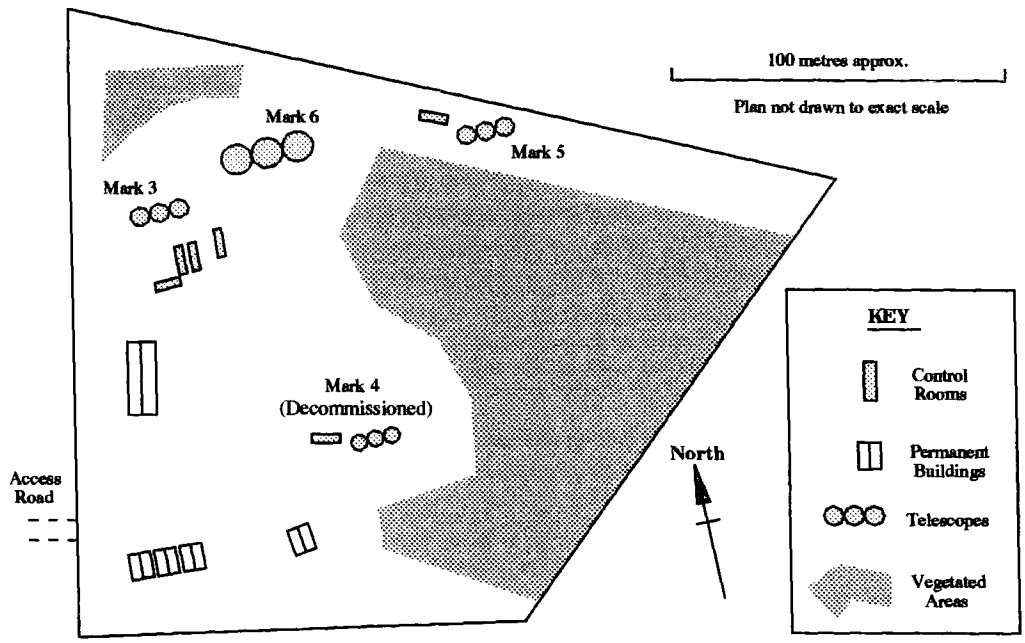

Figure 3.1: A plan of the Bohena site.

The Bohena site was previously occupied by the University of Sydney cosmic ray air shower detector, SUGAR. As a result this site provided the facilities and logistical infrastructure required to operate a number of atmospheric Čerenkov telescopes. A plan of the site is shown in Figure 3.1. The Mark 3 and Mark 5 are separated by 100 m along an east-west line. The Mark 6 is positioned 20 m to the east of the Mark 3. Each telescope has a control room (a converted shipping container) in which the electronics, steering control and the data logging equipment are situated. These telescope control rooms are connected to a central control room, in which the telescopes' performances (environmental conditions, steering, photomultiplier information and trigger rates) can be monitored during an observation, via ethernet and Econet networks. The central control room also serves as a daytime logistics centre.

3.1.1 Timekeeping

A large part of the University of Durham's telescope time has been directed in searching for pulsed TeV γ-ray emission from pulsars. An accurate knowledge of

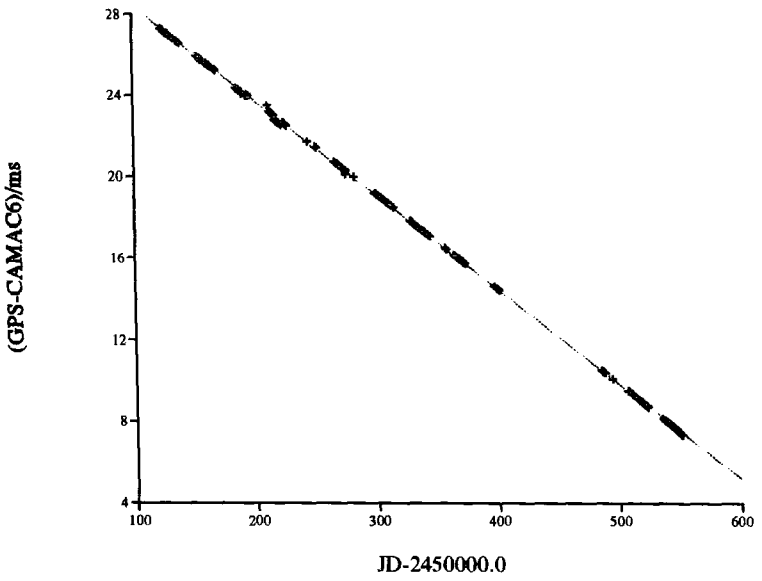

Figure 3.2: The Rubidium atomic oscillator clock drift as measured with respect to the GPS timing signal between February 1996 and April 1997.

the absolute time is an obvious precursor to enable this work. This is achieved with an Efratom FRK-L rubidium atomic oscillator situated within the Mark 3 control container. This oscillator provides a 10 MHz output which is used to record the time of each event to μs accuracy. In April 1992, a PC based GPS timing system was installed, providing a simple method for determining the rubidium clock drift rate. Prior to this date, the drift rate was determined with respect to a radio timing signal. This measurement is made on a daily basis and the recent drift rate can be seen in Figure 3.2.

3.2 Mirror Construction and Properties

The design of the flux collectors for an atmospheric Čerenkov telescope should be optimised to account for the brief temporal spread of Čerenkov photons, the large lateral light pool and the inherent angular extent of features within the EAS. The extended nature of an EAS determines the imaging characteristic required, typically a point spread function of between $0.1° \rightarrow 0.25°$, depending upon the pitch angle of the individual photomultiplier tubes in use, is often quoted as adequate.

Increasing the flux collecting area will allow the threshold energy of a telescope system to be reduced, as low Čerenkov photon densities within the light pool can be sampled. Such large flux collectors are required to be relatively light in order not to make the telescope superstructure overly large. A further constraint on the production of large flux collectors is the requirement to keep costs, both in materials and man hours for construction, to a minimum.

To satisfy these design criteria the University of Durham γ-ray group have advanced a design of mirror construction first applied to the antenna sections of the James Clerk Maxwell millimetre wavelength telescope. A thin anodised aluminium sheet is stretched over a steel former of the required shape (this is usually a segment of a parabolic mirror). These aluminium sheets are then fixed to a bonded honeycomb structure and an aluminium backing plate with epoxy resin. This provides a stiff and yet light mirror segment. A reflectivity of 80% between 300 and 500 nm has been measured, with little degradation noted over a period of a decade (Weekes, 1985). The use of a simple former allows the mass production of mirror segments. Mirrors constructed by this method can achieve the desired point spread function.

An inherent design feature of these mirrors is their very low thermal inertia. The mirror surface temperature can therefore fall below that of the ambient air temperature through coupling with the night sky. During the winter months this leads to water droplets forming (misting) on the mirror surface. If the ambient air temperature falls to within a few degrees of 0° C, ice can also form on these mirror surfaces. To stop the formation of water droplets, a surfactant solution is sprayed onto the mirror surfaces prior to an observation (the effect of this solution will last for approximately 12 hours). The group is currently testing methods to reduce the formation of ice on the mirror surfaces. One possibility being studied is the implementation of fans fitted on to the telescope structure which are designed to produce a flow of air across the mirror surfaces (see Roberts, 1997a).

3.3 The Mark 3 Telescope

The Mark 3 telescope was constructed at the Bohena site in November 1986. For a full description of the telescope see Chadwick (1987). Various upgrades have been implemented since its construction, the majority of these are described in Bowden (1993). A brief review of the current telescope setup is presented here.

In common with all the University of Durham Čerenkov telescopes, a three fold coincidence system is utilised. This is achieved by mounting three co-axial flux collectors on a single alt-azimuth mount. These flux collectors are commonly termed as the left, centre and right dishes. The three fold coincidence system allows the photomultiplier tubes (PMTs) within the detector packages to operate at a high gain while maintaining a low accidental trigger rate. This system also has the advantages of recording three samples of each shower and a greatly reduced trigger rate from local muons compared to a single triggering dish (see Section 2.4.1).

The left and right flux collectors are constructed from 43 tessellated mirrors, each 60 cm in diameter. These dishes are 4 m in diameter with a focal length of 2.45 m and a 11 m^2 mirror area. The central mirror is constructed from 12 parabolic mirror segments, with a diameter of 3.5 m and a 3.32 m focal length. The point spread function for this central dish is approximately 2.5 cm full width half maximum (FWHM) at the detector package.

The left and right detector packages (commonly termed 'cameras') consist of 7 hexagonal Phillips XP3422 PMTs. The centre detector package is constructed from 19 hexagonally close packed one inch Burle S83062E tubes, surrounded by a circular ring of 12 1.5 inch Burle C7151Q tubes. The field of view of this central camera is 2.5°, with each one inch tube having a pitch of 0.5°. The telescope triggering criteria requires a signal in the corresponding left and right PMTs as well as a signal from any one of the 19 one inch PMTs in the centre camera above a fixed threshold and within a gatetime of 10 ns.

3.4 The Mark 5 Telescope

The Mark 5 telescope was designed primarily as a prototype of a low threshold energy Čerenkov telescope, for full details see Dickinson (1995). The design characteristics and telescope infrastructure developed with the Mark 5 were later utilised in the construction of the Mark 6. The three flux collectors are constructed from 12×30° parabolic mirror segments, with a diameter of 3.5 m and a focal length of 3.32 m. The detector packages and triggering system are as in the Mark 3 telescope.

When the Mark 3 and Mark 5 telescopes are observing the same object, these two systems act as a stereo pair. At the zenith, approximately 45% of the events which trigger the Mark 5 telescope will also trigger the Mark 3. Correlations between lower moments of the images recorded (see Section 4.2) have been exploited to provide discrimination between γ-rays and hadrons, see Chadwick *et al.* (1996).

3.5 The Mark 6 Telescope

The Mark 6 telescope has been designed to be a low threshold energy γ-ray telescope combined with a high resolution imaging capability. Based on a tested design it has twice the linear dimensions of the Mark 5 telescope. Construction took place during June and July 1994 at the Bohena site (for full details see Dickinson, 1995). The Mark 6 and Mark 5 can act as a stereo pair of telescopes, this area of data analysis is currently being investigated within the group, see Roberts (1997a).

Each of the three flux collectors are constructed from 24 15° paraboloid mirror segments. Each collector has a 7.0 m diameter, a 7.2 m focal length and a collecting area of 42 m^2. The mirrors were aligned with a laser calibration system described in Dickinson (1995) and after construction was completed the point spread function of the central mirror was determined to be 0.34° FWHM (see Figure 4.6). This point spread function has been measured on a number of subsequent occasions and has not been observed to deviate from this value.

Figure 3.3: The Mark 6 telescope

During July and November 1995, the Mark 6 superstructure was covered with opaque shielding in order to reduce the amount of extraneous ambient light detected by the PMTs.

3.5.1 Detector Packages

The central detector package consists of 91 hexagonally close-packed one inch Hamamatsu R1924 PMTs, surrounded by a 'guard ring' of 18 circular two inch Burle 8575 PMTs (see Figure 3.5). The 3 cm tube pitch of the circular one inch PMTs corresponds to a field of view of 0.3° and an aperture for the high resolution component of 2.64° across opposite vertices. The two inch PMTs forming the 'guard ring' allow the light density outside the high resolution region to be determined. The left and right cameras consist of 19 close-packed hexagonal Phillips XP3422 PMTs, each with a 0.5° field of view. The aperture of these hexagonal PMTs is matched to the high resolution component of the central camera.

Conical light cones have been fitted to the faces of both the one inch central

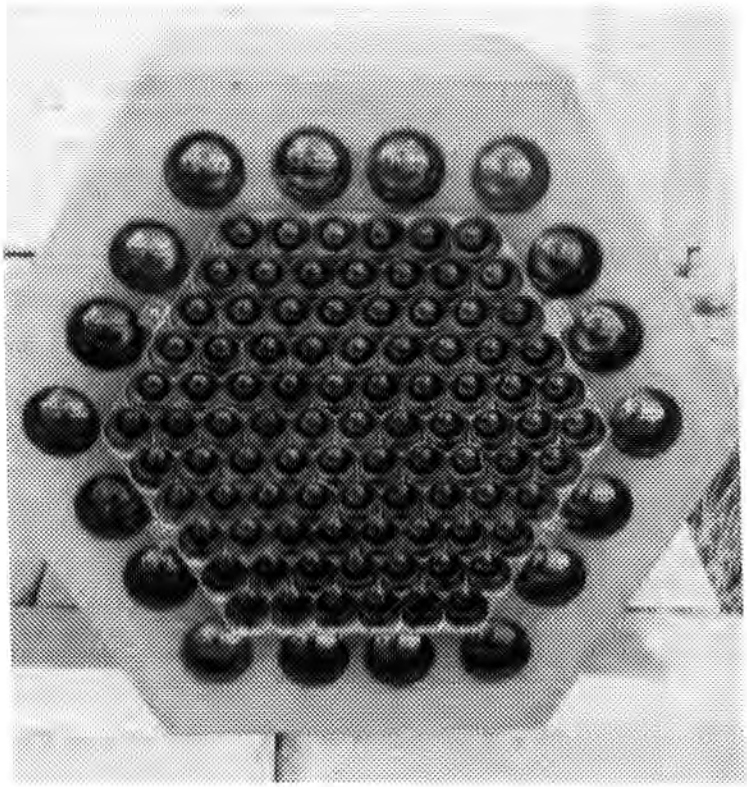

Figure 3.4: The Mark 6 central detector package

camera PMTs and the hexagonal PMTs in the left and right cameras. In the case of the one inch PMTs, the cones allow light collection from areas between the circular photocathodes of the tubes. The large photocathode area of the hexagonal tubes in the left and right detector packages results in a characteristically broad pulse time profile, a consequence of the variations in path lengths between regions of the tube face and the first stage of the dynode chain. Cones for the hexagonal PMTs are therefore designed to focus light incident on the whole tube face into a central region of the photocathode, resulting in an improved time profile (see Roberts, 1997a). These cones have enabled a 30% reduction in threshold energy to be obtained. The signals from the PMTs are passed through approximately 50 m of CT100 coaxial cable to the electronics within the Mark 6 container.

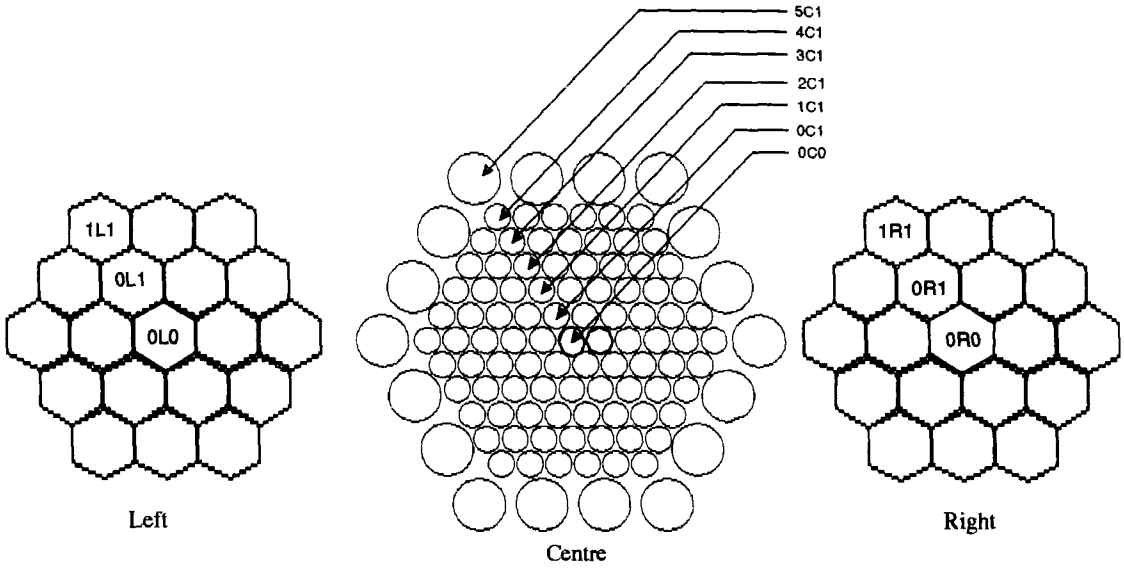

Figure 3.5: The PMT naming system for the three Mark 6 detector packages. The tube number within each ring increases clockwise when viewing the packages from behind.

3.5.2 Electronics and Trigger Criteria

The Mark 6 telescope employs a novel 3-fold spatial plus 4-fold temporal coincidence system. The telescope is triggered when a signal above a set threshold (normally 50 mV) is detected from a corresponding pair of PMTs in the left and right cameras plus two of the seven one inch tubes in the central camera which also correspond to this same region of sky (2-of-7 coincidence), all within 10 ns. This trigger has been designed to be efficient at recording Čerenkov light from EAS initiated by relatively low energy γ-rays. This triggering criterion is illustrated in Figure 3.6

The high voltage for the PMTs is provided by a number of commercial E.H.T. units. The electronics configuration is similar to that in use in the Mark 3 and Mark 5 telescopes. The signals from the PMTs are amplified and passed through a set of discriminators. The output from these discriminators are sent to the trigger logic units and if the trigger criteria has been satisfied the ADCs read out the integrated charge (QT) for each PMT. Along with the QTs, the time, steering and triggering information are recorded by the logger computer. This system is shown

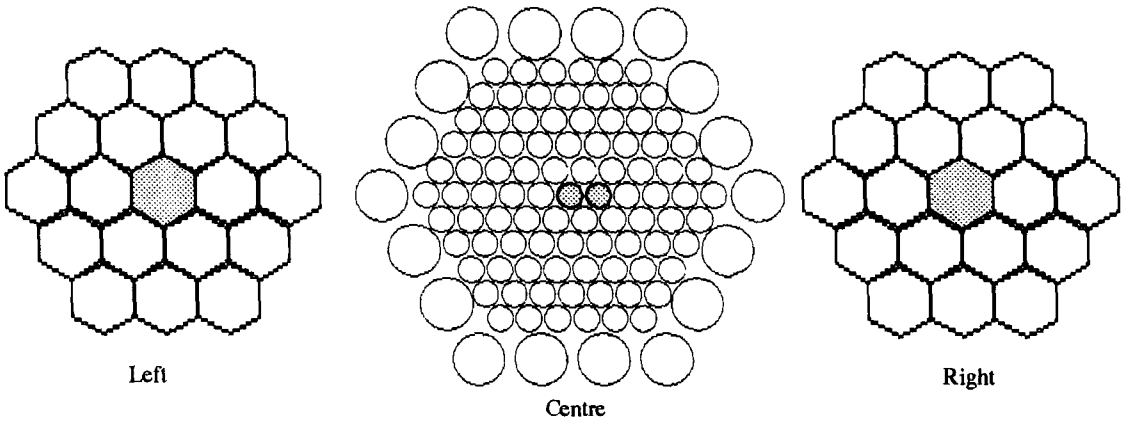

Figure 3.6: A schematic representation of the Mark 6 triggering criteria: signals from associated left and right PMTs plus any 2 of the corresponding 7 central one inch PMTs above a 50 mV threshold (grey tubes), within a 10 ns interval.

schematically shown in Figure 3.7.

The data are logged on a microcomputer which has a dead time of approximately 2 ms. A second microcomputer displays the PMTs anode currents, one-fold rates as well as the three-fold and 2-of-7 coincidence rates. This information is recorded to a file and provides telescope performance information which is used when undertaking analysis.

3.5.3 Steering

The zenith and azimuth D.C. servo motors can supply a maximum torque of 75 Nm. The telescope position is sensed and recorded (within each event) to 14 bit accuracy (0.022°), although the target position is only updated to 12 bit accuracy (0.1°) to reduce excessive motor wear. During 1995, the azimuth drive was fitted with a torque limiter, thereby reducing the possibility of damage to the drive system from excessive forces e.g. due to a sudden gust of wind. The steering is controlled through a dedicated BBC microcomputer. The motor control system is shown in Figure 3.8.

To obtain accurately the absolute pointing position of the Mark 6 telescope a

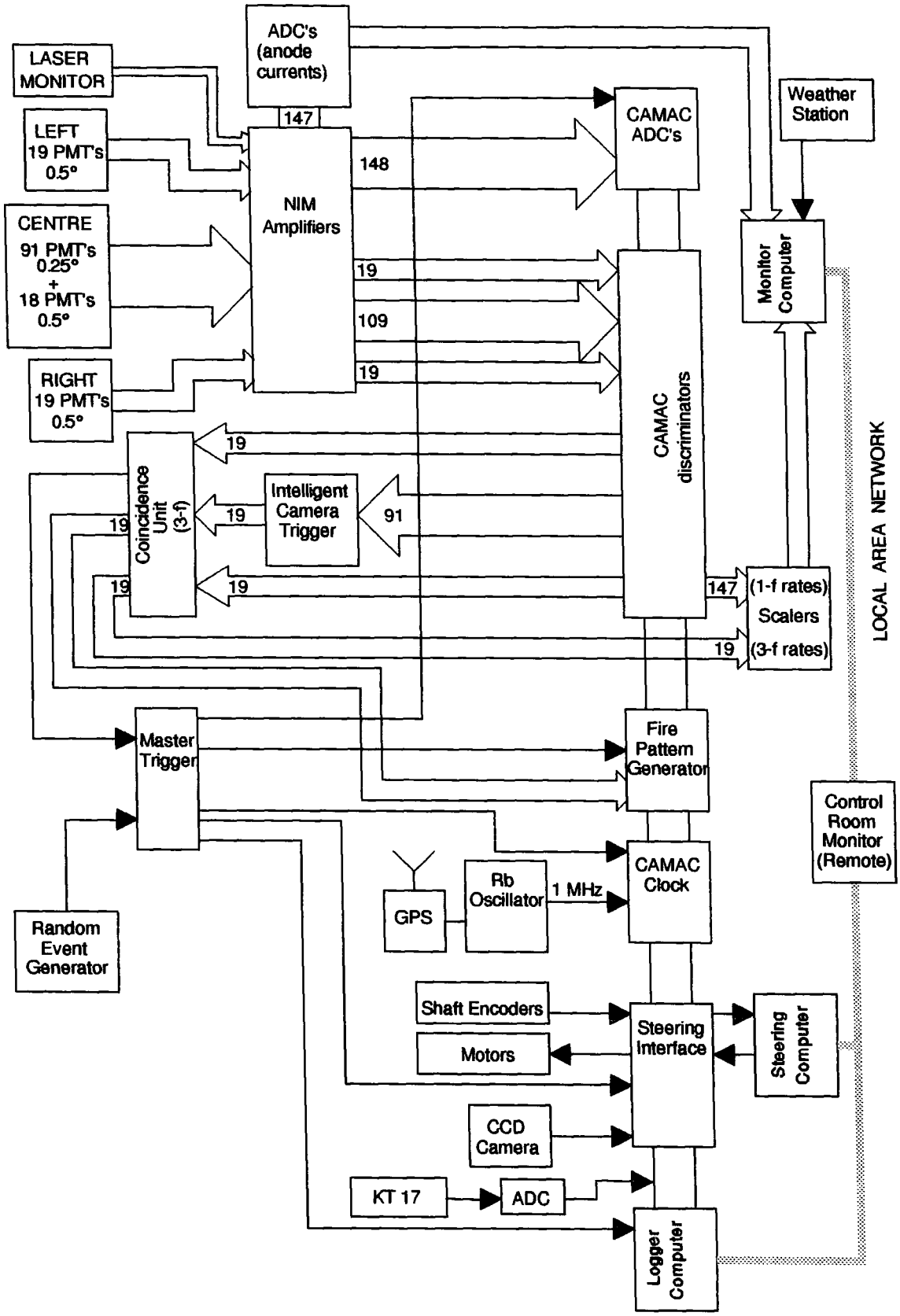

Figure 3.7: A schematic representation of the Mark 6 control and logging electronics. After Dickinson (1995).

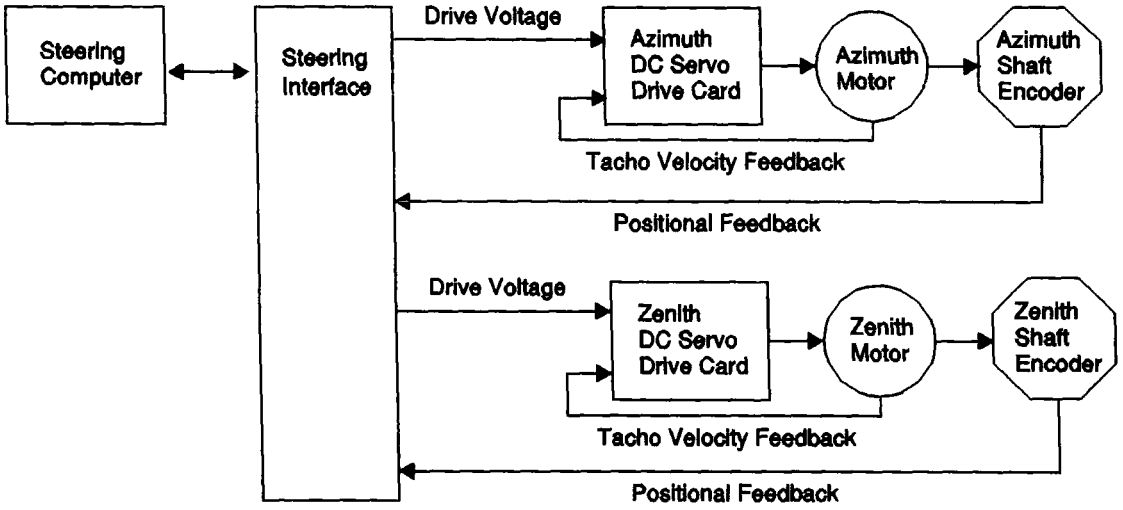

Figure 3.8: A schematic representation of the Mark 6 steering control.

coaxial CCD (with a 2.9° × 2.9° field of view) has been mounted onto the telescope framework. Within each event the (x,y) position of the brightest CCD pixel within the frame is recorded, which can be compared to that expected from a star database. This requires a reasonably bright star to present within the field ($m_V \leq 6$) and provides an independent method for determining to true pointing position of the telescope. At the data analysis stage the offset between the CCD calculated position and the 14 bit shaft encoders is determined for which a best fit parabola is produced. A small second order correction is also applied to account for movement of the central detector package with respect to the optic axis as a function of zenith angle. The size of this second order correction is given by

$$(3 \times 10^{-3}) \times (30° - \text{zenith angle}) \text{ degrees.}$$

The total calculated correction is applied to the encoder positions within each event and as a result the absolute telescope pointing is known to ±0.03°.

Determining the offset between the optic and CCD axes as well as the rotation angle of the CCD chip with respect to the horizontal is critical in this pointing reconstruction method. The offset between the optics axes has been measured with the use of a photodiode placed on the central one inch camera tube. The telescope tracks a known bright star, with the signal from the photodiode indicating the instant when the star as at the centre of the field of view. At this point the brightest

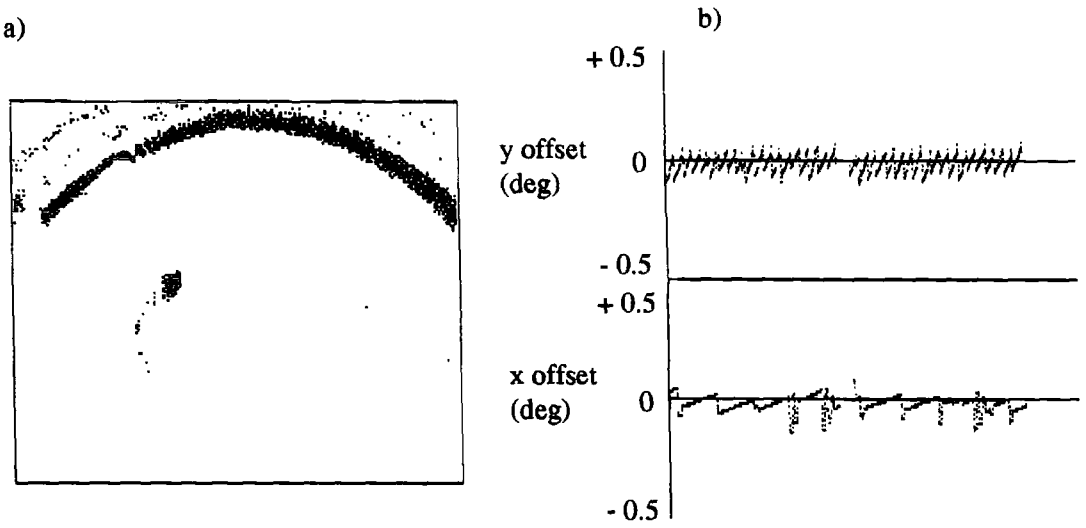

Figure 3.9: a) A reconstruction of the peak pixel position during a tracking run; b) The telescope's x,y position relative to the source, as determined with the 14 bit shaft encoders and CCD information.

pixel within the CCD frame is determined. This process is iterated a number times. The rotation angle of the CCD chip with respect to the horizontal can be determined with the use of a full frame image containing a number of bright stars. This image can be compared to the expected field positions and the rotation angle can be calculated. The reconstruction of the CCD brightest pixel through an observation and the calculated steering offsets with respect to the source position are shown in Figure 3.9.

3.5.4 Environmental Monitoring and Telescope Performance Stability

Various environmental factors can affect both the performance and stability of an atmospheric Čerenkov telescope. For example, sky clarity will have a direct effect on the telescope triggering rate (and therefore threshold energy), while large variations of the temperature within a detector package may produce varying PMT performances. As a consequence, many of these factors are recorded and in a number of situations effort has been directed into reducing any performance fluctuations.

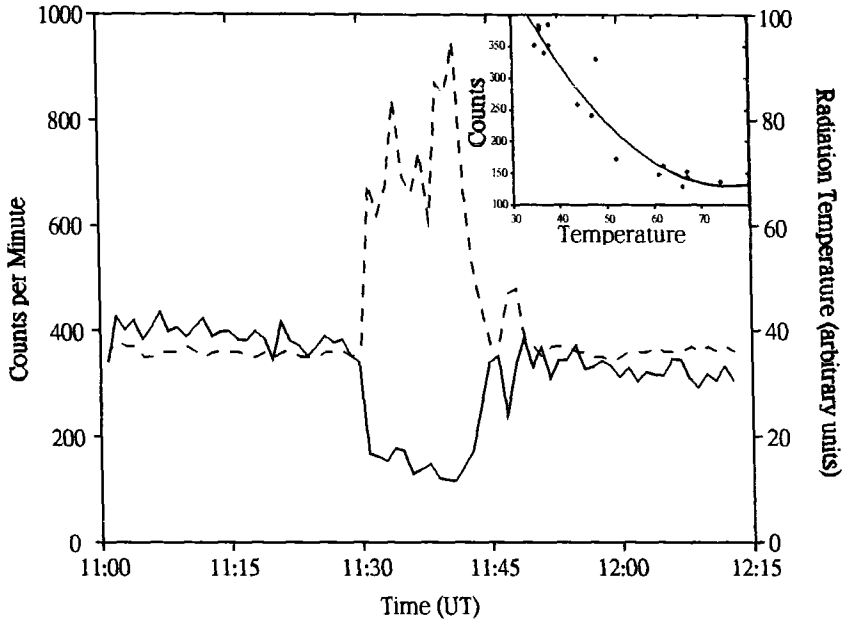

Figure 3.10: FIR radiation temperature (dashed line) and count rate (solid line) during an observation with the Mark 6 telescope. The inset shows the measured relationship between radiation temperature and count rate.

In March 1997, a KT17 far infrared radiometer (FIR) was mounted coaxially on the Mark 6 telescope framework. This provides a direct measure of the sky clarity which is independent of the telescope performance. The radiometer has a 2 degree square field of view and a dynamic range covering $-25\,^{\circ}\mathrm{C} \rightarrow +50\,^{\circ}\mathrm{C}$ (see Roberts, 1997a). Figure 3.10 illustrates the effect of cloud during an observation on both the telescope count rate and the KT17 output. The instantaneous KT17 value is logged within each event (see Figure 3.7).

The temperatures of the electronics within the Mark 6 container, mirror surfaces, detector packages, air and the laser calibration system (see Section 4.1.3) are recorded and displayed on a microcomputer within the Mark 6 control room (this display is also relayed to the central control room). Displayed on this environmental monitoring systems are also the atmospheric pressure, humidity and wind speed/direction.

A system of heaters have been installed within each of the three detector packages in order to reduce large scale temperature variations during observations. These

variations arise from the diurnal air temperature cycle and ohmic heating of the resistors within the PMTs dynode chains. The heaters are switched on three hours prior to astronomical dark and are set to servo at a predetermined temperature for the period of the observation. This will reduce any temperature dependent gain variation of the PMTs.

3.5.5 Data Treatment

The data logged during an observation are recorded on to an internal hard disk within a microcomputer. The format of this data file is designed to keep the dead time for the logger computer to a minimum. Following an observation, the data files are copied over the ethernet network to a second hard disk situated within the central control room. At the end of a three week observing session the data, CCD, housekeeping and environmental monitoring files are transferred onto a DAT for returning to Durham. At Durham the data files are 'formatted'. This process expands the compressed raw data file into a logical file format which is ready for calibration and analysis procedures.

3.6 Observing Techniques

The steering of all three telescopes is controlled by a standard software package. Two general observing techniques are available:

1. Tracking Mode : The source is maintained at the centre of the field of view for the duration of the whole observation.
2. Chopping Mode : The source is tracked for a period of time (normally 15 minutes) and then a field which has a right ascension 15 minutes later than the source position is tracked (ON/OFF). This allows exactly the same zenith range to by covered and a background sample of events to be obtained. If this OFF field contains a bright star for example, then

the field preceding the ON by 15 minute will be used (OFF/ON). Combinations of these two methods have been developed to remove any linear systematic effects (such as temperature variations) from an observation, e.g. ON/OFF/OFF/ON.

The tracking mode is predominantly used for sources from which pulsed emission is expected, the evidence for γ-rays coming from non-statistical features in the period analysis (see Section 4.4). For objects such as AGNs and supernova remnants where no periodicity will be present, the evidence for γ-ray emission has to come from comparisons between the source and a background region. An obvious disadvantage with the chopping technique is that half the duty cycle of the telescope is used observing a region of sky from which no γ-rays are expected. In the chopping mode, 50 seconds of data after the telescope begins to steer to the new position are removed to allow for the telescope slew rate. The data 20 seconds prior to the steer are also removed to account for inaccuracies in the steering computer's clock.

3.7 Threshold Energy Determination

Determining the energy threshold of an atmospheric Čerenkov telescope has a number of inherent difficulties. The only measure of the energy of a primary initiating particle comes from the resultant density and extent of Čerenkov photons produced within the EAS. Folding in the telescope triggering response and detector characteristics makes this indirect method of determining the energy of a primary initiating particle highly inaccurate.

The energy thresholds of the Mark 3 and Mark 5 telescopes have historically been determined on a semi-empirical method. This has involved scaling the measured cosmic ray count rate with reference to an original measurement made with a small array of Čerenkov telescopes situated at Dugway, Utah (Chadwick, 1987). This method produces a threshold energy for cosmic rays. A cascade initiated by a γ-ray will produce roughly twice as many Čerenkov photons as that from a hadron of the

same primary energy. The confined nature and uniform lateral distribution from γ-ray initiated cascades will also produce a higher probability of triggering a telescope system than those showers initiated by cosmic rays.

With the Mark 6 telescope, Monte Carlo simulations have been used as an aid in threshold energy determination (see Holder, 1997). These simulations calculate the shower development and Čerenkov photon production for both primary photons and cosmic rays. For this purpose the MOCCA Monte Carlo code was used (Hillas, 1982). These shower simulations are passed through a model of the Mark 6 to replicate the telescope response. The model input parameters include the mirror point spread function, triggering criteria, discriminator levels, night sky background photon density, mirror collecting area and site altitude. From a sample of simulated cosmic ray showers the discrimination levels are varied until the triggering rate of the telescope model corresponds to that measured experimentally. This telescope model can then be applied to a set of simulated γ-ray initiated showers.

The telescope trigger rate (R_{CR}) for cosmic rays will be determined by

$$R_{CR} = 2\pi \int_0^{\infty} \int_0^{2\pi} \int_0^{\infty} \frac{dF_{CR}}{dE d\Omega} P_{CR}(E, r, \theta)\, r dr\, d\Omega\, dE \tag{3.1}$$

where $dF_{CR}/dEd\Omega$ is the cosmic ray flux and $P_{CR}(E, r, \theta)$ is the detection probability as a function of energy (E), impact parameter (r) and angle of incidence of the shower (θ) with respect to the telescope axis (Köhler *et al.*, 1996). The effective collecting area for cosmic rays can be defined as

$$S_{CR}(E) = 2\pi \int_0^{2\pi} \int_0^{\infty} P_{CR}(E, r, \theta)\, r dr\, d\Omega \tag{3.2}$$

and the trigger rate can now be expressed as

$$R_{CR} = \int_0^{\infty} \frac{dF_{CR}}{dE d\Omega} S_{CR}(E)\, dE. \tag{3.3}$$

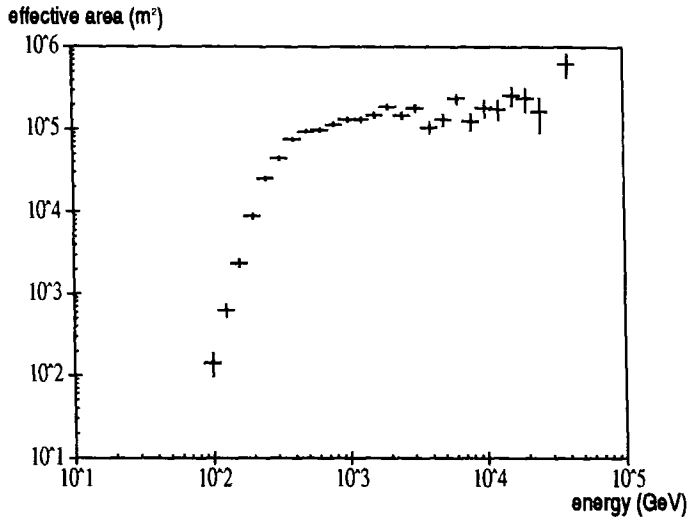

Figure 3.11: The simulated effective collecting area for γ-rays with the Mark 6 Telescope as a function of primary energy. From Holder, 1997.

As γ-rays are assumed to originate from a point source, the effective collecting is given by

$$S_\gamma(E) = 2\pi \int_0^\infty P_\gamma(E, r)\, r dr. \tag{3.4}$$

Simulations of 40000 cosmic rays were generated between 200 and 10^5 GeV with the telescope inclined at 20° to the zenith. These showers were produced over a 2° circular field of view and with impact parameters extending to 250m. The application of the refined telescope model provided by these cosmic ray simulations was then applied to 50000 γ-ray initiated EAS. These showers were generated with energies between 100 and 10^5 GeV and with a power law spectrum of -2.4 (the measured Crab differential spectrum; Vacanti *et al.*, 1991). The effective collecting area for γ-ray initiated showers is obtained by numerically integrating equation 3.4 (see Figure 3.11).

The energy threshold of an atmospheric Čerenkov telescope can be defined as the energy at which the differential flux for γ-rays is a maximum (Aharonian *et al.*, 1995). This is shown in Figure 3.12, the simulations suggest a γ-ray energy threshold of $\sim$ 300 GeV. A number of systematic errors can be assumed to be present

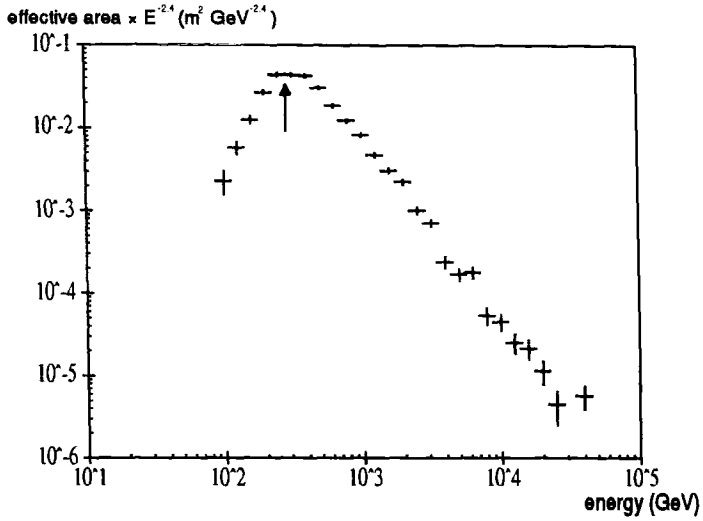

Figure 3.12: Threshold energy of the Mark 6 telescope as defined by the maximum in the differential flux. A source differential spectral index of -2.4 has been assumed. The threshold energy is therefore calculated as 300 GeV. From Holder, 1997.

in our simulations and telescope model. A conservative estimate of the error in the energy threshold determined is ± 100 GeV.

Chapter 4

Calibration and Analysis Techniques

High resolution telescopes utilising the ACT have typically between 109 and 588 photomultipliers tubes (PMTs) acting as imaging elements. In this chapter the calibration of these PMTs and the analysis techniques applied to the data will be discussed. Two distinct methods of image parameterization will be outlined, a traditional moment analysis (Section 4.2.1) and a bivariate Gaussian fit to the Čerenkov image (Section 4.2.2). Methods of searching for periodicity within data will also be introduced.

This chapter will conclude with a set of parameter selections which are expected to reject a large fraction of hadronic events while retaining the majority of any γ-ray signal.

4.1 Data Calibration

To produce an accurate image reconstruction of the Čerenkov light emitted within an EAS, calibration procedures must be undertaken to account for individual PMT characteristics and offsets within the electronics units. After calibration, the array

of imaging elements will produce a flat field in the absence of any Čerenkov photons (except for fluctuations in the night sky background) while responding uniformly over all elements to Čerenkov photons.

4.1.1 Pedestal Determination

An artificial DC offset (pedestal) is applied to the charge digitizer units to stop any negative signals being recorded due to downward fluctuations in the night sky photon background. The pedestal is determined by randomly triggering the telescope to produce a 'null event' (the random event generator is shown in Figure 3.7). The signal (QT) determined for each PMT from these 'null events' will be a combination of the artificial DC offset and the night sky photon density.

A 'null event' produced by a random trigger is flagged with the coincidence unit, allowing its easy removal prior to any analysis procedures. From these 'null events' a histogram of the QT of each PMT is produced (see Figure 4.1), from which the pedestal (the mean of the distribution) and the noise due to night sky photon fluctuations can be determined. The calculated pedestals are removed from the QTs of each event produced by Čerenkov light and the noise is used in the moment parameterization (see Section 4.2.1). The telescopes are randomly triggered at a rate of 50 min^{-1}, providing the statistics needed to determine the pedestal on a 15 min timescale.

If these random events are unavailable, a technique has been developed for determining the pedestals using events containing Čerenkov light. Events are selected in which only one of the outer channels has triggered. It is assumed that the light from such an event will be confined within this small triggered area of the camera. As a result, the signals recorded from the PMTs on the opposite side of the camera will be due to only the DC offset and the night sky contribution. For PMTs close to the centre of the camera the Čerenkov light will begin to make a contribution to the measured QT. A parameter fit has been developed to account for this Čerenkov light contamination.

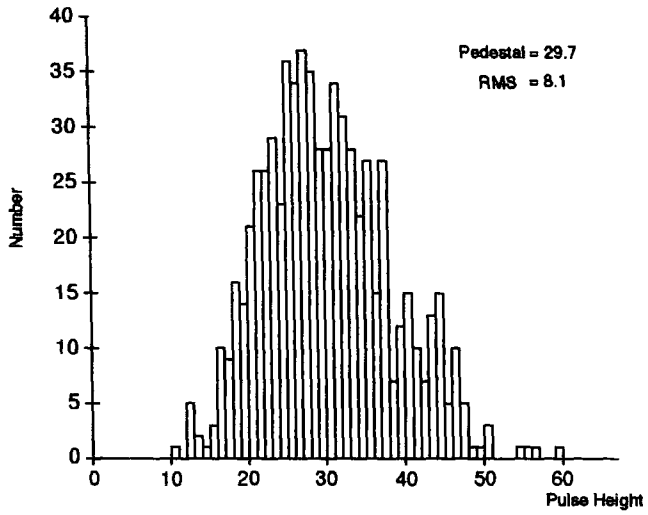

Figure 4.1: The pulse height distribution from 650 'null events' (a standard 15 min sample) for a typical 1 inch PMT in the central Mark 6 detector package. The pedestal is defined as the mean of the distribution and the spread (noise) is due to fluctuations in the night sky photon density.

4.1.2 Software Padding

As will be discussed in further detail in Section 4.2.1, the moment imaging technique relies upon the Čerenkov signal within the PMTs being significantly larger than the noise due to the night sky photon background (typically Nσ above the pedestal, where σ is a measure of the noise). PMTs which do not pass this fixed threshold are treated as having a signal of zero. When observing in a chopping mode (see Section 3.6), brightness difference between the ON and OFF fields will result in variations in the measured sky noise, affecting the image parameterization.

A Čerenkov signal in a tube with a low level of sky noise (a dark field) will pass a fixed threshold to become a part of an image with a greater probability than that for a tube with a large sky noise contribution (a bright field), see Figure 4.2. A brighter field will result in fewer PMTs on average being included in an image compared to a dark field. This will lead to systematic parameter differences between the ON and OFF fields, resulting in biases when performing event selections within parameter space.

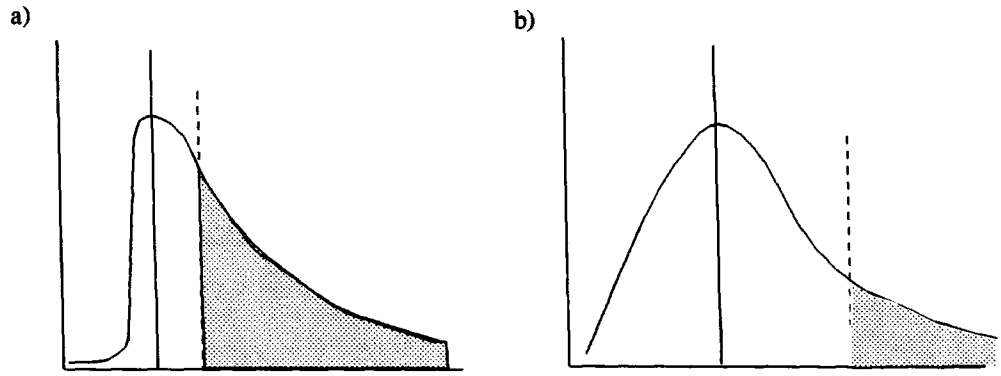

Figure 4.2: a) A tube with a small sky noise component b) A tube with a high level of sky noise. Using a threshold which scales with the noise level, the number of occasions when a tube exceeds this threshold will be less in (b) than in (a). From Cawley (1994).

Historically, to overcome this problem, padding lamps consisting of LEDs placed close to the photocathode of each PMT, were used to provide a constant illumination (and therefore constant noise) across the tube faces. This became impractical with the number of PMTs within a high resolution camera. Punch (1993), suggested a method of replicating the effect of padding lamps within software. This software padding procedure artificially adds noise to PMTs in the dark field, therefore padding the noise level up to that in the bright field. For example, the total ON signal for a tube is given by

$$ON = P_{ON} + \sigma_{ON}\text{Gauss}(0:1) + C_{ON} + \sqrt{C_{ON}}.\text{Gauss}(0:1) \qquad (4.1)$$

where P is the pedestal, σ is the noise and C is the Čerenkov signal. The noise component due to the night sky background is given by

$$N_{ON} = \sigma_{ON}\text{Gauss}(0:1) \quad \text{and} \quad N_{OFF} = \sigma_{OFF}\text{Gauss}(0:1)$$

If N_{ON} is larger than N_{OFF} (due to a bright star for example), noise needs to be injected (N_{ADD}) to the OFF field, so that

$$(N_{ON})^2 = (N_{OFF})^2 + (N_{ADD})^2$$

$$N_{ADD} = \sqrt{((N_{ON})^2 - (N_{OFF})^2)}$$

The total OFF signal is therefore given by

$$OFF = P_{OFF} + \sigma_{OFF}\text{Gauss}(0:1) + N_{ADD}\text{Gauss}(0:1) + C_{OFF} + \sqrt{(C_{OFF})}.\text{Gauss}(0:1)$$

The reverse is applied if a PMT in the OFF field has a larger noise than in the ON.

4.1.3 PMT Gain Determination

The relative gains of the individual PMTs are determined to allow a flat field response to be obtained from a uniform photon density over the detector. This enables a true representation of the Čerenkov light from an EAS to be obtained.

The PMTs will have different gains due to the variable voltage at which the tubes are operated, construction of the individual dynode chains, degradation of the photocathode resulting in a reduction in the quantum efficiency and gas leakage into the vacuum separating the anode and cathode. In the case of the Mark 6 telescope, the one inch PMTs are assigned a relative gain with respect to the central tube (0C0), the gains of the two inch guard ring tubes are given relative to 5C1 and the left and right hexagonal tubes are relative to 0L0 and 0R0 respectively (the PMT naming nomenclature is shown in Figure 3.5). For the purpose of data analysis, the 2 inch 'guard ring' PMTs (5C1→5C18) are treated as one inch PMTs with the application of a form factor. This form factor accounts for the difference in photocathode area and intrinsic performance characteristics. Two methods are currently used to determine the relative gains of the PMTs.

In-Flight Laser Gains

A nitrogen laser (VSL model 33700) mounted onto the telescope is used to produces a 3ns, 40 kW pulse of 337 nm radiation, which is presented to a plastic scintillator.

This scintillator produces light in the 400±20 nm range which is transmitted through three plastic optic fibres to opal diffusers positioned at the center of each mirror. These diffusers produce a uniform illumination over the detector packages and by measuring the response of each PMT the relative gains to be determined.

During a typical observation the laser unit produces pulses separated by a random interval with a mean rate of 50 min^{-1}. The pulse produced is bright enough to trigger the telescope system and these events are flagged by the coincidence unit for their easy removal prior to analysis.

Cosmic Ray Gains

If the laser system is unavailable, the relative gains are determined with the aid of cosmic ray events, based on a procedure suggested by Punch (1993). If it is assumed that the detector package is free from triggering biases, the PMTs should be subjected to a uniform average illumination of Čerenkov light produced by cosmic ray events.

The integral distribution of signals from the PMTs are produced for cosmic ray events. The QT range over which this integral distribution falls from 30% to 5% of the maximum is equated to the gain of that PMT (see Figure 4.3). This region of the integral spectrum is chosen so as to be removed from small flashes where triggering biases become important. This technique is applied for the gain calibration of the Mark 3 and Mark 5 telescopes. The difference between the relative gains determined by the laser and cosmic ray methods is shown in Figure 4.4

4.1.4 Steering Offset

The accurate pointing information obtained from the coaxial CCD (see Section 3.5.3) and the 14 bit shaft encoders is used to determine the exact source position with respect to the centre of the detector package. This allows the image parameterization to be undertaken relative to this source position and not the geometrical centre of

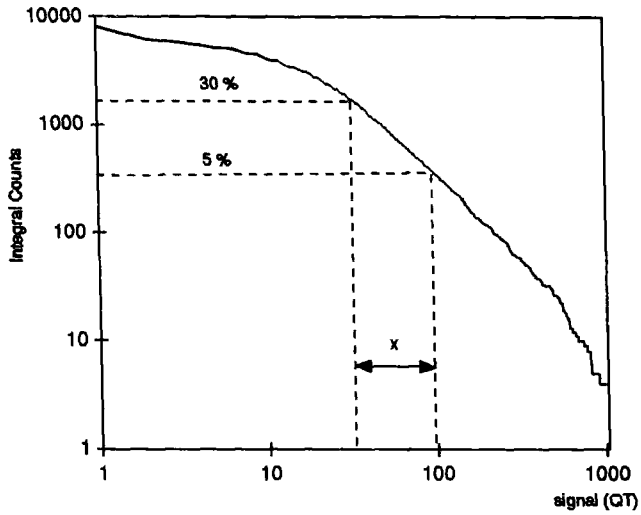

Figure 4.3: Gain calibration using the cosmic ray beam. The gain of the PMT is assumed to be represented by the QT difference between the 30% and 5% level of the integral pulse height spectrum (x). This value is compared to that determined for tube 0C0 to provide a relative gain.

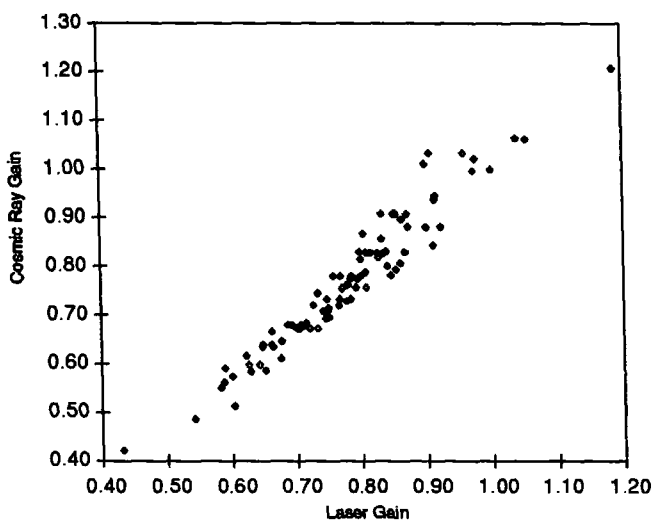

Figure 4.4: Comparison of the relative gains determined for the one inch central PMTs by the in-flight laser and cosmic ray methods.

the camera. This becomes particularly important when using the parameter *alpha* (the angular alignment between the major axis of the fitted ellipse and the source position, see Section 4.2.1).

4.2 EAS Imaging

In order to improve the signal to noise ratio of γ-rays over the abundant hadrons, methods of parameterizing the Čerenkov images of EAS have been developed. The discrimination between γ-rays and hadrons arises from the inherent differences in shower development, described in Section 2.3.1.

The most successful method used to date has been the 'moment' parameterization technique, which has been used in the detection of the Crab Nebula, PSR 1706-44, Mrk 421 and Mrk 501. Although this technique has been proven to be extremely efficient at γ-ray and hadron separation, it does suffer from a number of inherent limitations. For this reason, alternative parameterization methods have been introduced, including the bivariate Gaussian fitting technique developed within the University of Durham group (Section 4.2.2).

The discrimination power of an analysis technique can be quantified by its quality factor (Q-factor), as defined by Fegan (1992):

$$Q = \frac{\eta^{\gamma}}{\sqrt{\eta^{N}}} \tag{4.2}$$

where η^{γ} and η^{N} are the fraction of γ-rays and hadrons retained after parameter selections respectively.

4.2.1 Moment Analysis

Hillas (1985) proposed that, based on studies of γ-ray and hadronic Monte Carlo simulations, the Čerenkov image formed from an EAS could be parameterized by standard moment procedures. The parameters derived from this method have been termed as 'Hillas image parameters' and are shown in Figure 4.5 and defined in Table 4.1. Additional parameters have since been derived, including

$$alpha = \sin^{-1} \frac{Miss}{Distance}.$$

This is the angle between a line joining the source position and the image centroid to the major axis of the fitted ellipse.

Hillas showed that significant discrimination between γ-ray and hadronic initiated cascades could be achieved by performing a selection in multidimensional moment parameter space. In particular γ-rays were shown to have a tendency to be aligned towards the source position, i.e. low values of *alpha*.

Typically PMTs are included within the moment calculation if they have a signal greater than 4.25 σ (termed an 'image' tube), or 2.25 σ ('border' tube) which is also adjacent to an 'image' tube, where σ is the measure of the noise for that PMT. The Whipple collaboration using a highly refined set of moment parameter selections ('Supercuts'), achieve a 99.7% hadronic rejection while retaining 50% of any γ-rays (McEnery *et al.*, 1997).

The imaging criteria applied to data obtained with the Mark 6 telescope has been refined to account for small optical aberrations produced by the central mirror. Figure 4.6 shows the point spread function for the central Mark 6 mirror. It can be seen that a single Gaussian cannot account for the overall shape of this image. It is therefore expected that a small amount of light contamination into tubes surrounding the 'true' image will occur. To account for this effect, the image tubes are defined as having a signal which is larger than 37.5% that of the highest tube QT, while border tube have a signal greater than 17.5% of this maximum value. The imaging criteria will relax back to the fixed noise thresholds (4.25σ; 2.25σ), when

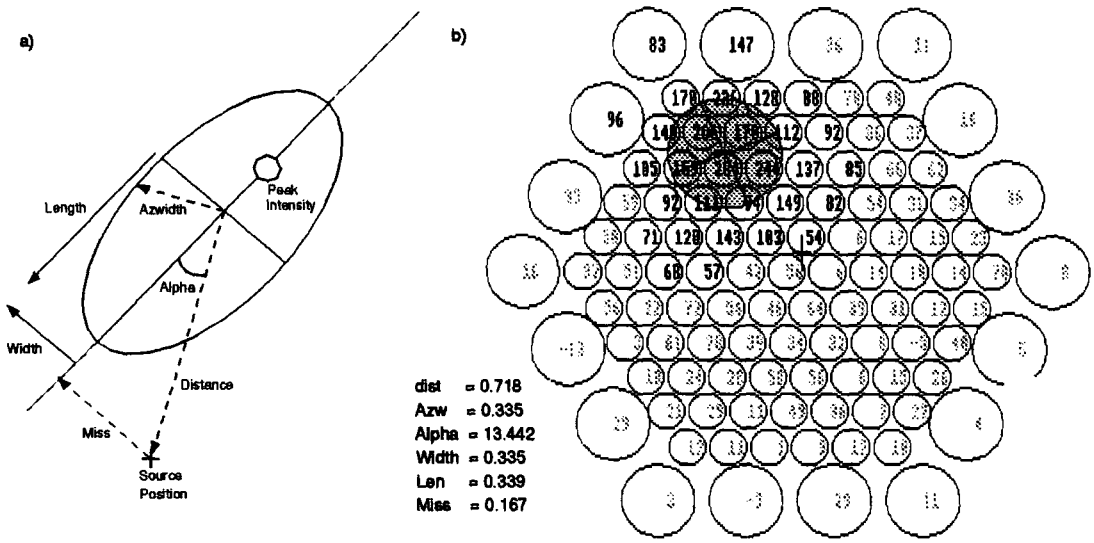

Figure 4.5: a) The definitions of the Hillas image parameters. b) A typical Mark 6 event, with both the moment fit and derived parameters shown (the imaging criteria is as described within the text).

Table 4.1: Definition of the Hillas parameters

Parameter	Definition
Width	RMS spread of the light along the image's minor axis
Length	RMS spread of the light along the image's major axis
Miss	Angular distance between the major axis and the centre of the field of view
Azwidth	RMS image width relative to an axis joining the centre of the field of view and the centre of the image
Distance	The angular separation of the centroid from the centre of the field of view

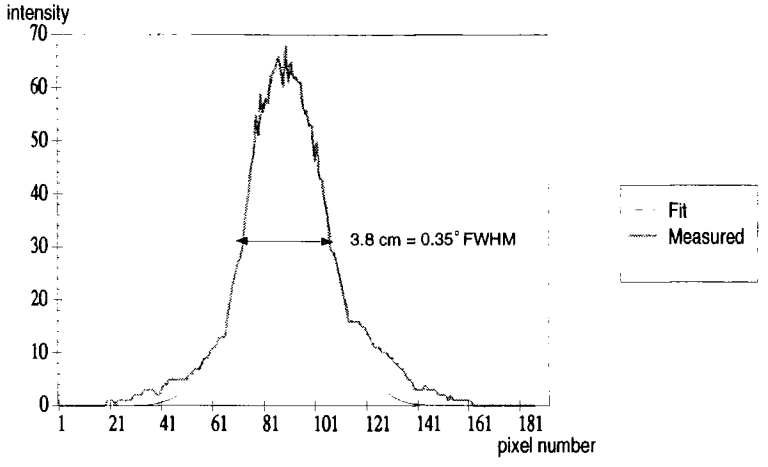

Figure 4.6: A cross section of an image of Jupiter formed with the Mark 6 central mirror (taken with a CCD mounted on the telescope framework). The inability to fit this point spread function with a single gaussian has led to the development of the percentage criteria for image and border tube definitions.

this value is larger than that determined with the percentage method (Figure 4.7 shows a flow diagram for the procedure of assigning image and border tubes) .

4.2.2 Bivariate Gaussian Fitting

Although the moment parameterization technique has been highly successful at enhancing a small γ-ray signal from within the background cosmic ray events, it does have a number of inherent limitations:

1. The moment technique arbitrarily assigns threshold QT values for the inclusion of a tube within an image. The tubes used in the moments calculations are: tubes in which the signal is well removed from the noise (image tubes) or is still the dominant component (border tubes). The signal from all other tubes are essentially set to zero for the moment calculation purposes. This removes a large amount of information contained within tubes which either have roughly equal measures of signal and noise or are noise dominated.

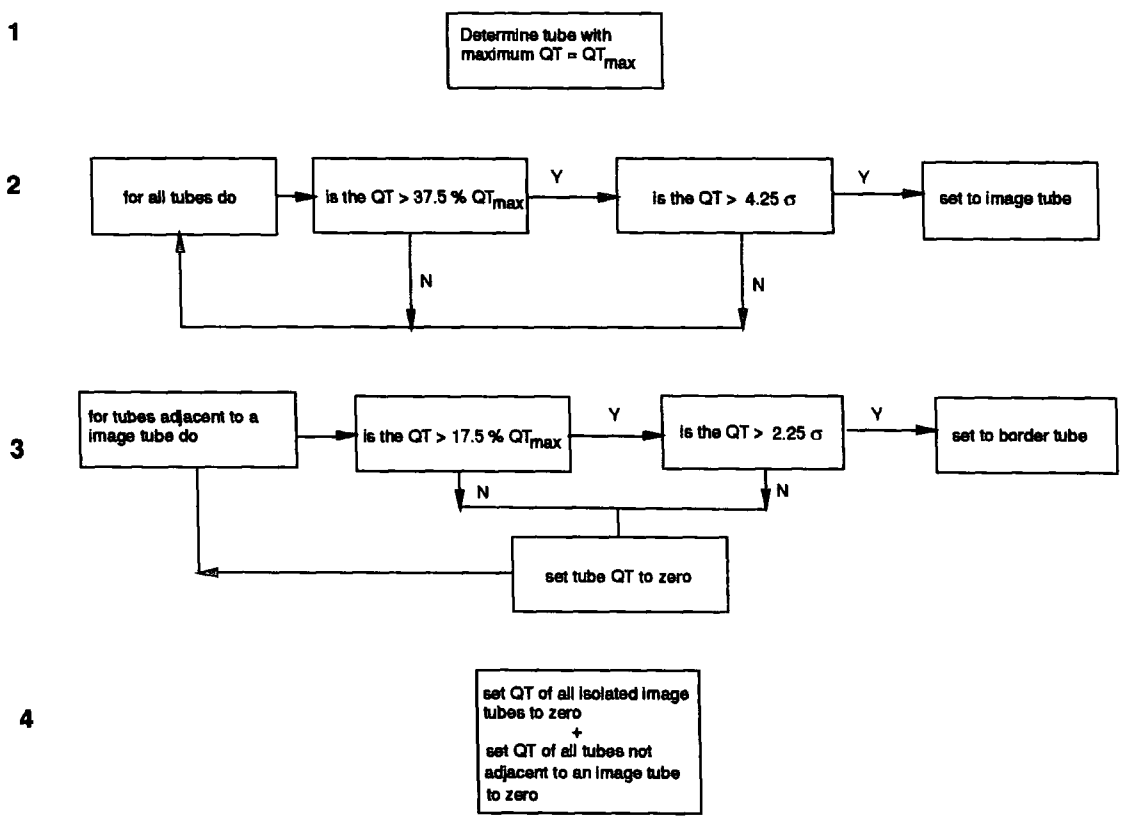

Figure 4.7: A flow diagram showing the four stages for determining the image and border tubes.

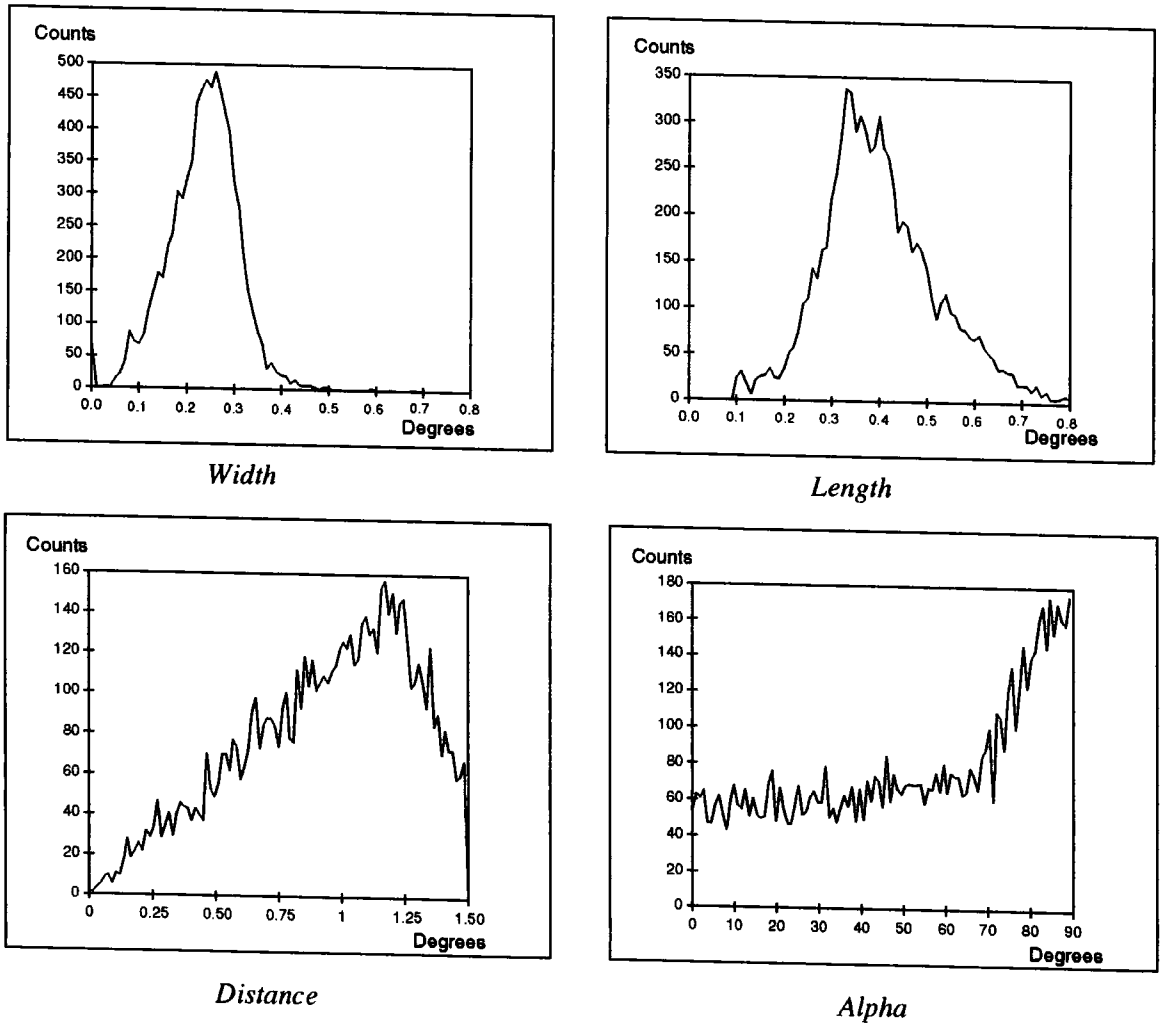

Figure 4.8: Parameter distributions for the hadronic background, using the percentage imaging criteria.

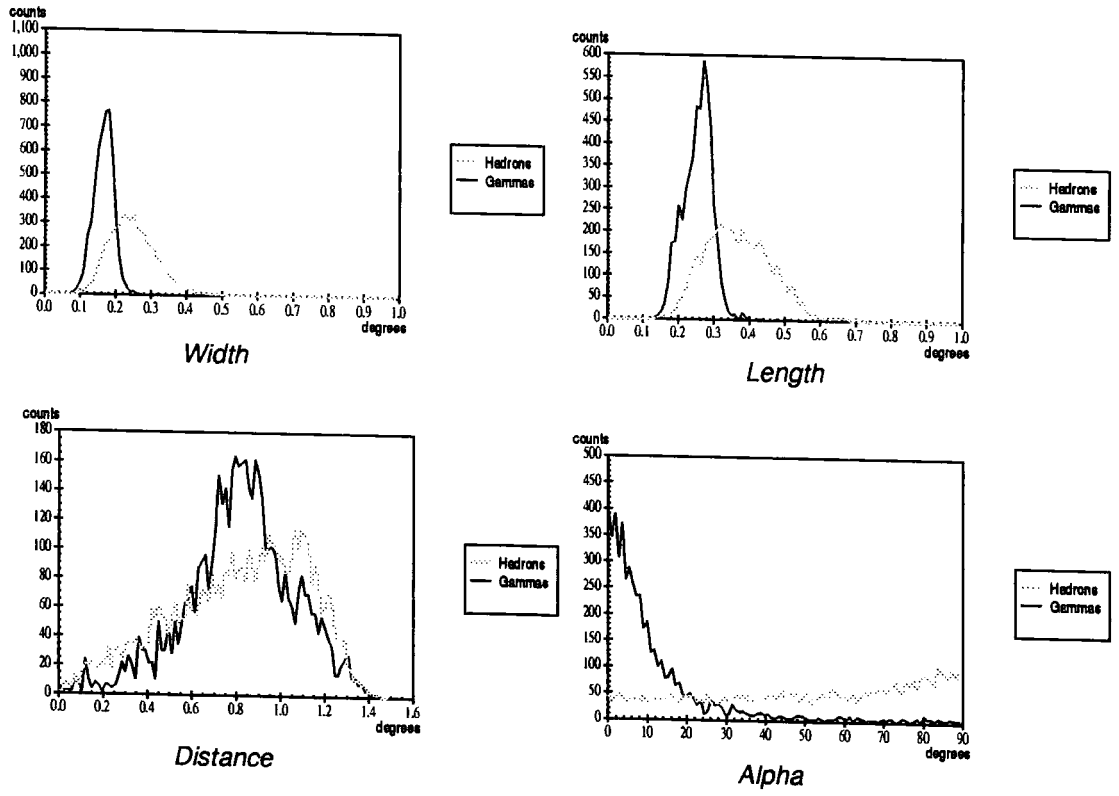

Figure 4.9: Normalised parameter distributions for simulated hadron and γ-ray images calculated using the percentage moment procedure.

2. It is assumed in the moment calculation that the Čerenkov light from an EAS will be confined within the whole camera. This is obviously incorrect. In practice to overcome this problem a selection on the *distance* parameter is made, to only analysis events in which the centroid of the image is well confined within the camera. This again does not make use of the full information available.

For these reasons, the Durham group have developed an alternative analysis technique. This employs the fitting of a smoothing function to the signals from all the tubes within the central detector package. For this purpose, a bivariate gaussian fitting function has been used (for full details see Holder, 1997). This function has the benefit that it has no variable moments higher then second order, thus allowing direct comparisons with the standard second order moments (e.g. *Width* and *Length*).

Holder (1997), presented the preliminary analysis of PSR 1706-44 carried out with both the standard moment and bivariate Gaussian fitting techniques. It was shown that the detection of this object was marginally less significant using this new fitting technique than with the standard moments. It should be noted that a number of alternative imaging techniques have been developed and tested by various groups, but to date no method has been found that can produce a larger Q-factor (see equation 4.2) than that for the standard moment analysis (for examples see Fegan *et al.*, 1995).

The power of the bivariate fitting method becomes apparent when plotting the parameter *alpha* as a function of *distance*. Geometrical effects within the camera can produce biases in parameter distributions using the standard moment analysis. For example, images with centroids close to the edge of the camera will have preferences for *alpha* towards 90° (parallel to the edge of the detector package), due to image truncation in the radial direction. The bivariate Gaussian fitting method does not suffer from this limitation, as it models the expected photon density outside the the detector package, as seen in Figure 4.10. The ideas presented in this section are

currently being developed and updated by members of the Durham group.

4.3 Analysis Of DC Emission

For sources in which any γ-ray emission is expected to form a steady DC flux, a chopping observing technique is utilised, described in Section 3.6. This allows the source to be tracked for a period of 15 minutes, followed by a corresponding OFF region of sky. The ON and OFF source regions are calibrated and the same moment parameter selections are used on data from each field. Evidence for possible γ-ray emission arises from any excess in the number of events passing the parameter selections from the ON field over that from the background OFF field. The significance of any excess is calculated by:

$$\sigma = \frac{N_{ON} - N_{OFF}}{\sqrt{N_{ON} + N_{OFF}}} \tag{4.3}$$

where N_{ON} and N_{OFF} are the number of events passing the parameter selections for the ON and OFF fields respectively.

4.4 Searching For Pulsed Emission

For sources such as pulsars and X-ray binaries, the possible pulsed nature of any VHE γ-ray emission has been used as an aid to improve the poor signal to noise inherent within the observations. This technique has been pioneered primarily by the Durham and Potchefstroom groups and was extensively used during the 1980s as a powerful discriminant.

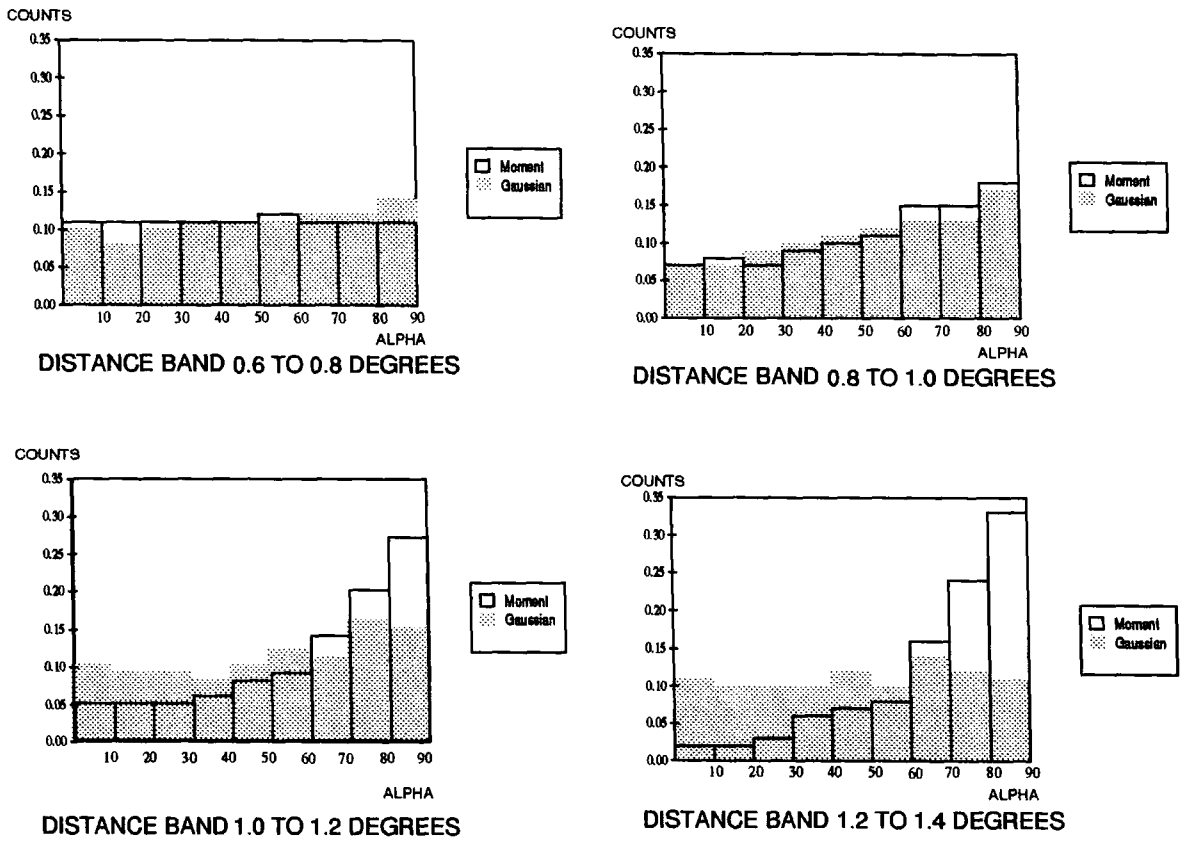

Figure 4.10: Plots of the parameter *alpha* as a function of various *distance* bands. With the standard moments analysis, at large values of *distance* a bias towards 90° *alpha* is observed. With the bivariate Gaussian fitting method, the *alpha* distribution remains uniform across all the *distance* ranges. From Holder (1997).

Barycentering

In order to undertake sensitive analysis using event arrival times, various corrections need to be applied to artificially replicate a stationary detector with respect to a source. This process is termed as barycentering.

The barycentering alteration to the recorded event arrival times has to be applied after the CCD steering correction has been determined, as the latter requires the correct absolute time to calculate the expected positions of the field stars within the CCD camera (see Section 3.5.3). The Durham group uses the JPL DE200 Earth ephemeris (Standish, 1982), to barycenter with respect to the centre of the solar system. This process has 3 stages:

1. To correct for the motion of the telescope about the centre of the Earth. This requires the exact detector position on the Earth's surface, which is provided by the GPS system (≤ 0.021 s).
2. To correct for the effect to the Earth's orbital motion (≤ 500 s).
3. To remove the relativistic effects due to the Earth's motion about the Sun (≤ 0.003 s) (Mannings, 1990).

When observing systems such as X-ray binaries, the orbital motion of the source has to be account for. For details of this procedure see Carramiñana (1991).

4.4.1 Phase Sensitive Analysis

Depending upon the type of object and precision of the known period, various analysis procedures are appropriate. Pulsars have very steady known periods and are closely monitored at various wavelengths, so for these sources an epoch folding method can be used. For sources such as X-ray binaries, for which the period and orbital parameters are often poorly determined, circular statistics can be invoked. For extensive details of these tests see Carramiñana (1991).

Epoch Folding

This procedure provides a simple test for periodicity from sources with steady well known periods. A relative phase is assigned to each event based on its arrival time. By summing the number of events which occur within each phase interval, an overall lightcurve is produced. Comparing this derived light curve to that of a uniform distribution, it is possible to test for evidence of periodicity. The Pearson's χ^2 test is often used for the purpose, determining the significance of any deviations from the expected uniform distribution (Leahy *et al.*, 1983).

For objects in which the shape and size of the expected light curve is known, the size and position of the phase bins can be determined *a priori* and the maximum statistical significance can be gained. If on the other hand the light curve it not so well known, then any signal maybe split between two neighbouring phase bins. Rebinning the data into narrower phase bins will result in an overall lower statistical significance due to the number of degree of freedom introduced.

The Rayleigh Test

Circular statistics can be used for sources in which the light curve is poorly defined, removing the need for arbitrary phase binning invoked in the epoch folding method. The Rayleigh test was first applied to VHE γ-ray astronomy by Gibson (1982). In this test, the time of arrival is represented by a radial vector at a phase angle ϕ, with respect to an arbitrary phase. The radial vectors are summed, producing a resultant vector (R). The modulus of this vector is divided by the number of events, N, to give a normalised value of R, between 0 and 1

$$\mathrm{R} = \frac{1}{N}[(\sum_{i=1}^{N} \cos\phi_i)^2 + (\sum_{i=1}^{N} \sin\phi_i)^2]^{\frac{1}{2}} \quad . \tag{4.4}$$

For a large number of events ($N \geq 100$), the parameter $2N\mathrm{R}^2$ is distributed approximately as a χ^2 distribution with two degrees of freedom and the probability

of obtaining a particular value is given by

$$Pr(\geq 2N\mathrm{R}^2) = e^{-N\mathrm{R}^2}, \tag{4.5}$$

where $N\mathrm{R}^2$ is known as the Rayleigh power. Short exposures and varying count rates due to zenith angle variations can introduce artificial biases into the χ^2 distribution. The first of these problems can be overcome by reducing the data to an integral number of test periods (Poincaŕe's correction). Orford (1996), has suggested a method of producing corrected χ^2 distributions for datasets of finite size and varying count rates.

4.5 Parameter Selections

It was shown in Section 2.2.3 that the EAS formed by γ-rays and cosmic rays are fundamentally different. These differences will be evident in the Čerenkov images formed of these showers. The Hillas image parameter distributions of simulated γ-ray and cosmic ray primaries are shown in Figure 4.9.

In order to improve the signal to noise ratio, parameter selections are applied to reject a large fraction of the background hadronic events while retaining the γ-ray initiated showers. These selections can be based upon physical arguments and information gained through simulations.

The parameter selections applied to data collected with the Mark 6 telescope are shown in Table 4.2. The justification for each of these selections is as follows:

1. *Distance* : 'Standard' Hillas parameter as defined in Table 4.1. The lower distance limit removes events that originate from the source region that also have small impact parameters (e.g. showers which fall very close to the telescope). The Čerenkov image of a γ-ray in this range is expected to be circular and as a result the error in the calculated parameter *alpha* is large. The outer limit removes events that fall close to the edge of the

detector. The image of these rejected events are generally truncated in the radial direction.

2. *Eccentricity* : Ratio of *Length* over *Width*. The upper limit removes images that are approximately circular, for which the parameter *alpha* is poorly known. The lower limit is used to reject events which trigger two distinct regions of the detector, as sometimes expected in images of hadronic initiated cascades. These events will have a tendency to large values of *Length* compared to *Width*, as the major axis of the fitted ellipse will join these two separated regions.

3. *Ddist* : The angular separation between the image centroids in the left and right flux collectors. Cosmic ray initiated cascades will tend to larger values of *Ddist* than that for γ-rays, as fluctuations in the light pool density over the 14 metre baseline between the left and right flux collectors will become significant (Shaw, 1997).

4. *Camera Sum* : The sum of the total signals recorded within all the central camera PMTs. As no arbitrary imaging criteria are used in the calculation of this parameter, it provides the most accurate measure of the total light detected and therefore the 'size' of the event. A feature of the 3-fold coincidence system utilised by the University of Durham telescopes is the gradual rise in the triggering probability as a function of particle primary energy compared to that for a single dish. This produces second order moment parameter distributions (*Length* and *Width*) which vary considerably with primary energy (see Figure 4.11). The data are therefore split into 5 size bands to account for the change in the expected γ-ray parameter distributions as a function of energy.

5. *I ratio* : The ratio of *Camera Sum* less the total signals within the image and border tubes (QT_{total}) over *Camera Sum*. This provides a measure of the amount of light falling outside the image and border region. The relatively compact images formed from γ-rays are expected to tend towards low values of *I ratio* compared to images of cosmic ray cascades of the same energy. The values of *I ratio* shown in Table 4.2 were de-

Table 4.2: Parameter Selections

Distance			$0.35 \rightarrow 0.85$		
Eccentricity			$0.35 \rightarrow 0.65$		
Ddist			< 0.15		
Camera Sum	200-800	800-1500	1500-3000	3000-5000	> 5000
I ratio	< 0.7	< 0.45	< 0.2	< 0.15	< 0.1
Width	< 0.13	< 0.22	< 0.255	< 0.315	< 0.34

veloped on the 1996 PSR 1706-44 dataset. This parameter is similar to the *Concentration Ratio* parameter used by the Whipple collaboration (Catanese, 1996).

6. *Width* : 'Standard' Hillas parameter as defined in Table 4.1. The narrowly confined EAS formed by a γ-ray primary will tend to small values of *Width*, a fact supported by simulations (see Figure 4.9). The median value of the *Width* distribution for each *Camera Sum* size band is applied as an upper bound. An upper limit *Width* parameter selection is utilised by all groups using high resolution Čerenkov telescopes.

Events are therefore selected which are relatively small, elliptical, well confined within the camera, have a large fraction of the light confined within the image tubes and good left-right correlation.

Events are then selected with values of the *alpha* parameter less than 22.5° as γ-ray candidates. These parameter selections have resulted in a 5.0σ detection of PSR 1706-44 from 10 hours of ON source data. This confirms the previous CANGAROO VHE γ-ray detection of this object (Kifune *et al.*, 1995). This data were obtained with the Mark 6 telescope during the 1996 observing season, for full details of this analysis see Chadwick *et al.* (1997). A Q-factor of 5 is estimated from this data analysis.

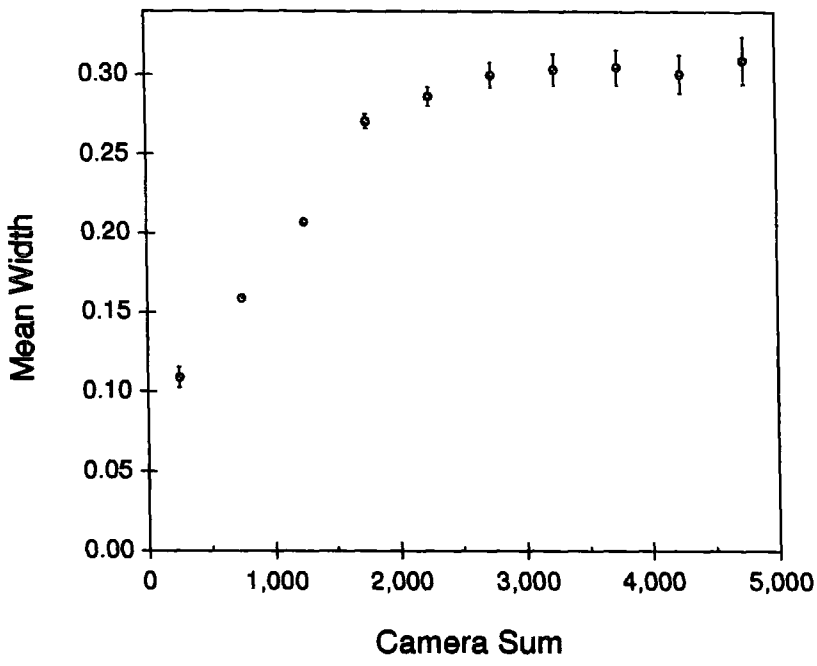

Figure 4.11: Variation of mean *width* as a function of *Camera Sum*. This is a result of the gradual rise in triggering probability inherent with a 3-fold coincidence system

4.6 Summary

In this chapter, the calibration and analysis techniques routinely applied to data obtained with the University of Durham Mark 6 telescope have been described. A set of parameter selections has been defined which are expected to reject a large fraction of hadronic events while retaining the majority of any γ-rays. This has resulted in a 5σ detection of PSR 1706-44 from data obtained during the 1996 observing season.

These parameter selections have been applied to data obtained from southern hemisphere blazars to search for possible TeV γ-ray emission. The results obtained from this analysis will be presented in Chapter 6.

Chapter 5

γ-Ray Production in Blazars

5.1 Introduction

The term active galactic nuclei (AGN) is used to describe a wide variety of extra-galactic objects which exhibit very large luminosities of a non-stellar origin. Although large numbers of classifications exist, common features of AGNs include rapid flux variability, large collimated relativistic jets, strong emission lines and non-thermal continua. These features are indicative of a population of objects which contain large magnetic fields, efficient particle acceleration mechanisms, accretion discs and possibly massive black holes. Observations of AGNs reveal some of the most energetic processes taking place within the Universe.

At present, the general structure of AGNs is thought to be reasonably well understood and is schematically represented in Figure 5.1. The inherent axial-symmetry of these objects allows the observable properties to vary considerably depending upon the viewing angle. This has led to the unification schemes, in which the underlying physical processes are similar in all AGNs containing radio jets, but the different observable features are due to the angle at which these systems are viewed (reviewed by Antonucci, 1993). The unification scheme at present suggests that beamed emission is predominantly observed from AGNs which are viewed at

relatively small angles with respect to the jet axis. At large viewing angles the relativistic jets appear in the plane of the sky and the central accretion disc and black hole are believed to be obscured by a large molecular torus. The large radio fluxes observed from these objects have given rise to their being termed as 'radio-loud' galaxies. A large number of AGN systems do not show these large extended jets, such as Seyfert type I and II galaxies. These galaxies are characterised by strong broad emission lines and a bright central nucleus. The lack of large radio jets from these objects has led to their being termed 'radio-quiet' galaxies.

Prior to the CGRO (see Section 1.4.1), only one AGN was known to emit at γ-ray energies: the quasar 3C273, detected by the COS B satellite (Swanenburg *et al.*, 1978). This situation has recently changed dramatically with the advent of the EGRET experiment onboard the CGRO, which has detected nearly 50 AGNs in the energy range 30 MeV to 20 GeV. To complement these detections, two close AGNs have recently been detected at TeV energies. This chapter will outline recent γ-ray observations (Section 5.1.2), the attenuating affect of the intergalactic infrared background (Section 5.2), the blazar class of AGN (Section 5.3.1) and possible γ-ray production mechanisms (Section 5.4). By combining these considerations a list of objects observable from the Bohena site from which VHE γ-ray emission maybe expected is produced (Section 5.6).

5.1.1 EGRET Observations

With the launch of the CGRO, the γ-ray sky in the energy range 1MeV - 30 GeV opened up. One of the most dramatic discoveries made with this satellite was the number of AGNs detected with the EGRET experiment (see Section 1.4.1). Mattox *et al.* (1997b), have reported on the detection of 42 AGNs above a 5σ detection level and a further 16 with marginal detection significances ($4 < \sigma < 5$) obtained during observing phases I and II. All the AGNs detected by EGRET fall into the blazar category of radio-load AGN (see Section 5.3). The lack of any detections from radio-quiet systems (Seyfert quasars) and Fanaroff-Riley type I and II (see

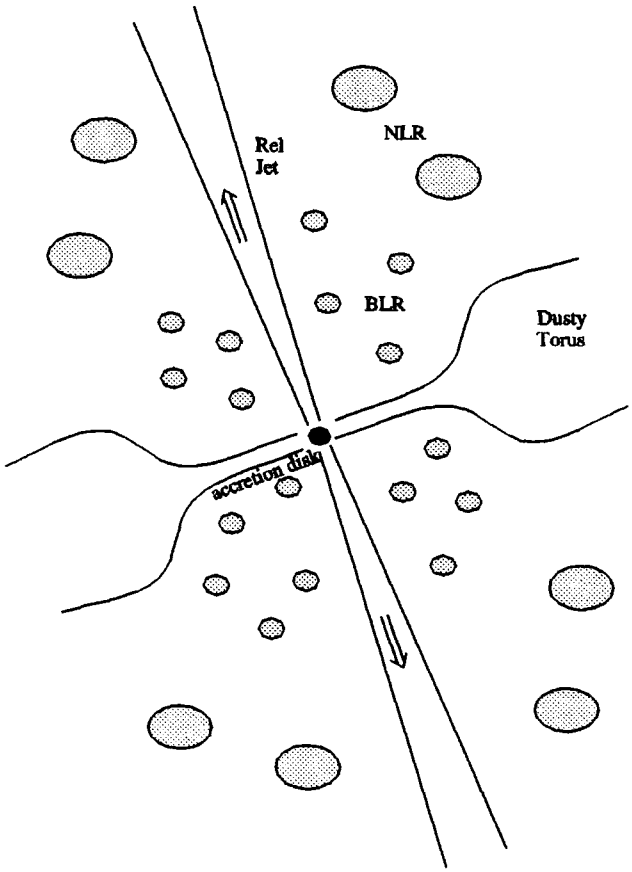

Figure 5.1: A schematic representation of a typical radio-loud AGN environment. The central black hole is fed by matter infalling from the surrounding accretion disc. Thermal radiation from the disc is reprocessed by local gas and dust clouds, resulting in optical emission lines becoming observable. The clouds closest to the central region produce broad line (BLR) emission, while at a greater distance narrow emission lines (NLR) are detected. Symmetric jets are seen emanating from the central black hole region. The synchrotron emission observed from these jets indicate the presence of a population of energetic electrons.

Table 5.1: EGRET detected BL Lacs ($z < 0.2$)

Object	Other name	z	EGRET Flux ($E > 100\,MeV$) ($10^{-7}\,cm^{-2}\,s^{-1}$)
1101+384	Mrk 421	0.031	1.5 ± 0.4
0521-365	PKS	0.055	2.1 ± 0.6
2200+420	BL Lac	0.069	2.1 ± 0.6
2005-489	PKS	0.071	1.8 ± 0.5
1219+285	W COM	0.102	0.8 ± 0.2
2155-304	PKS	0.117	2.7 ± 0.7
0829+046	OJ 049	0.180	1.9 ± 0.6

Section 5.3) radio-loud galaxies is consistent with the idea that MeV-GeV γ-rays are produced by relativistic processes within radio jets. These γ-rays become visible only when viewed along the jet axis, the orientation consistent with blazars.

The emission from most blazars observed by EGRET is well represented by a power law

$$\frac{dN}{dE} \propto E^{-\Gamma_\gamma} \tag{5.1}$$

with

$$\Gamma_\gamma = (1.4 \rightarrow 3.0) \pm 0.2.$$

Plotting νF_ν vs ν for these objects reveals that in a large number of cases the amount of power released as γ-rays can equal or even exceed that produced in the IR and optical wavebands.

Of the 90 BL Lacs (see Section 5.3.1) previously catalogued (Hewitt and Burbidge, 1993), 14 have been detected by EGRET through to observing phase IV (Yin *et al.*, 1997). Of these 14, 10 have previously been classified as radio selected BL Lacs (RBL), two as X-ray selected BL Lacs (XBL) (see Section 5.3.2) and the classifications of two are unknown. The sample of EGRET detected BL Lacs at $z < 0.2$ has been studied by Lin *et al.* (1996) and are summarised in Table 5.1.

5.1.2 Review of Previous TeV Detections

Cen A

Cen A was reported as a TeV γ-ray source in the early 1970's (Grindlay *et al.*, 1975). Observations were made over the period 1972-1974, using an adapted optical interferometer as a Čerenkov detector. The threshold of this detector was quoted at 300 GeV. The detection of a muon core allowed a simple hadronic rejection to be made. From the 50 hours of observations obtained, a 4.6σ detection was claimed. This corresponded to a rate of 0.76 ± 0.16 γ-rays min^{-1}. The integral flux was calculated as

$$F_\gamma(\geq 300\ \mathrm{GeV}) \simeq 4.4 \pm 1.0 \times 10^{-11} \mathrm{cm}^{-2}\mathrm{s}^{-1}.$$

An energy spectrum was produced by dividing the data according to the size of the signals from the individual events. Three size bins corresponding to threshold energies between 300 - 3000 GeV were used. It was suggested that the observations were consistent with Cen A having a flat source spectrum ($\Gamma = 1.7$) with a possible high energy break at around 10^{12} eV. The University of Durham Čerenkov telescopes have observed Cen A on a number of occasions (Carramiñana *et al.*, 1990) and an upper limit above 300 GeV has been determined

$$F_\gamma(\geq 300\,\mathrm{GeV}) < 7.8 \times 10^{-11}\ \mathrm{cm}^{-2}\mathrm{s}^{-1}.$$

Mrk 421

Mrk 421 is the closest EGRET detected blazar ($z = 0.031$) and has previously been classed as an X-ray selected BL Lac (see Section 5.3.2). TeV emission was first detected by the Whipple telescope, based upon 445 minutes of ON source observations obtained during the 1992 observing season (Punch *et al.*, 1992). The detection significance after the 'Supercuts' parameter selection is claimed as 6.7σ, with a rate of 0.34 ± 0.05 γ-rays min^{-1}. The integral flux above 500 GeV is

$$F_\gamma\ (\geq 500\ \mathrm{GeV}) \simeq 1.6 \times 10^{-11}\ \mathrm{cm}^{-2}\mathrm{s}^{-1}.$$

Schubnell *et al.* (1996), report on the observations made with the Whipple telescope during the 1992-1994 observing seasons (a total of 59 nights). From the analysis of the data during this period, it was concluded that the source appeared to be highly variable. Mrk 421 had previously been seen to be variable from radio through to X-rays, but no variability has been observed with EGRET (Lin *et al.*, 1992). A strong flare was reported on May 14^{th}-15^{th} 1994 (Kerrick *et al.*, 1995a), during which period the flux increased by a factor of ten above the quiescent level

$$F_{flare}\,(\geq 250\ \text{GeV}) \simeq 21.9 \pm 3.8 \times 10^{-11}\ \text{cm}^{-2}\text{s}^{-1}.$$

The flare of Mrk 421 occurred while this object was a subject of a multiwavelength observation campaign. This has provided vital information regarding possible production mechanisms. Mrk 421 was again seen to flare once in 1995 (Buckley *et al.*, 1996) and twice within a 7 day period in May 1996 (Gaidos *et al.*, 1996). The flares during May 1996 produced the largest TeV flux observed to date. During this period the spectrum was best fitted with a single power law extending up to 5 TeV, given by (McEnery *et al.* 1997)

$$F(E) = (2.24 \pm 0.12 \pm 0.7) \times 10^{-6}\ \ E^{-2.56\pm0.07\pm0.1}\ \ \text{photons s}^{-1}\text{m}^{-2}\text{TeV}^{-1}$$

Buckley *et al.* (1996), have concluded that the γ-ray emission from Mrk 421 is best characterized by a succession of rapid flares with a baseline level near the sensitivity limit of the current Whipple detector and consistent with little steady emission. The subject of blazar variability and flares will be discussed in Section 5.5.

The HEGRA collaboration observed Mrk 421 during Dec 1994→May 1995 using the first two HEGRA telescopes (CT1 and CT2), from which an independent confirmation of Mrk 421 as a TeV source was obtained (Petry *et al.*, 1996). The claimed threshold of this pair of telescopes is 1 TeV. CT1 collected 111 extra events in 28 hours of ON source data, producing a 4.0σ detection. CT2 collected 218 excess events in 41 hours of ON source data, resulting in a detection at the 4.1σ level. Combining these two detections results in a overall significance of 5.8σ, corresponding

to a rate of 5 γ-rays hour^{-1}. The integral spectrum above 1 TeV is given as

$$F_\gamma\,(\geq 1\text{ TeV}) \simeq 8(\pm 2)_{stat}(+6-3)_{syst} \times 10^{-12}\text{ cm}^{-2}\text{s}^{-1}.$$

Mrk 501

The second AGN detected by the Whipple collaboration at TeV energies was Mrk 501 (Quinn *et al.*, 1996). This object shares a number of similar features of Mrk 421. Mrk 501 has also been previously classed as an X-ray selected BL Lac and is located at a similar redshift (z = 0.033). One important difference between these two objects is that unlike Mrk 421, Mrk 501 has not been detected by the EGRET experiment.

The Whipple detection of Mrk 501 was based upon 40 hours of data obtained during the period March - July 1995. An excess of 334 γ-ray candidates were observed in 2275 minutes, corresponding to a rate of 0.15 ± 0.02 γ-rays min^{-1}. The significance of this detection after the Supercuts parameter selection is reported at 8.36σ. The flux of Mrk 501 during this period was approximately 20% that of Mrk 421 and is given as

$$F_\gamma\,(\geq 300\text{ GeV}) \simeq 8.1 \pm 1.4 \times 10^{-12}\text{ cm}^{-2}\text{s}^{-1}.$$

The Whipple data indicates an integral spectral index of -1.0. It should be noted that the lack of an EGRET detection indicates that the integral spectrum between 100 MeV and 300 GeV must be harder than -1.2. Variability was first observed during MJD 49,921, when the flux was seen to increase by a factor of 5 above the quiescent level.

This object was independently confirmed as a TeV source by the HEGRA collaboration (Bradbury *et al.*, 1997). This result was obtained from 147 hours of data using the CT1 telescope during March - August 1996. Off source calibration data were obtained in the months before, during and after the Mrk 501 observing season. An excess of 351 γ-ray candidates were observed, resulting in a 5.2σ detection at a

rate of 2.4 ± 0.5 γ-rays hour^{-1}. The differential spectral index has been calculated as 2.6 ± 0.5, with an integral flux above 1.5 TeV of

$$F_\gamma\,(\geq 1.5\,\mathrm{TeV}) \simeq 2.3(\pm 0.4)_{stat}(+1.5 - 0.6)_{syst} \times 10^{-12}\,\mathrm{cm}^{-2}\mathrm{s}^{-1}.$$

During 1997, Mrk 501 has shown a dramatic increase in flux over a period of a number of months, with short term flaring activity superimposed upon this increase. The Whipple collaboration have observed an average flux increase of more than a factor of 16 above the 1995 level (Quinn *et al.*, 1997). The HEGRA collaboration have observed Mrk 501 to have a flux varying between a factor of one and eight times the Crab. During this high state, Mrk 501 has also been detected with the CAT (Barrau *et al.*, 1997) and Telescope Array prototype (Aiso *et al.*, 1997) Čerenkov telescopes. Further details of this flux variability will be given in Section 5.5.

Upper Limits

The Whipple collaboration have reported upper limits (significance $\leq 3\sigma$) from 35 AGNs during the observing periods 1991 - 1994 (Kerrick *et al.*, 1995b), with 15 of these objects confirmed as EGRET detections. The data were mostly taken in the ON/OFF observing mode with the background hadronic events being rejected with the 'Supercuts' parameter selection. The absence of TeV signals may imply a change in the primary source spectrum above the EGRET threshold and/or the effect of absorption by pair production on extragalactic IR photons (see Sections 1.3 and 5.2). The non-detections have been grouped together to improve counting statistics but no excess is observed to be present. The observations of BL Lacs with $z < 0.2$ observed with Whipple telescope are reported in Catanese *et al.* (1997).

Recently, the X-ray selected BL Lac, 1ES2344+514 ($z = 0.044$), has been reported by the Whipple collaboration as a tentative TeV detection (Catanese *et al.*, 1997). Further observations of this sources are needed to confirm this result. This object has not been detected by EGRET.

The CANGAROO collaboration has reported upper limits above 2 TeV from four southern hemisphere BL Lacs - PKS 0521-365, PKS 2316-423, PKS 2005-489 and EXO 0423-084 (Roberts *et al.*, 1997b). No evidence was found for any steady DC emission or flaring activity.

5.2 Infrared Attenuation

Gould and Schréder (1966), suggested that TeV γ-rays from AGNs may be attenuated by pair production with the intergalactic IR background. The energy density of the IR background is very difficult to determine directly due to the Galactic and solar components, but attempts have been made with the Diffuse IR Background Experiment (DIRBE) on the Cosmic Microwave Background Explorer (COBE) (Hauser, 1991). The energy density of the IR background is of great cosmological significance as it is especially sensitive to the rate of early star formation. For γ-rays of energy E, the cross section for pair production is maximized when the soft photon energy (ε) is in the range:

$$\varepsilon(E) \simeq \frac{2(mc^2)^2}{E} \simeq 0.5(\frac{1 \text{ TeV}}{E}) \text{ eV}. \tag{5.2}$$

In a series of papers (Stecker *et al.*, 1992; Stecker *et al.*, 1993) it has been suggested that an indirect measurement may be made of the IR background by determining the spectral energy distributions of γ-ray emitting AGNs at various redshifts. Stecker *et al.* (1992), showed that for an object at a redshift of z, with IR photons of energy ε and number density $n(\varepsilon)d\tau\text{cm}^{-3}$, the corresponding optical depth is given by

$$\tau(E) = \frac{c}{H_0}\int_0^z dz(1+z)^{\frac{1}{2}}\int_0^2 \frac{x}{2}\int_{\varepsilon_1}^{\infty} d\varepsilon n(\varepsilon)\sigma[2x\varepsilon E(1+z)^2] \tag{5.3}$$

where σ is the pair creation cross section and

$$\varepsilon_1 = \frac{2m^2c^4}{Ex(1+z)^2} \quad \text{for} \quad z \ll 1.$$

De Jager *et al.* (1994), have calculated a value for the IR background using EGRET and Whipple observations of Mrk 421. De Jager *et al.*, point to a possible spectral break at 3 TeV in the Whipple data as a signature of extragalactic absorption. The determined value is consistent with the conversion of at least 30% of the energy from stellar nucleosynthesis to IR, both from emission by cool stars and as a result of absorption and re-emission by interstellar dust.
Biller *et al.* (1995), reject de Jager *et al.*'s findings on three points:

1. The spectral break (if real) may be due to an intrinsic change in the source spectrum due to acceleration limits or internal absorption. Analysis of data from one source can only produce an upper limit.
2. De Jager *et al.* assume a known uniform IR spectrum: this may not be a valid assumption.
3. The extrapolation of the spectral index from the EGRET data up to TeV energies is prone to large uncertainties due to poor EGRET statistics.

For a more precise estimate of the IR background, data are needed in the 100 GeV energy range in order to determine the true spectral shape between the EGRET and Whipple data. Biller *et al.* (1995), have produced a set of upper limits to the IR background (see Table 5.2 and Figure 5.2).

Stecker and de Jager (1997), have presented a new calculation of the intergalactic γ-ray pair production coefficients as a function of energy and redshift. Applying a model of the spectral energy distribution of Mrk 421 and recent measurements obtained by the HEGRA group (Petry *et al.*, 1996) from this object, an observed spectral steepening in the energy range $3 \rightarrow 5$ TeV is again interpreted as γ-ray absorption due to pair production with the IR background. Figure 5.3 shows the optical depth due to intergalactic pair production derived from this new calculation as a function of energy at a number of redshifts.

Table 5.2: Upper limits on the Infrared Background energy density (After Biller *et al.*, 1995)

E_{TeV}	ε (eV)	Energy density eV cm^{-3}
0.5	1.0	0.11
1.0	0.5	0.06
5.0	0.1	0.04

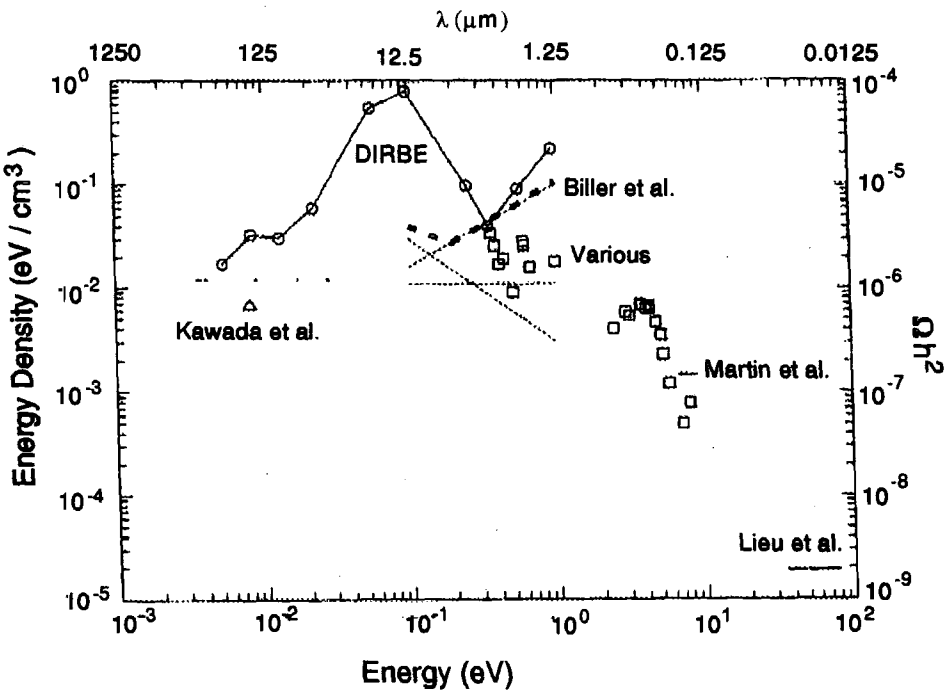

Figure 5.2: Experimental upper limits on the background IR energy (see Biller *et al.* (1995) and references therein). The energy density is expressed in both units of eV cm^{-3} and in terms of the critical density Ω, times h^2, where the Hubble constant is given by 100 h km s^{-1}Mpc^{-1}. Dotted lines show limits derived by Biller *et al.* for assumed IR spectral indices of 1.2 (positive slope), 2 (flat) and 3 (negative slope). From Biller *et al.* (1995).

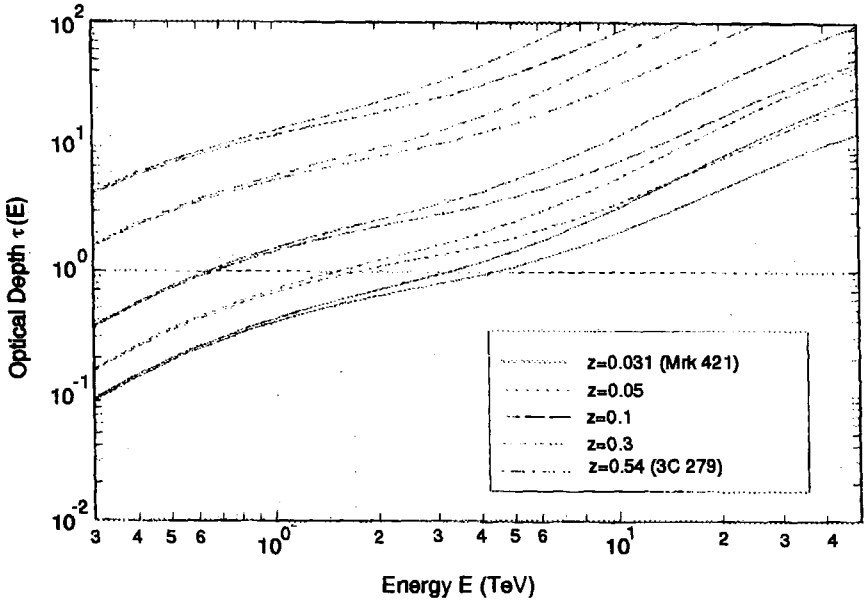

Figure 5.3: The optical depth as a function of γ-ray energy at a number of redshifts. The two predictions at each value of z corresponds to two models of the spectral energy distributions of Mrk 421. From Stecker and de Jager (1996).

Stanev and Franceschini (1997), have produced strong upper limits on the IR background based on the recent HEGRA observations of Mrk 501 (Aharonian *et al.*, 1997). These observations have shown a spectrum which extends to beyond 12 TeV, with no evidence for a spectral steepening due to pair production with the IR background. The upper limits determined by Stanev and Franceschini are inconsistent with the energy density determined by Stecker and de Jager (1997) and is close to the lower limits produced by recent deep IR surveys. Analysis of the data obtained by a number of independent telescopes of Mrk 501 during its very active period in 1997 should provide information to help resolve these inconsistencies.

5.3 Blazar Characteristics

The 50 extragalactic objects detected with the EGRET experiment have all been associated with blazars (Mattox *et al.*, 1997b). The blazar category of radio loud AGN is thought to encompass objects in which beamed emission from relativistic

jets plays a critical role. In blazars, the large radio jets seen in images of radio-loud galaxies are believed to be orientated such that the jet axis is close to the line of sight of the observer. The emission from these jets results in a nonthermal continuum being observed which swamps the emission from the rest of the host galaxy.

Evidence for this beamed emission has come from observations of superluminal motion, short term variability and very high calculated bolometric luminosities. A key characteristic of all blazars is the nonthermal emission extending from the radio through to UV and in some cases X-rays. This emission is believed to be produced by synchrotron radiation, emitted by a population of relativistic electrons contained within the jet (for a basic review of these properties see Robson, 1996).

The blazar population is subdivided into two different observed types of objects: BL Lacs and optically violently variable quasars (OVV quasars), otherwise known as flat spectrum radio quasars (FSRQs). These two types of objects share the common features of all blazars, showing a broadband nonthermal continuum, rapid high amplitude variability, a high degree of polarization and superluminal motion. Approximately 200 blazars have been catalogued (for a recent and highly detailed review of radio loud galaxies see Urry and Padovani, 1995).

5.3.1 BL Lacs and OVV Quasars

The basic properties of these two types of objects are summarised below:

• **BL Lacs** : Mainly observed below $z < 0.2$, appear to have relatively low bolometric luminosities (compared to OVV quasars), very weak or non-existent emission lines (equivalent widths $W_\lambda < 0.5\,\AA$) and superluminal motion (of the 11 BL Lac objects consistently observed by the VLBI, all have shown superluminal motion).

• **OVV quasars** : Found in the redshift range $0.1 < z < 2$, large bolometric luminosities, strongly polarized continuum spectra, highly erratic variability and very strong and broad optical emission lines.

A key distinction between the OVV quasars and BL Lacs has come from X-ray

observations. The OVV quasars on the whole show X-ray emission that has a significantly flatter spectrum than that of BL Lacs. While BL Lacs show a continuous spectrum through the radio to X-rays, the X-ray emission from OVV quasars is seen to lie above that extrapolated from the IR and optical emission. This is clearly indicative that in OVV quasars there are distinct emission processes involved in these two regions.

Although OVV quasars and BL Lacs show overall similar features, a number of differences still remain to be resolved. One possible explanation is that these two classes of objects are a result of two distinct parent radio galaxy populations. To determine the parent population, the luminosity function of these objects needs to be calculated (the number of sources per unit volume per unit luminosity as a function of redshift). This requires complete deep sky surveys.

Padovani and Urry (1990), calculated the luminosity function for Fanaroff-Riley type I (FR I) radio galaxies (FR I radio galaxies exhibit low luminosity extended lobe emission connected to a central region by turbulent jets, as opposed to FR II which have powerful radio lobes connected by smooth supersonic jets). From a known parent luminosity function it is possible to estimate the beaming parameters for the BL Lac sample, which can be tested against observations [A full outline of this work is given by Urry *et al.* (1991)]. The luminosity function of FR I galaxies suggests that BL Lacs should have beaming factors in the range $2 < \delta < 16$ with the average tending to smaller values. This was found to agree with VLBI observations of BL Lacs.

VLBI observations of BL Lacs also indicate that the magnetic fields within the jets run perpendicular to the jet axes. This is consistent with strong shocks being present within the jet, compressing and enhancing the transverse magnetic field. Conversely the observations of OVV quasars show the magnetic fields running parallel to the jet axis, suggesting the absence of shocks.

Further evidence for the connection between BL Lacs and a parent population of FR I radio galaxies was provided by Antonucci and Ulvestad (1985), who obtained

very deep radio map of blazars. This study used the principle that the relatively weak lobe emission seen in FR I galaxies and the far stronger lobe emission from FR II should be unaffected by orientation. The very deep radio maps of the BL Lac sample did indeed show very weak extended emission surrounding the dominant core, while the OVV quasars exhibited much stronger lobe emission. Barthel (1989), showed that the flat spectrum radio-loud quasar population (OVV quasars) was consistent with the FR II radio galaxies beamed towards the observer. This conclusion suggests that radio galaxies with the jets aligned $\theta < 40 - 50°$ to an observer will be seen as quasars.

5.3.2 X-Ray and Radio Selected BL Lacs

BL Lacs were first found in high frequency radio surveys (for a recent extensive survey see Stickel *et al.*, 1991). With the advent of high sensitivity X-ray experiments, a new population of BL Lac objects were discovered whose X-ray emission was the dominant spectral component. This has given rise to the terms radio and X-ray selected BL Lacs (RBLs and XBLs respectively). The XBL sample is characterised by a flatter spectral energy distribution from radio through to X-rays, a lower degree of polarization and a higher fraction of starlight.

Sambruna *et al.* (1996), have carried out an extensive analysis of the spectral energy distributions (SEDs) from a complete sample of blazars, RBLs (1 Jy radio sample, Stickel *et al.*, 1991), XBLs (Einstein Extended Medium Sensitivity Survey, EMSS, Morris *et al.*, 1991) and a small but complete sample of FSRQs (S5 radio survey, Brunner *et al.*, 1994). This study compared the data obtained from the ROSAT X-ray satellite with radio, IR, optical and UV fluxes from the literature via the NASA Extragalactic Database (NED).

Although the terms RBL and XBL have been used extensively, it was suggested by Padovani and Giommi (1996), that these terms were inadequate, with some BL Lac objects included in both the radio and X-ray surveys. It was suggested that these objects should be categorised either as low frequency peaked BL Lacs (LBLs),

or high frequency peaked BL Lacs (HBLs) depending upon the ratio of the X-ray to radio flux

$$F_{\frac{X}{R}} = \frac{F(0.3 - 3.5\,\mathrm{keV})}{F(5\,GHz)} \tag{5.4}$$

where

$$F_{\frac{X}{R}} < 10^{-11.5} \rightarrow LBL$$

$$F_{\frac{X}{R}} > 10^{-11.5} \rightarrow HBL$$

Sambruna *et al.* (1996), characterise the SEDs by two methods

1. Using broadband spectral indices
2. Fitting the SEDs with a parabola

Method 1 uses the definitions of broadband indices provided by Ledden and O'Dell (1985)

$$\alpha_{12} = -\frac{\log(\frac{F_1}{F_2})}{\log(\frac{\nu_1}{\nu_2})}$$

$$\alpha_{121} = \alpha_{21} - \alpha_1$$

where F_n is the flux density at frequency n.

A value of $\alpha_{xox} \approx 0$ would indicate that the X-ray spectrum lies on the extrapolation of the optical to X-ray slope. Negative and positive values indicate a convex or concave continuum respectively. A concavity would suggest the presence of a hard spectral component in the X-ray band which may connect to the γ-ray emission. Although of a similar form, the spectral indices indicate that different classes of blazars have systematic differences in their continuum shapes. XBLs differ strongly from RBLs and FSRQs in having a flatter overall radio to optical spectra and convex

optical to X-ray continua. RBLs and FSRQs have similar radio and optical energy distributions but differ significantly in the shape of the optical to X-ray continua (see Figure 5.4 and Figure 5.5).

The parabolic fit allowed the use of the complete spectrum of measurements, making the determination of the bolometric luminosity and the peak frequency (ν_p) easier. The fit was given by

$$\log(\nu L_\nu) = A(\log \nu)^2 + B \log \nu + C. \tag{5.5}$$

All three types of object seem to follow a systematic pattern, with the power per decade peaking (ν_p) in the range $10^{13 \rightarrow 17.5}$ Hz. When this peak is $< 10^{14}$ Hz, as for LBLs and FSRQs, the optical to X-ray continuum appears concave, with a flat X-ray spectrum. This would suggest that the X-ray emission is of a different origin than the optical emission. The LBLs and FSRQs also appear to have large luminosities. In contrast, HBLs have convex optical to X-ray continua and steep X-ray spectra consistent with a high frequency extension of the synchrotron emission.

Sambruna *et al.* (1996) conclude that orientation effects alone are unlikely to be able to produce the different SEDs, especially the factor of 10^4 variation in ν_p. The different SEDs seem to require a smooth change of the intrinsic physical parameters. Specifically, the transition $XBL \rightarrow RBL \rightarrow FSRQ$ corresponds to a decreasing magnetic field and/or decreasing electron density. The overall topologies of the three classes of blazars appear similar, with the observed spectral differences being due, in part, to variations in physical parameters. The contribution played by the accretion disc may become important for the FSRQs, as emission lines are clearly visible. To make further progress it is critical to obtain simultaneous measurements from radio to γ-rays, especially with accurate determination of the position of the synchrotron and γ-ray peaks. These peaks are indicators of the magnetic field and electron densities present within the system.

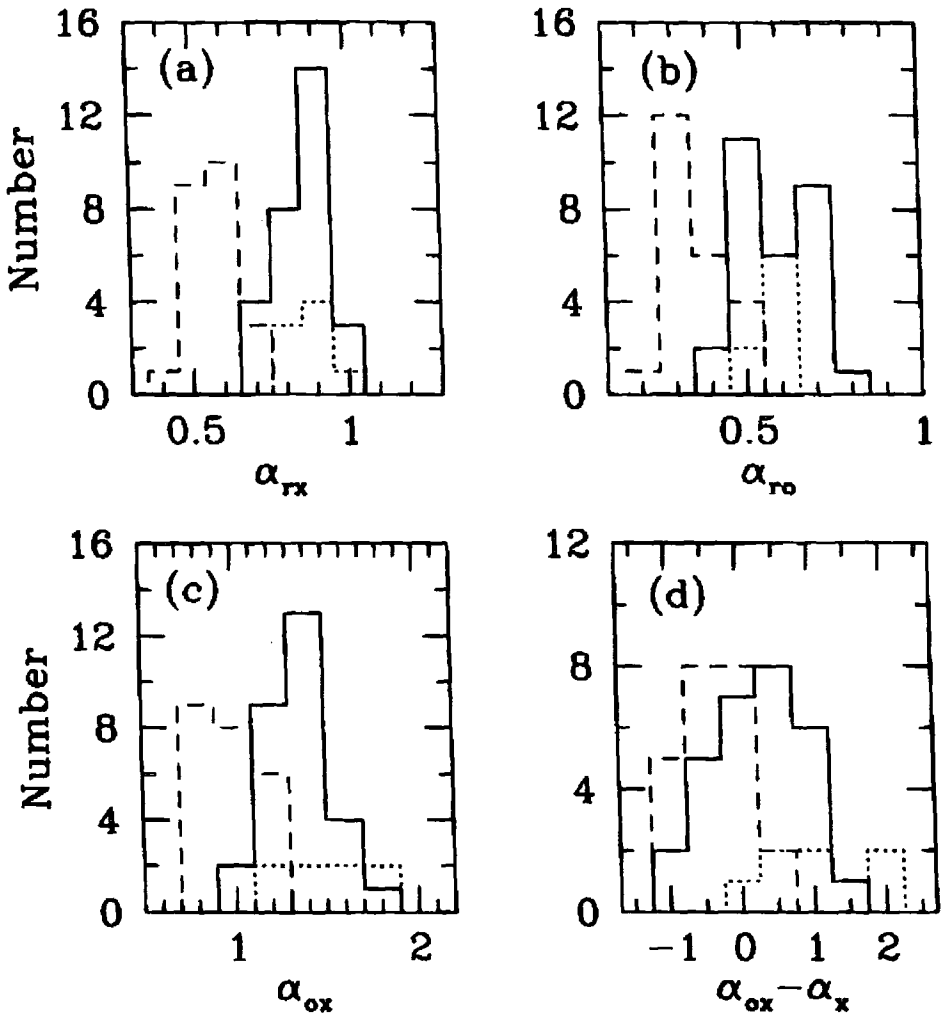

Figure 5.4: Distributions of the composite spectral indices for the EMSS XBLs (*dashed line*), the 1 Jy RBLs (*solid line*) and the S5 FSRQs (*dotted line*). (a): radio-to-X-ray index, α_{rx}, (b):radio-to-optical, α_{ro}, (c):optical-to-X-ray index, α_{ox}. In all three cases, XBLs are well separated from both RBLs and FSRQs, at a 99.9% confidence level and they have flatter indices. RBLs and FSRQs do not differ significantly from one another. (d): distribution of α_{xox}, where α_x is the ROSAT energy spectral index. XBLs have mostly negative indices, indicating typically convex spectra, at variance with FSRQs, which have concave continua. RBLs have a large spread of optical-to-X-ray shapes. From Sambruna *et al.* (1996).

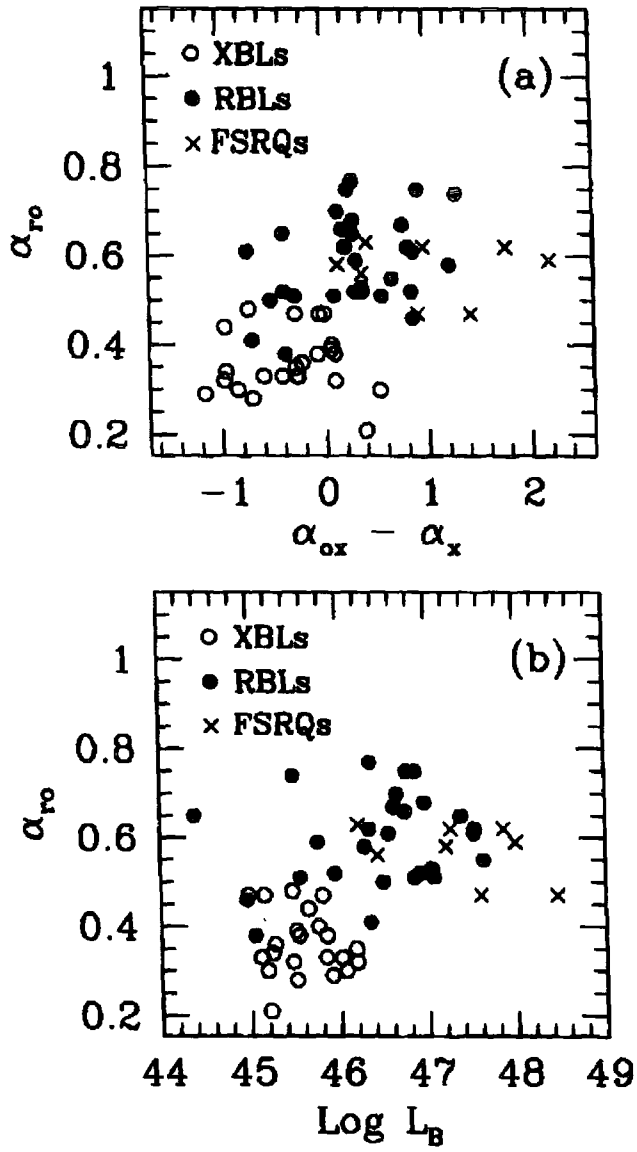

Figure 5.5: (a) Colour-shape plot of blazar spectra, with the radio-to-optical index, α_{ro}, vs. the concavity/convexity indicator, α_{xox}. The three blazar classes occupy different but overlapping regions, indicating a continuity of properties. (b) Plot of the radio-to-optical index, α_{ro}, vs. the bolometric luminosity, as estimated from parabolic fits to the multiwavelength spectra. There is a correlation at $> 99\%$ confidence, in the sense of more luminous objects having steeper α_{ro} indices or, as α_{ro} is strictly correlated with the peak frequency of the emission, ν_p. From Sambruna *et al.* (1996).

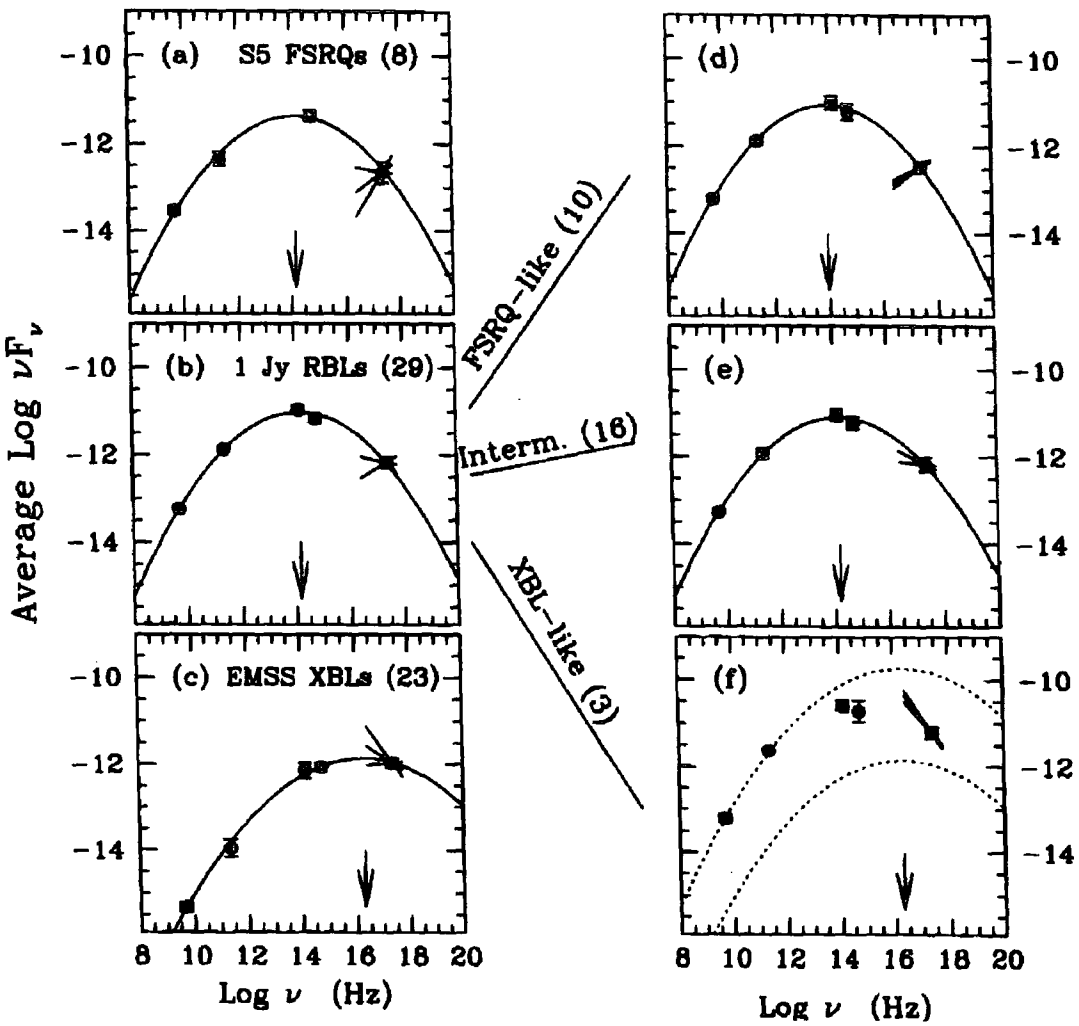

Figure 5.6: Average spectral energy distribution for (a) the complete sample of S5 FSRQs; (b) the complete sample of 1 Jy RBLs; (c) the complete sample of EMSS XBLs. The radio, millimetre, IR and optical points are averages of the mean K-corrected flux densities. Going from FSRQs to RBLs to XBLs, the peak of the emission shifts towards higher energies and the mean X-ray spectrum steepens. The RBLs can further be divided into three subgroups, according to the shape of their optical-to-X-ray continua. From Sambruna *et al.* (1996)

5.4 Production Mechanisms

Possible mechanisms for γ-ray production within blazars is an active area of current research. A brief review of three possible mechanisms will be presented and one current model which provides reasonable fits to the multiwavelength data available will be outlined in further detail. It should be noted that although blazars appear to have similar broadband features, there are a number of notable differences. The most obvious of these is the lack of emission lines observed from BL Lacs. This might have important implications concerning the local black hole and accretion disc environments. A recent review of production mechanisms has been provided by Sikora (1994a).

5.4.1 Synchrotron Self Compton

It has been firmly established that synchrotron radiation, originating from a population of relativistic electrons within the jets, is the dominant emission process from radio to optical frequencies in all blazars. In the synchrotron self-Compton model (SSC), the synchrotron photons act as a soft photon field. This photon field can undergo inverse Compton scattering with the population of relativistic electrons, producing X-rays and γ-rays (this model is described by Marscher and Bloom, 1993 and Maraschi *et al.*, 1992), see Figure 5.7a. This elegant model has the advantage that the relativistic electrons and the soft photons needed to produce γ-rays are a direct consequence of one another. Maraschi *et al.* (1992), applied this model and assumed an inhomogeneous jet to explain the spectrum of 3C279.

The maximum energy of the γ-rays produced by this mechanism is a function of the magnetic field density, electron energy density and the size of the production region. Sikora (1994a), suggested that the synchrotron and corresponding TeV photons may be produced within separate regions of the jet in order to avoid depression of the spectrum (which is not observed in the Whipple observations of Mrk 421) by the Klein-Nishina effect (the relativistic correction to Thompson scattering). Dar

(1992), suggested that SSC is such an efficient cooling mechanism that producing a steady TeV flux may be difficult.

5.4.2 External Compton

Dermer *et al.* (1992), proposed that soft photon fields originating external to the jet would enable inverse Compton scattering (EC) to produce GeV and TeV γ-rays. Based on observations of 3C273 and 3C279, Dermer *et al.* suggested that these soft photons could originate from an accretion disc (see Figure 5.7b). The soft photons from an accretion disc will be typically be in the UV or X-ray range due to the high temperatures.

This model predicts an absence of sources with spectra extending above 100 GeV, due to the γ-ray absorption with UV photons. The detection of both Mrk 421 and Mrk 501 above 300 GeV is an obviously problem for this model. For TeV emission to be present, the soft photon fields would have to be in the IR range and not in the UV. A further problem is that the soft photons from an accretion disc will enter the jet in the same direction as the bulk motion within this system. As a result, the soft photon field will appear to be redshifted within the jet frame, strongly limiting the maximum scattered photon energy. This effect could be limited if the external photons originated from the edges of the accretion disc. The redshifting of this photon field within the jet frame will then be limited by the large incident angle of these external photons.

A more efficient production mechanism was suggested, in which the external photons originate from dust and gas clouds surround the jet (Blandford, 1993; Sikora *et al.*, 1994b). Within this model, thermal UV and X-ray photons from the accretion disc would be reprocessed within emission line clouds, resulting in IR photons entering the jet at large angles (see Figure 5.7c). This model naturally resolves the problems associated with producing GeV and TeV γ-rays in the Dermer *et al.* (1992) model. Sikora *et al.* (1994b), used this mechanism to account for the spectrum of 3C279. This model has problems in explaining γ-ray emission from BL Lacs, which

show little evidence for these emission line clouds.

5.4.3 Hadronic Production

Mannheim and Biermann (1992), proposed that a flare observed during June 1991 from 3C279 could be explained by a hadronic production mechanism. In this model, very high energy protons interact with the photon fields within a jet, normally the synchrotron photons (the low density of matter in such regions rules out proton-matter interactions), to produce secondary particles

$$p + \gamma \rightarrow \pi^0 + p \quad \text{and} \quad p + \gamma \rightarrow e^+ + e^- + p.$$

The decay of these secondary particles provides the flux of γ-rays.

Recently, the hadronic models have been revisited, for example by Dar and Laor (1997), who have made predictions about TeV γ-ray emission from AGNs. These models predict that a number of a blazars should emit 50$\rightarrow$100 TeV γ-rays and that γ-ray flares will be accompanied by a flux of TeV neutrinos and delayed MeV and GeV γ-rays. As seen in Section 5.2, γ-rays with an energy greater than a few TeV will become strongly attenuated by the infrared photon background, but the neutrinos produced within these hadronic interactions will not be affected. Dar and Laor, propose that if the flare of PKS 1622-269 (z = 0.815), observed by EGRET in June 1995 (Mattox *et al.*, 1997a), had an accompanying TeV γ-ray component, approximately 30 ν_μ could have been detected by a 1 km^2 detector on the Earth's surface. A major problem for this model is that the EGRET experiment did not detect an increase in the MeV-GeV γ-ray flux during the flaring episodes of Mrk 421 (this is discussed further in Section 5.5.1). Mannheim *et al.* (1996), have produced predicted fluxes for 15 blazars (which are observable by the HEGRA particle array) using a hadronic model. It is concluded that a number of sources, including EGRET detected RBLs, should be detectable at 50 TeV by the HEGRA array with its current sensitivity.

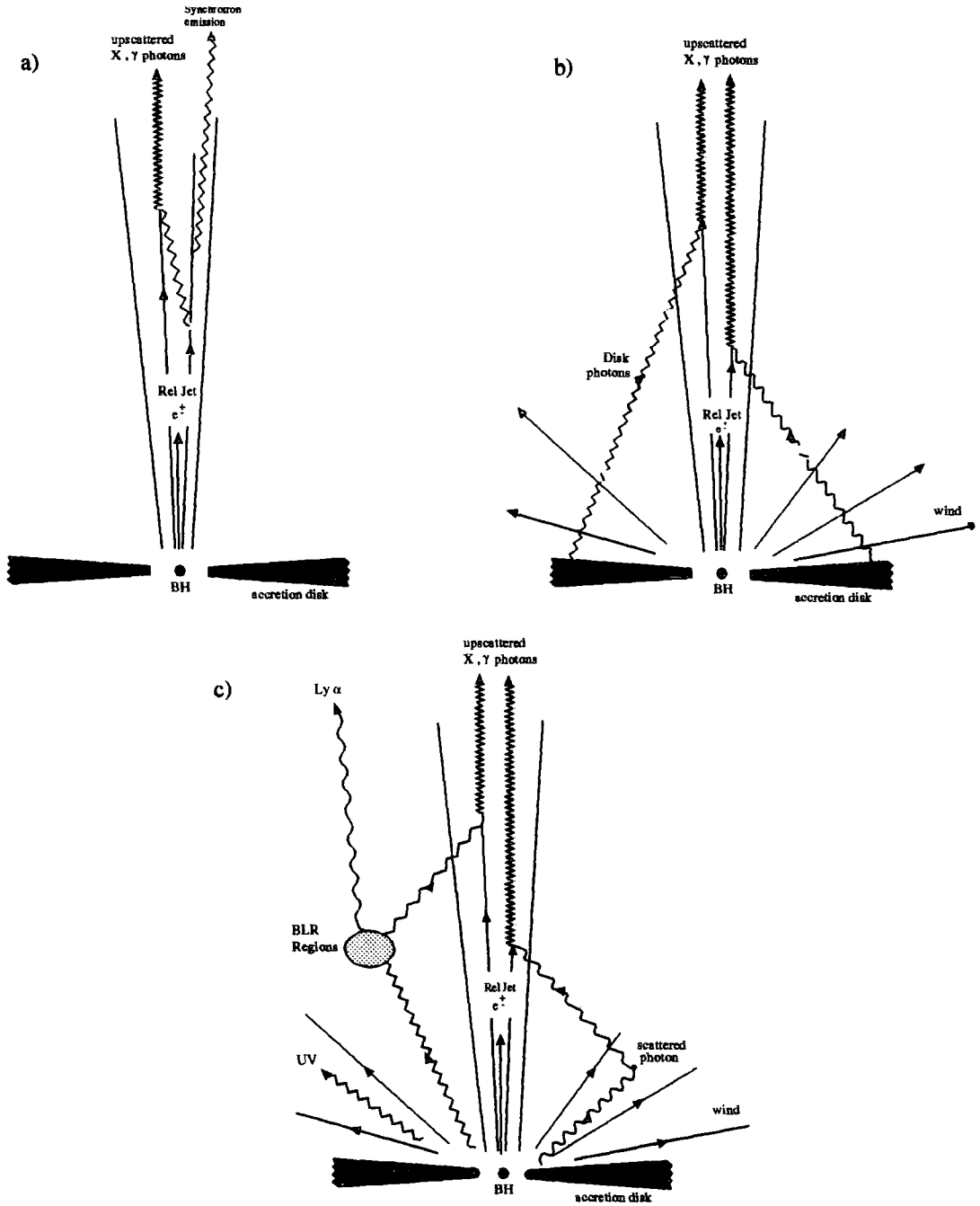

Figure 5.7: Schematic representations of possible γ-ray production mechanisms; a) Synchrotron Self Compton (Marscher and Bloom, 1993; Maraschi *el al.*, 1992); b) External Compton with the soft photon field provided by the accretion disc (Dermer *et al.*, 1992); c) External Compton with the soft photon field provided by emission line clouds (Blandford, 1993 ; Sikora *et al.*, 1994b).

Table 5.3: Physical Quantities

Parameter (Symbol)	Value
Electron injection index (s)	
Beaming factor (δ)	
Source radius (R)	pc
Magnetic field (B)	G
Ratio of electron energy density to magnetic energy density (η)	
Fraction of nuclear luminosity entering jet quasi-isotropically (γL_{nuc})	ergs s^{-1}
Mean energy (or temperature) of external photons (E_{ext} or T_{ext})	eV
Electron plasma scattering mean free path normalized by Larmor radius (ξ)	
Lorentz factor (Γ)	
Angle to line of sight (θ)	$^{\circ}$

5.4.4 Example Model

A review of a model for electron acceleration and γ-ray production within blazars produced by Inoue and Takahara (1996), (here-after known as IT96) will be discussed. This is designed to be a simple model with far fewer degrees of freedom than other models within the literature. Table 5.3 defines the physical parameters used. The basic model assumptions are :

1. One zone model : assumes a uniform one dimensional region which contains a single population of electrons; distances within this region are characterised by the parameter R.
2. Electron distribution approximated by a broken power-law.
3. Two basic types of soft photons, internally produced synchrotron and external thermal photons.
4. All particles and photon distributions are isotropic in the source frame

The beaming factor is given by

$$\delta = [\Gamma(1 - \beta \cos\theta]^{-1}, \tag{5.6}$$

where

$$\beta = \frac{v_s}{c}.$$

Synchrotron emission

The electron density will be normalised by giving B, along with the form of the electron distribution, $N(\gamma)$, so that

$$\eta = m_e c^2 \int_{\gamma_{min}}^{\gamma_{max}} \frac{\gamma N(\gamma) d\gamma}{\frac{B^2}{8\pi}}. \tag{5.7}$$

The standard homogeneous slab solution to the radiative transfer equation for the synchrotron emission is given by

$$I_\nu = \frac{j_\nu}{\alpha_\nu}(1 - e^{-\alpha_\nu R}), \tag{5.8}$$

where j_ν and α_ν are the emission and absorption coefficients respectively,

$$j_\nu = c_2 \, B \int_{\gamma_{min}}^{\gamma_{max}} d\gamma \, N(\gamma) F(\frac{\nu}{c_1 B \gamma^2}), \tag{5.9}$$

$$\alpha_\nu = -c_3 \, B \frac{1}{\nu^2} \int_{\gamma_{min}}^{\gamma_{max}} d\gamma \gamma^2 \frac{\partial}{\partial \gamma} [\frac{N(\gamma)}{\gamma^2}] \, F(\frac{\nu}{c_1 B \gamma^2}). \tag{5.10}$$

The constant terms are given in IT96.

Inverse-Compton emission

The calculation for the IC spectrum employs the formula derived by Jones (1968), which is accurate in both the Thompson and Klein-Nishina scattering regimes. The

electron energy is given by $\gamma m_e c^2$, the soft photon energy $\epsilon_0 m_e c^2$ and for the scattered high energy photon $\epsilon m_e c^2$. The differential photon production rate (number of photons of ϵ produced per energy interval per unit volume per unit time) will be a convolution over the electron and soft photon distributions

$$q(\epsilon) = \int d\epsilon_0 n(\epsilon_0) \int d\gamma N(\gamma) C(\epsilon, \gamma, \epsilon_0), \tag{5.11}$$

where $n(\epsilon_0)$ is the number density of the soft photon per energy interval and $C(\epsilon, \gamma, \epsilon_0)$ is the Compton kernel. This production rate (Equation 5.11) is converted to emission coefficient by the relations

$$j_\nu = \frac{h}{4\pi} \epsilon q(\epsilon), \quad \nu = \frac{m_e c^2}{h} \epsilon, \tag{5.12}$$

where h is the Planck constant.

Soft Photons

In the case of SSC, the soft photon intensity is simply the derived synchrotron spectrum. For the case of the external photons this becomes more difficult, due to the many possible sources. IT96 simply assume a diluted blackbody spectrum at a single temperature. In the source frame the mean soft photon energy is duly blueshifted

$$E' \sim \Gamma E_{ext} \sim \Gamma k_B T_{ext}. \tag{5.13}$$

Within the jet frame, the intensity of this radiation is given by

$$I_\nu = \tau \frac{L_{nuc}}{4\pi R^2} f_\nu(T_{ext}), \tag{5.14}$$

where $f_\nu(T_{ext})$ is a normalised Planck function and τ is the fraction of the nuclear

luminosity (L_{nuc}) at a distance R that is scattered/reprocessed isotropically (as in Sikora *et al.*, 1994b) or enters the jet at large angles (as in Dermer *et al*, 1992).

With angle averaging assumptions, the soft photon intensity within the source frame can be expressed as

$$I_{\nu'} = \Gamma\tau \frac{L_{nuc}}{4\pi R^2} f_{\nu=(\frac{\nu'}{\Gamma})}(T_{ext}). \tag{5.15}$$

Pair Absorption

The radius of the γ-ray source (R) is assumed to be of a size such that absorption by pair production of GeV γ-rays with coproduced X-rays is not important:

$$I_\nu = \frac{j_\nu R}{\tau_{\gamma\gamma}}(1 - e^{-\tau_{\gamma\gamma}}), \tag{5.16}$$

where $\tau_{\gamma\gamma}$ is the pair absorption optical depth. Equation 5.16 is analogous to equation 5.8.

Break Energy

An assumed kinetic energy equation for the electrons is determined. This equation assumes a power law injection spectrum and accounts for energy independent losses as well as radiative losses.

$$\frac{\partial N(\gamma)}{\partial t} = \frac{\partial}{\partial \gamma}[\frac{\gamma}{\tau_{cool}(\gamma)} N(\gamma)] + Q(\gamma) - \frac{N(\gamma)}{\tau_{ad}}. \tag{5.17}$$

$\tau_{cool}(\gamma)$ is the electron radiative cooling time, τ_{ad} is the advection or adiabatic loss time and $Q(\gamma) \propto \gamma^{-s}$ is the electron injection rate. From this the following steady state equation can be derived:

$$N(\gamma) = \exp(-\frac{\gamma_b}{\gamma})\frac{\gamma_b \tau_{ad}}{\gamma^2}\int_{\gamma}^{\infty} d\gamma' Q(\gamma') \exp(\frac{\gamma_b}{\gamma'}). \tag{5.18}$$

γ_b represents the electron break Lorentz factor, corresponding to $\tau_{cool}(\gamma) = \tau_{ad}$,

$$\gamma_b = \frac{3mc^2}{4(u_B + u_{soft})\sigma_T R}. \tag{5.19}$$

IT96 simplify the equation 5.18, which makes the broken power-law behaviour more apparent

$$N(\gamma) = K\gamma^{-s}(1 + \frac{\gamma}{\gamma_b})^{-1} \tag{5.20}$$

where K is a normalization constant, specified through B and η in equation 5.7.

Maximum Energy

It is assumed throughout the model that electrons gain energy via Fermi shock acceleration with magnetic disturbances. The physics of such processes within relativistic jets is currently poorly understood. By a simple treatment, IT96 equate the radiative cooling time $\gamma_{cool}(\gamma)$ with the acceleration time $\tau_{accel}(\gamma)$ to yield a maximum electron Lorentz factor

$$\gamma_{max} = \frac{\nu_s}{c}[\frac{9eB}{80(u_B + u_{soft})\sigma\xi}]^{\frac{1}{2}} \tag{5.21}$$

where ξ is the mean free path of the electrons between episodes of shock acceleration as a function of the Larmor radius.

Model Comparison with Observations

In order to limit the number of degrees of freedom within this model, IT96 constrained certain parameters using information obtained from observations. From superluminal motion studies, the conical value of $\delta = 10$ has be used; from pair production and variability studies the emission region is assumed to be $R = 0.03$ pc and the electron injection spectrum is taken to be $s = 2$.

Applying this model to the γ-ray blazar, 3C279, IT96 found the best fit was obtained with a combination of external and synchrotron self-Compton emission mechanisms (see Figure 5.8). This may not be surprising as observations of emission lines from this object reveal that there is an intense optical and UV thermal continuum. At the highest energies, pair production with the external photons is taking effect, resulting in a sharp cutoff near the observed maximum γ-ray energy (≈ 5 GeV).

The best fit obtained for the HBL, Mrk 421, is provided with a simple SSC model (see Figure 5.9). In order to produce TeV γ-rays, it is required that the local IR photon density field is low, in order to reduce the effect of pair production near the source. The TeV data points lie at the edge of a sharp spectral cutoff, corresponding to the electron acceleration limit, due to the Klein-Nishina effect (a maximum cutoff is expected at 5 TeV). The Whipple observations indicate that the spectrum extends beyond 5 TeV and has a spectral index which is not quite as steep as that predicted by the model. These inconsistencies may be overcome with the use of a more realistic multizone model. One important interpretation of this model is that TeV emission may be a unique property of Mrk 421 type objects (low luminosity and low external photon densities), which allows electron acceleration to very high energies with little radiative losses.

As this model clearly indicates, emission mechanisms within different classes of blazars may vary. A dominant factor within these mechanisms is the energy density of the external photons. To resolve the true emission mechanisms within the various types of blazars, contemporaneous multiwavelength monitoring of target objects are

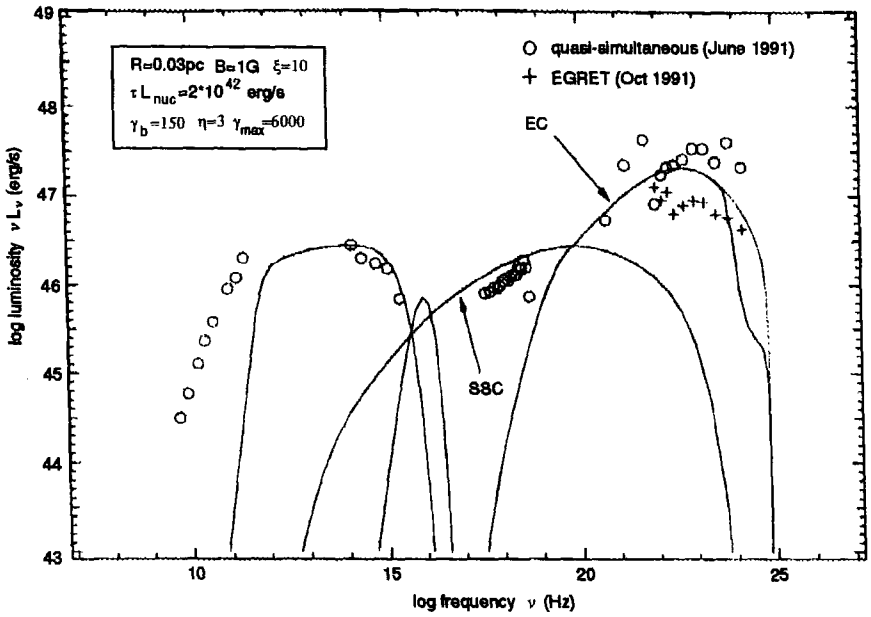

Figure 5.8: The spectral energy distribution of 3C279. The best fit provided by IT96 is shown (EC + SSC). Dotted lines are results without pair absorption. Best-fit parameters are shown within the figure. From Inoue and Takahara (1996).

needed.

5.5 Blazar Variability

One striking feature of blazars is their variability. By studying this variability over the whole electromagnetic spectrum it is possible to constrain both the physical parameters and production mechanisms within these objects. This powerful observational technique has only recently been fully utilised with the undertaking of large scale contemporaneous multiwavelength campaigns.

3C279

Gamma-ray variability was first detected from the blazar 3C279 ($z = 0.538$) during June 1991 with the CGRO (Kniffen *et al.*, 1993). This object showed a flux increase of a factor of five, with time scales for variations between days and weeks. Hartman

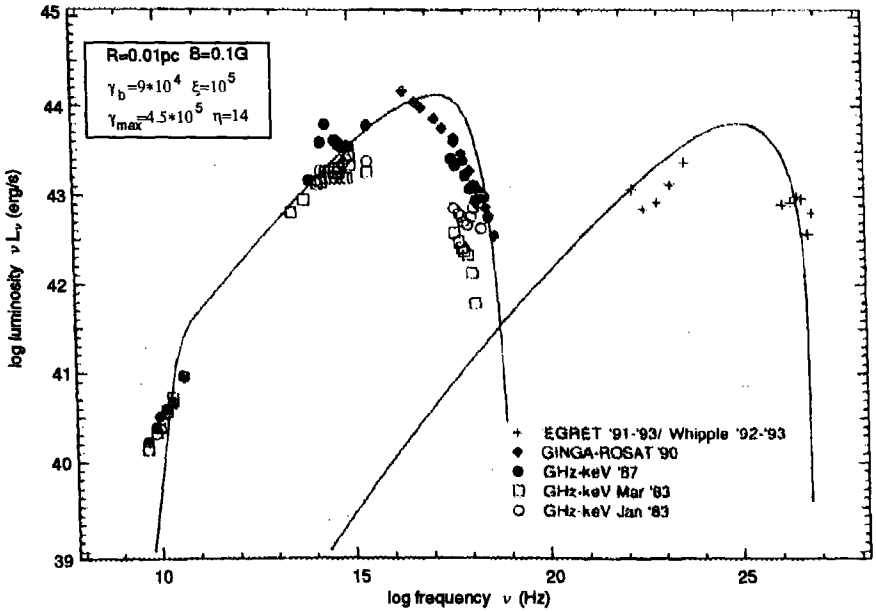

Figure 5.9: The spectral energy distribution of Mrk 421. The best fit provided by IT96 is shown (SSC only). Best fit parameter values are shown within the figure. From Inoue and Takahara (1996).

et al. (1996), brought together the multiwavelength observations made over the period early 1991 to mid 1992. It was concluded that the flare could be explained with either an SSC or EC model. The high amplitude γ-ray variation during this flare (see Figure 5.10) is predicted by the SSC model but could be reconciled with the EC model if a temporary change in the bulk Lorentz factor of the γ-ray emitting plasma occurred. Maraschi *et al.* (1994), report on the multiwavelength observation of 3C279 made during 1992 and 1993 when this object appeared to be in a quiescent state. These measurements again do not rule out either the SSC or EC γ-ray production models.

The HBL PKS 2155-304, an object very similar in many respects to Mrk 421, has also been targeted as a part of large scale contemporaneous multiwavelength campaigns. The analysis from one such campaign during 1991 is presented by Edelson *et al.* (1995). This campaign and a subsequent campaign during May 1994 are also discussed by Urry (1996). During the 1991 observations, the light curve of PKS 2155-304 was seen to vary, with the amplitude of this variation seeming to

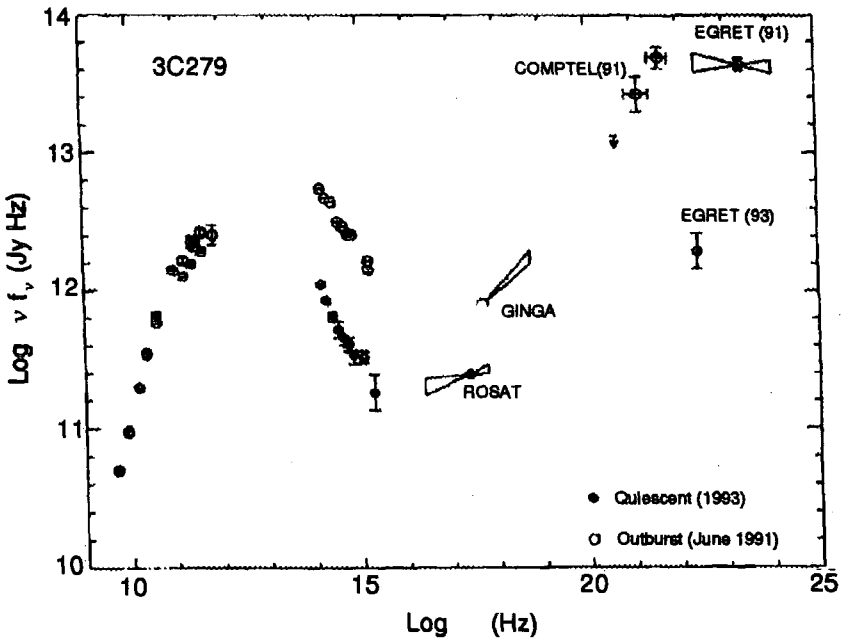

Figure 5.10: The spectral energy distribution of 3C279 during both the flare state (June 1991 observations) and quiescent state (observations made during 1992 and 1993). From Maraschi *et al.*, (1994)

be independent of wavelength. This result is contrary to that expected from a synchrotron flare caused by an increase in the population of energetic electrons. During the second campaign in 1994 a bright flare was observed in X-rays, followed by an EUV flare one day later and a broader, low amplitude UV flare two days later. This second flare with the time varying emission at different wavelengths is exactly what is expected from a synchrotron flare (see Figure 5.11). It is concluded that the 1991 variability was probably not due to a synchrotron flare, since the observed time scales were energy independent. It may have possibly been due to a microlensing event, as the galaxy passed behind a dense star cluster at the redshift on a known Lyman-alpha absorption system (Treves *et al.*, 1997).

5.5.1 TeV Variability

The first observation of TeV γ-ray variability occurred during a multiwavelength campaign on Mrk 421 (Kerrick *et al.*, 1995a). A flare was observed during May

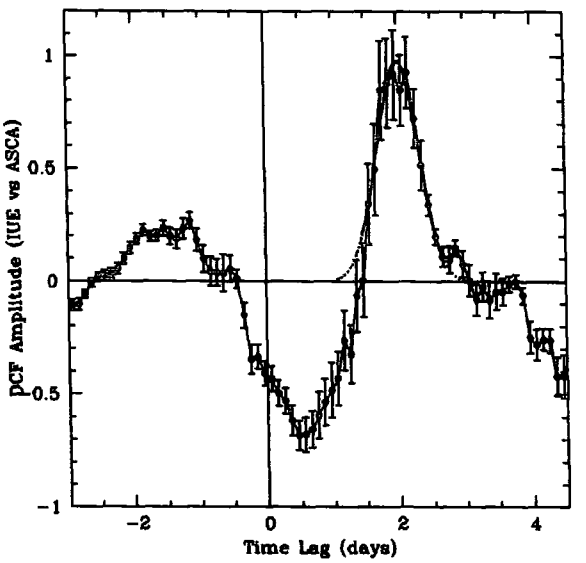

Figure 5.11: Cross correlation of May 1994 ASCA and IUE light curves of PKS 2155-304, showing that the X-ray flux leads the UV by ~2 days. From Urry (1996).

14^{th}-15^{th} 1994, the TeV flux increased by a factor of 10 and had a rise time of close to one day. This dramatic flux increase preceded an X-ray flare observed with the ASCA satellite by one day (Takahashi *et al.*, 1996). The TeV γ-ray flare was unexpected in view of the fact that the EGRET detector had observed Mrk 421 over six periods during 1991-1993 without showing any evidence for variability. The EGRET experiment also showed no flux increase during the period of the TeV and X-ray flares.

The X-ray data during this flare showed a doubling time scale of 12 hours. The shape of the X-ray spectrum varied during the observation (see Figure 5.13), in that hard X-rays always led the soft X-rays, both in brightening and dimming of the source. The $0.5 \rightarrow 1.0\,\mathrm{keV}$ photons lagged those in the $2 \rightarrow 7.5\,\mathrm{keV}$ band by one hour.

Macomb *et al.* (1995), have reported on the complete multiwavelength analysis of the May 1994 flare. It is concluded that there is little evidence for variability on the scale of the X-ray and TeV flux increases at any other wavelengths. The absence of flux variability below these spectral breaks suggests that the X-ray and TeV

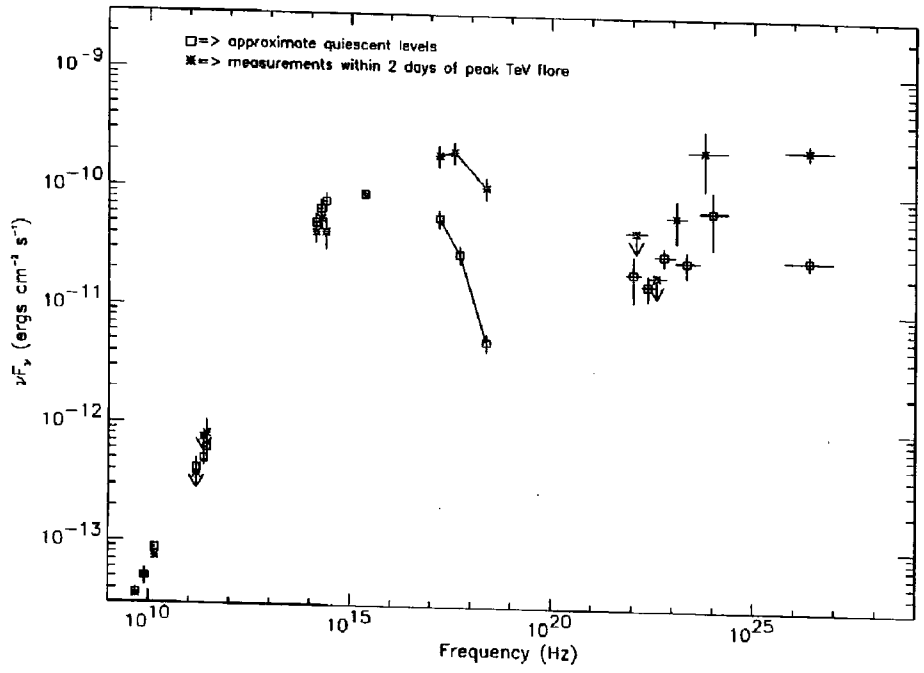

Figure 5.12: Multiwavelength spectrum of Mrk421 near the time of the flare (*asterisks*) and during 'quiescent' periods (*squares*). From Macomb *et al.* (1995).

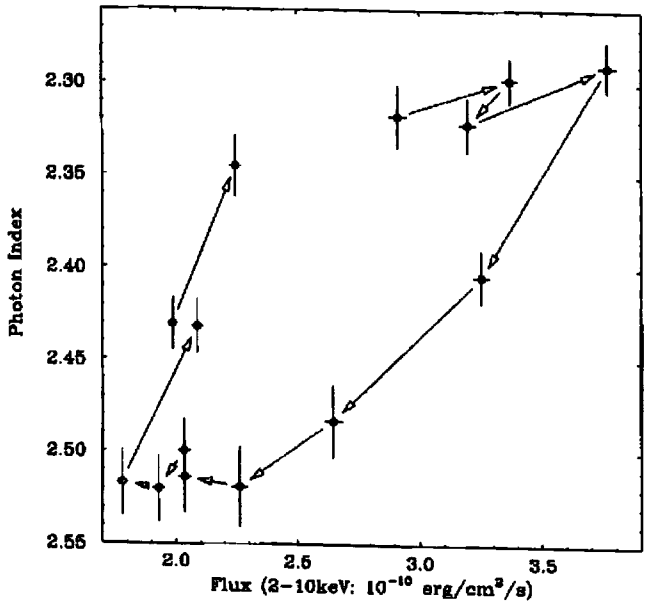

Figure 5.13: Evolution of the X-ray spectrum of Mrk 421 as a function of the X-ray flux. From Takahashi *et al.* (1996).

components are correlated. A natural conclusion is that the high energy population of electrons responsible for the X-ray synchrotron emission is extended during the flare to slightly higher energies. This is possible within a region of the jet where a shock acceleration mechanism suddenly increases in efficiency and extends the high energy electron population tail. The resultant increase in X-ray flux will be followed naturally by an increase in TeV emission through the inverse Compton process. The SSC model predicts that the TeV flux increase should be larger than that in X-rays, due to both the scattering electrons and soft photons having increased energy. The observations of this flare are consistent with the SSC model, but can not rule out another source of soft photons. The relatively short time scales for both the rise time ($\approx$ 2days) and decay ($\leq$ 12 days) of the flare strongly constrains the hadronic models on the basis of emission size constraints and the lack of any observed MeV flux increase.

Buckley *et al.* (1996) have reported on the 1995 observations of Mrk 421, including a flare observed on April 26^{th}. Although this flare was less intense than the 1994 flare, with a flux increase of only a factor of five, its rise and decay time was considerably shorter at $\leq$1 day. Analysis of the predicted SED for Mrk 421 from Inoue and Takahara (1996), reveal that the TeV emission may be at a break in the inverse Compton spectrum, analogous to the synchrotron break observed in X-rays. If either the electron acceleration efficiency or magnetic field strength changes, then the frequency at which the synchrotron spectrum breaks will alter. It is predicted that the inverse Compton spectral break will also change by a corresponding factor, with the result that the TeV flux becomes highly variable.

The most dramatic flaring occurrences of Mrk 421 were seen over an 8 day period in May 1996 (Gaidos *et al.*, 1996). On the 7^{th} May 1996, a flare was observed with the Whipple telescope which showed a flux increase of a factor of 50 and a doubling time scale of approximately 1 hour (see Figure 5.14). This flare corresponded to an observed rate of 12.5 γ-rays min^{-1} at its peak, the largest known TeV flux yet detected. A second flare occurred on the 15^{th} May 1996, which showed a flux increase of between a factor of 20 and 25. Extraordinarily the whole of this second outburst

lasted for only 30 minutes. Such large flux increases over correspondingly short time scales are very challenging to the current theoretical models. From causality arguments, the size of the TeV emission region must have been very small, $1 < R < 10$ light hours (assuming a beaming factor of $\delta \sim 10$): far smaller than predicted by current theories. These two flares seem to be quite different from the previous flux increases, both in size and duration. X-ray data obtained by the RXTE satellite during this period showed a high degree of variability and in contrast to earlier near simultaneous X-ray/γ-ray observations of Mrk 421, the variability amplitude is much larger at TeV than X-ray energies (Schubnell, 1997). This is exactly what is predicted by the SSC model. The high intensity and short timescale variation may be a result of an acceleration process not previously observed from blazars. One such process which has been discussed is magnetic reconnection, which is believed to produce short duration and high intensity flares on the surface of the Sun (Hillas, 1996b).

During 1997, Mrk 501 has shown a dramatic flux increase. The RXTE satellite observed an enhanced flux between JD 50,500 and approximately JD 50,650. The TeV emission has correspondingly increased, with a general rise of a factor between 8 and 16 above the Whipple 1995 level. Superimposed upon this increase, strong flaring behaviour has also been observed. During this period, TeV emission has detected by Whipple (Quinn *et al.*, 1997), HEGRA (Aharonian *et al.*, 1997), CAT (Barrau *et al.*, 1997) and the Telescope Array prototype (Aiso *et al.*, 1997). The HEGRA group report that the spectrum of Mrk 501 during this period is consistent with a differential energy spectrum between, 1 TeV and 10 TeV, of $2.49 \pm 0.11 \pm 0.25$. Figure 5.15 shows the TeV flux as measured by the HEGRA and CAT Čerenkov telescopes during this high state. The possible production mechanism for this long timescale flux increase is currently unknown.

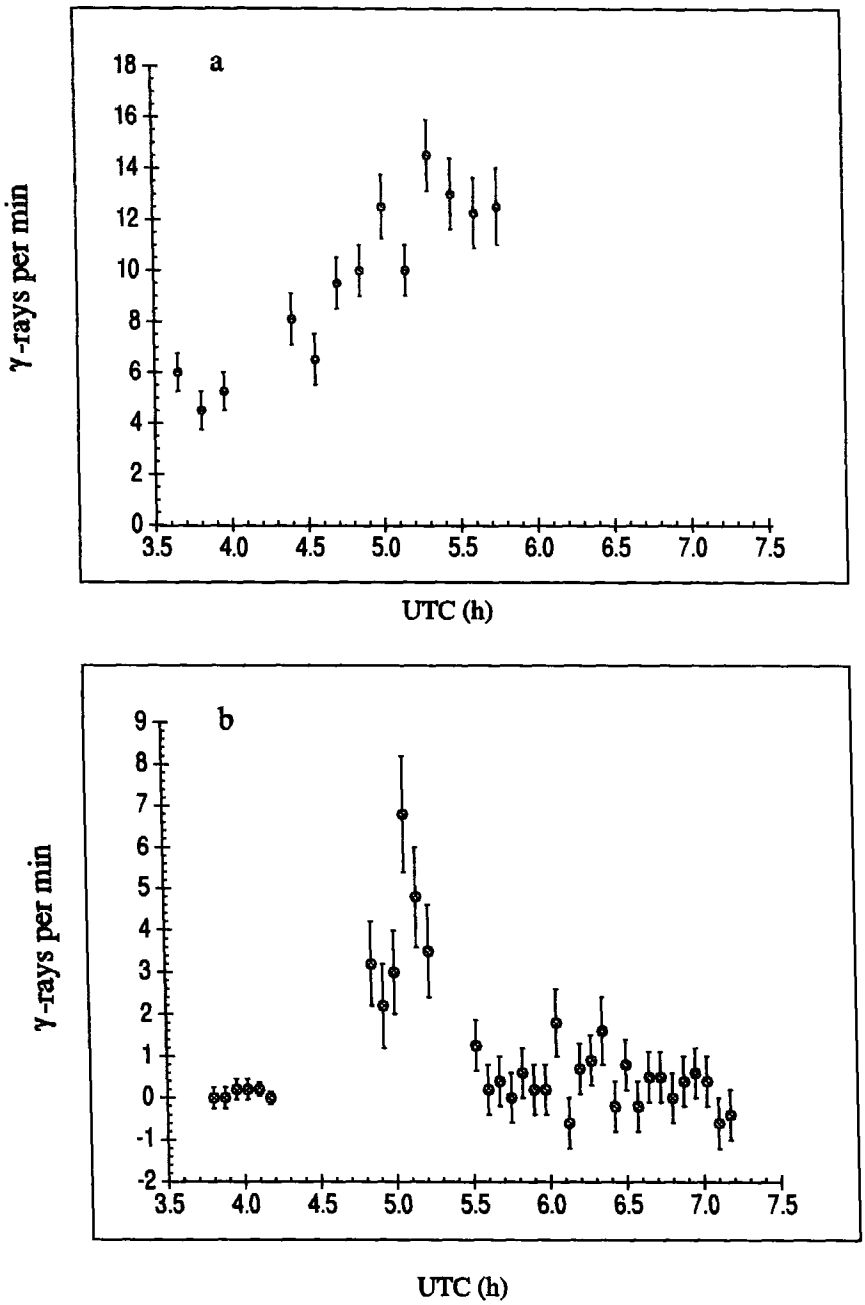

Figure 5.14: Temporal histories of two flares from Mrk421 during May 1996. Rates are determined from the excess events after background subtraction in the interval *alpha* $< 15°$. The time axes are coordinated universal time (UTC) in hours. For the 7 May flare (a), each point is a 9-min integration; for the 15 May flare (b), the integration time is 4.5 min. The error bars are statistical standard deviations. From Gaidos *et al.* (1996).

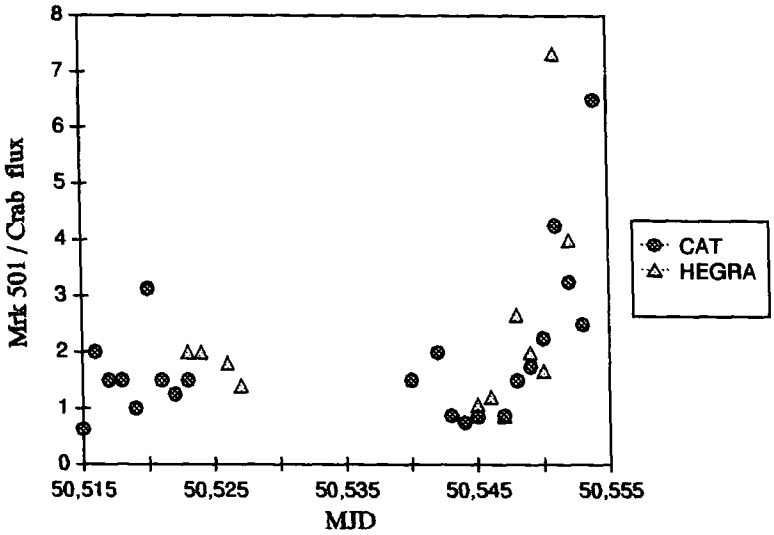

Figure 5.15: The Mrk 501 flux as a fraction of the Crab flux for the HEGRA and CAT experiments during April and May 1997.

5.6 Southern Hemisphere Candidate Sources

Observations of southern hemisphere blazars at TeV energies have until recently been very limited, with the majority of telescope time spent observing important galactic objects. As the duty cycles of Čerenkov telescopes are so limited, it is obviously of vital importance to make an informed decision upon which blazars will form the basis of an observing program.

The northern hemisphere Čerenkov telescopes, as reported in Section 5.1.2, have detected two blazars, Mrk 421 and Mrk 501, both of which are HBLs (see Section 5.3.2). It is also worth noting that upper limits have been published for a further 35 extragalactic objects, 15 of which are EGRET detected sources. This may suggest that HBLs may have an intrinsically high TeV flux, compared to LBLs and FSRQs. The ideas behind this have been outlined in Section 5.3, where it was shown that typically the synchrotron energy peak (ν_p) is a factor $10^3 \rightarrow 10^4$ higher in energy for HBLs than in the case of LBLs and FSRQs. This may imply that an EGRET detection may not be a strong indicator of a probable high TeV flux. The detection of only 2 HBLs with EGRET indicates the possibility that the power

emitted by LBLs and FSRQs peak within the MeV to GeV energy range, while the HBL sample peak at considerably higher energy, closer to TeV. X-ray measurements of both the flux and spectral indices, seems to provide a more reliable indicator of possible TeV γ-ray emission from blazars (the ROSAT observations of BL Lac objects are presented in Lamer *et al.*, 1996).

A second important consideration is the distance from the solar system at which the extragalactic object is situated. As shown in Section 5.2, TeV γ-rays are believed to be attenuated by pair production with the intergalactic infrared background. Current estimates suggest that photons with energies greater than 1 TeV will become strongly attenuated from sources which are situated at $z > 0.1$ (Mrk 421 and Mrk 501 are at $z = 0.031$ and $z = 0.033$ respectively).

These considerations have been brought together by Stecker *et al.* (1996), coupled with a SSC model for γ-ray production. The model used for the IR background is that described in Stecker and de Jager (1996). Predicted fluxes are produced for a number of blazars at 100 MeV, 300 GeV and 1 TeV (summarised in Table 5.4). It is concluded that low redshift HBLs may be the only extragalactic γ-ray sources observable at TeV energies. This conclusion is tentative, as only two blazars have been detected at this energy to date (with the possibility of a third, 1ES2344+514). The TeV γ-ray observations of these limited number of blazars are providing vital clues in establishing areas such as the extragalactic infrared background, broadband production mechanisms and flaring mechanisms. The observations of a number of southern hemisphere blazars obtained with the Mark 6 telescope are presented in Chapter 6.

Table 5.4: Predicted γ-ray fluxes for low-redshift XBLs (HBLs) observable from Narrabri (Mrk 421 and Mrk 501 are included for comparison). After Stecker *et al.* (1996).

1ES Name	Other Name	Z	$\phi(>0.1\text{GeV})$ $10^{-7}\text{cm}^{-2}\text{s}^{-1}$	$\phi(>0.3\text{TeV})$ $10^{-11}\text{cm}^{-2}\text{s}^{-1}$	$\phi(>1.0\text{TeV})$ $10^{-12}\text{cm}^{-2}\text{s}^{-1}$
1ES0323 + 022	1H	0.147	0.11	0.40	0.15
1ES0347 - 121		0.188	0.05	0.38	0.08
1ES0548 - 322	PKS	0.069	0.56	1.3	1.2
(1ES1101 + 384	Mrk 421	0.031	1.43	2.3	3.6)
1ES1212 + 078	Mrk 180	0.136	0.22	0.07	0.03
1ES1312 - 423	MS	0.105	0.19	0.24	0.15
(1ES1652 + 398	Mrk 501	0.034	1.4	2.1	3.2)
1ES2005 - 489	PKS	0.071	0.70	0.91	0.84
1ES2155 - 304	PKS	0.116	3.9	1.7	0.88

Chapter 6

Blazar Observations

6.1 Introduction

In this chapter the observations of blazars made with the Mark 6 telescope will be described. In Section 5.6, it was suggested that relatively close HBLs are the best candidate sources for possible TeV γ-ray emission. We have obtained relatively large data sets from three of these objects; PKS 0548-322, PKS 2005-489 and PKS 2155-304. Data have also been obtained from a close LBL; PKS 1514-24.

The parameter selections applied to the data are those described in Section 4.5. For data to be accepted as suitable for analysis a number of criteria had to be satisfied, including

1. Raw count rate variations between corresponding ON/OFF scans $\leq 2.5\sigma$
2. No evidence for poor weather/atmospheric conditions or condensation/ice forming on the mirror surfaces
3. No hardware problems (e.g. CCD information available, all PMTs operational)
4. Zenith angle less than 40°

The data passing these criteria were calibrated, determining the pedestal, noise

and gain of each PMT. The software padding procedure, described in Section 4.1.2, was applied to the data to remove the possibility of any systematic biases due to field brightness variations. The data analysis was undertaken during June, July and August 1997.

Following an outline of the observations and analysis for each of these objects, the implications of the results will be discussed. The multiwavelength data shown in the broad band energy distributions have been collected using the NASA/IPAC Extragalactic Database (NED) and from Giommi *et al.* (1995). Data provided by the ASM/RXTE quick look team have also been used.

6.2 Observations

6.2.1 PKS2005-489

The HBL PKS 2005-489 was first discovered in the Parkes 2.7 GHz survey (Wall *et al.*, 1975) and was identified as a BL Lac object on the basis of its flat radio spectrum and featureless continuum (Wall *et al.*, 1986). Very weak emission lines were detected during a low state, which allowed the determination of its redshift, $z = 0.071$ (Falomo *et al.*, 1987). PKS 2005-489 is one of the brightest BL Lac objects known, including a detection in the EUV band, which is rare for an extragalactic object (Marshall *et al.*, 1995). The ROSAT observations and spectral variability of this source have been studied by Sambruna *et al.* (1995). This object was detected by the EGRET experiment during observing phase I with a significance of 4.3σ (Fichtel *et al.*, 1994), but the significance fell to 3.8σ in the generation of the Second EGRET Catalog and was therefore not included (Thompson *et al.*, 1995). Although PKS 2005-489 is, by definition, an RBL (it is included in the complete 1 Jy radio catalog; Stickel *et al.*, 1991), on the basis of its radio to X-ray flux it can be categorised as an 'XBL-like' object (Giommi & Padovani, 1994). The ratio of the $0.3 \rightarrow 3.5$ keV to 5 GHz fluxes, leads to this object being classed as an HBL (see Equation 5.4).

Table 6.1: Mark 6 Observing log for PKS 2005-489 during 1996

Date (1996)	No. of scans
Aug 10	12
Aug 11	5
Aug 12	15
Aug 13	4
Aug 14	11
Aug 17	5
Total	52 (12.5 hr)

PKS 2005-489 was observed during August 1996 with the Mark 6 telescope. During these observations the telescope was operated in an OFF/ON/ON/OFF observing mode (see Section 3.6). The data passing the selection criteria given above are listed in Table 6.1. A total of 52 scans passed this selection process, resulting in 12.5 hours of ON and OFF source data.

During the observations on the 10, 11, 12, 13 and 14^{th} August 1996, three charge-time converters (QT units) associated with the PMTs 2C13→3C18; 4C6→4C18 in the central Mark 6 detector package were seen to develop a fault. For the 'null event' triggers, which are used for calibration purposes, the gate time of the charge time converters for these PMTs extended from the standard 40 ns to approximately 72 ns. This resulted in an artificially large pedestal and noise being determined for these tubes. Analysis of the unaffected tubes revealed that the pedestal and noise remained almost constant throughout the period of an observation. This fact was supported by the application of a method for determining the pedestals without the use of these 'null events', a procedure described in Section 4.1.1. As a first order correction, the pedestal and noise from the scan preceding the fault occurring were applied to all subsequent scans. This is only possible because the ON and OFF fields contain no bright stars, which would introduce significant sky noise differences.

The parameter selections are those given in Table 4.2. The number of events

Table 6.2: Number of events remaining after parameter selections for PKS 2005-489

Parameter selections	ON source	OFF source	Difference
Raw counts	421738	422390	-652 (-0.7σ)
Parameter Selected	9257	9113	144 (1.1σ)
Alpha < 22.5°	2606	2530	76 (1.0σ)

passing the parameter selections are shown in Table 6.2.

The difference between the *alpha* distributions ON and OFF source is shown in Figure 6.1. There is no evidence for γ-ray emission within this data.

To test for γ-ray emission from a region removed from the radio source position a false source analysis has been applied. A 2.0° × 2.0° field surrounding the source position is split into a 20 by 20 square grid. At each of these assumed positions the parameters are recalculated and a significance is derived. An offset source may be due to systematic errors within the telescope steering or a displaced γ-ray emission region, as is a possibility in supernova remnants (but is highly unlikely from extragalactic objects). A false source analysis from the region surrounding PKS 2005-489 is shown in Figure 6.2. There is no evidence for significant deviation from the expected statistical distribution.

A three sigma upper limit above 300 GeV has been determined, assuming a collecting area of 3×10^4 m^2 and a 50% γ-ray retention ratio

$$F_\gamma(\geq 300 \text{ GeV}) \leq 3.2\,(\pm 0.88_{sys} \pm 0.55_{stat}) \times 10^{-11} \text{ cm}^{-2}\text{s}^{-1}. \qquad (6.1)$$

The systematic component of the error arises from the uncertainty in the collecting area/threshold energy determined through simulations (see Section 3.7).

The position of this flux limit within the broad band energy distribution is shown in Figure 6.3, the predicted fluxes produced by Stecker *et al.* (1996) are also shown (see Table 5.4). The RXTE satellite has recently started producing daily flux mea-

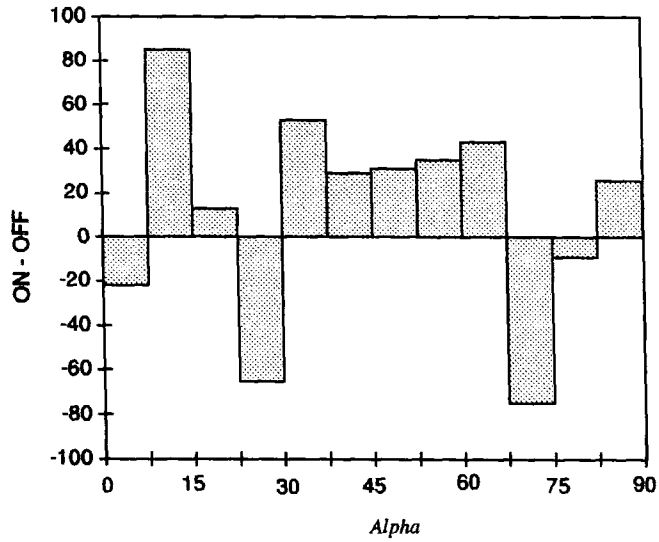

Figure 6.1: The difference between the *alpha* distributions ON and OFF source for PKS 2005-489. No bias towards low values of *alpha* ON source can be seen.

surements of PKS 2005-489, prompted by the correlation between the X-ray and TeV flux variations of Mrk 501 during the 1997 flaring activity. The X-ray flux during June and July 1997 is shown in Figure 6.4. Although the quiescent flux from this source seems to be close to, or below the detector sensitivity, there does seem to be a number of periods of enhanced emission (MJD 50617 for example). This X-ray data will provide vital contemporaneous information to be used in conjunction with future Mark 6 observations of this object.

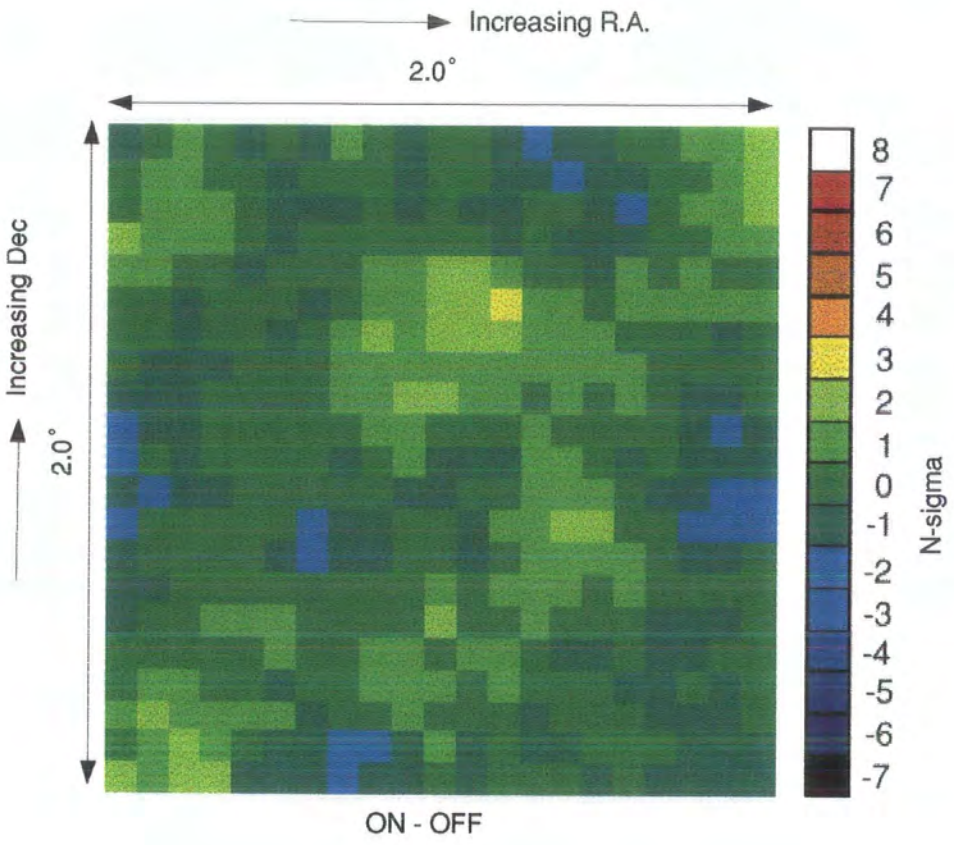

Figure 6.2: A false source analysis of the region surrounding PKS 2005-489. There is no evidence in the above plot for significant deviations from the expected statistical distribution.

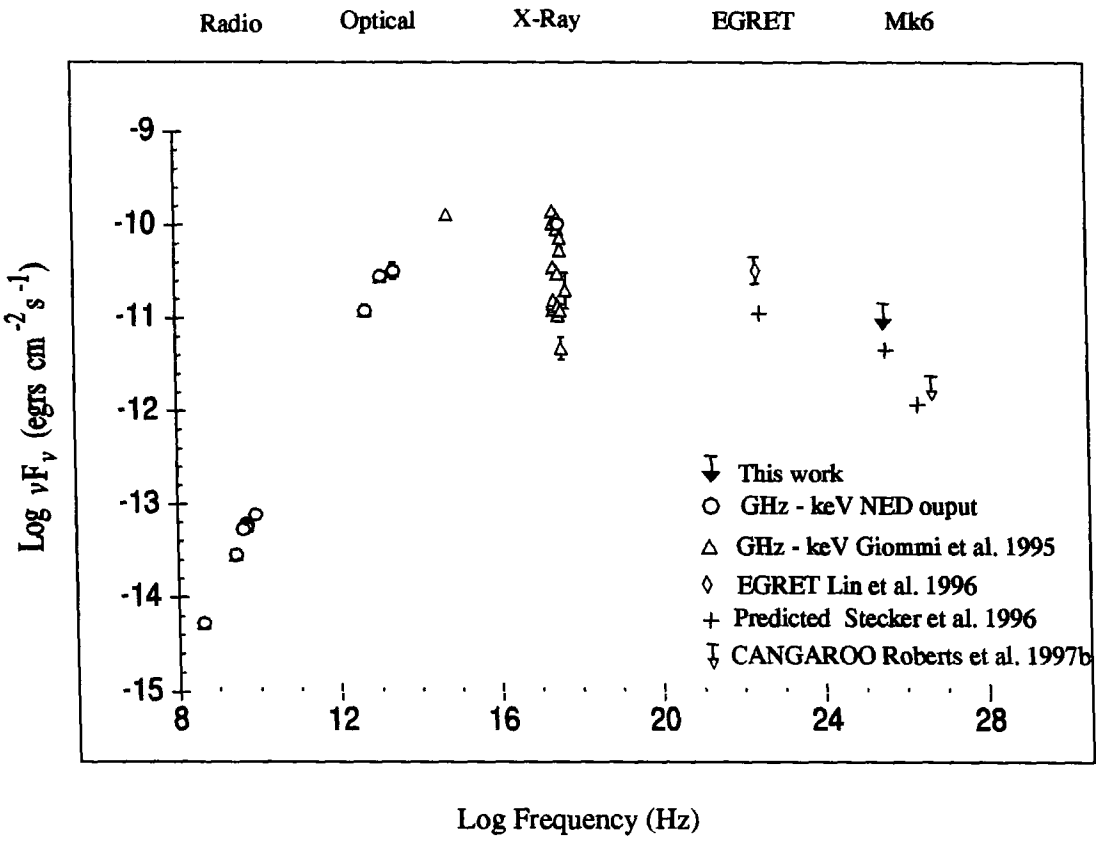

Figure 6.3: The spectral energy distribution of PKS 2005-489

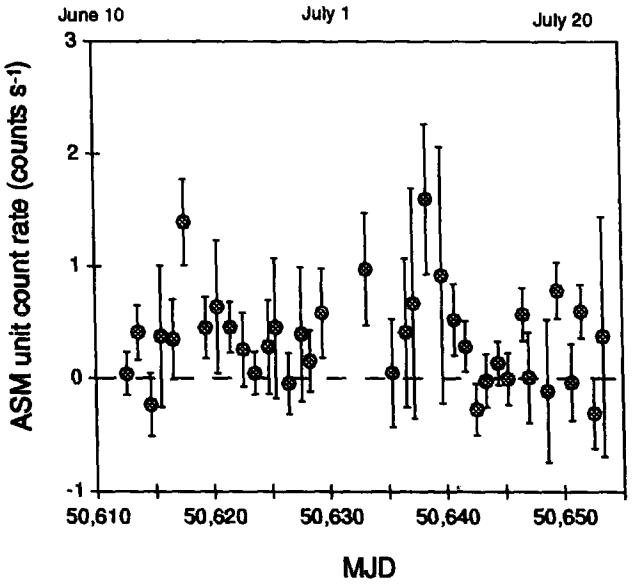

Figure 6.4: The averaged daily X-ray flux measurements of PKS 2005-489 during June and July 1997 produced by the RXTE satellite. Although there seems to be little steady detectable emission, a few periods of enhanced emission are observed.

Table 6.3: Mark 6 Observing log for PKS 2155-304 during 1996

Date	No. of scans	Date	No. of scans
Aug 14	6	Oct 2	1
Sept 3	2	Oct 9	4
Sept 4	2	Oct 10	3
Sept 5	9	Oct 12	2
Sept 6	6	Oct 13	4
Sept 7	8	Oct 14	5
Sept 8	4	Oct 15	1
Sept 9	2	Nov 2	2
Sept 10	8	Nov 7	5
Sept 12	3	Nov 10	2
Sept 14	7	Nov 11	2
Sept 15	7	Nov 12	5
Sept 17	5		
Sept 18	3		
Total			108 (25.25 hr)

6.2.2 PKS2155-304

The object PKS 2155-304 is often considered to be the archetypal XBL. It has a history of strong, rapid broadband variability and is one of the brightest BL Lac objects from optical to X-ray energies (see Section 5.5). This object and Mrk 421 are the only two XBLs detected by EGRET (Vestrand *et al.*, 1995). The EGRET experiment detected a very hard spectrum from PKS 2155-304, with a spectral index of 1.71 ± 0.24. Vestrand *et al.*, conclude that this very hard spectrum in conjunction with its relatively low redshift ($z = 0.116$) make PKS 2155-304 a prime candidate for TeV γ-ray emission. The ROSAT observations of PKS 2155-304 are reported in Lamer *et al.* (1996).

PKS 2155-304 was observed during August, September, October and Novem-

Table 6.4: Number of events remaining after the parameter selections for PKS 2155-304

Parameter selections	ON source	OFF source	Difference
Raw counts	846828	846835	-7 (-0.005σ)
Parameter Selected	13847	13944	-97 (-0.58σ)
Alpha $< 22.5°$	3709	3714	-5 (-0.05σ)

ber 1996. A total of 108 scans passed the initial selection criteria, the details of these data are presented in Table 6.3. The number of events passing the parameter selections are given in Table 6.4. The difference between the ON and OFF *alpha* distributions is shown in Figure 6.5 and a false source analysis of the region surrounding PKS 2155-304 is presented in Figure 6.6. There is no evidence for any γ-ray emission above 300 GeV during our observations. The 3σ upper limit for the flux above 300 GeV is given by (again assuming a 3×10^4 m^2 collecting area and a 50% γ-ray retention) :

$$F_\gamma(\geq 300 \text{ GeV}) \leq 1.9\,(\pm 0.76_{sys} \pm 0.6_{stat}) \times 10^{-11} \text{ cm}^{-2}\text{s}^{-1}. \qquad (6.2)$$

The position of this upper limit within the broadband energy distribution is shown in Figure 6.7. The RXTE satellite produced daily X-ray flux measurements during the period of our observations, which are shown in Figure 6.8. The shaded areas within this diagram represent the dark moon period, during which the observations were obtained. The RXTE data indicate no X-ray variability which is contemporaneous with our observations, although an X-ray flare may have been observed during full moon between our September and October observing periods.

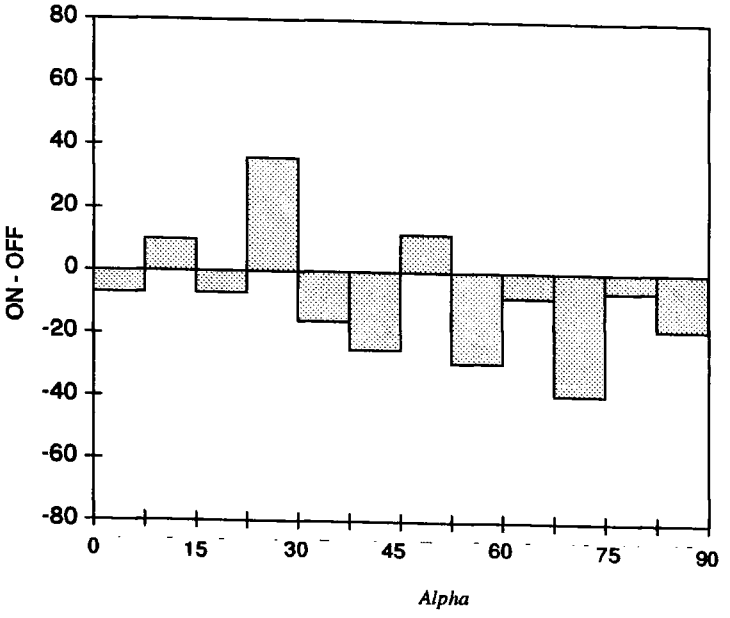

Figure 6.5: The difference between the *alpha* distributions ON and OFF source for PKS 2155-304.

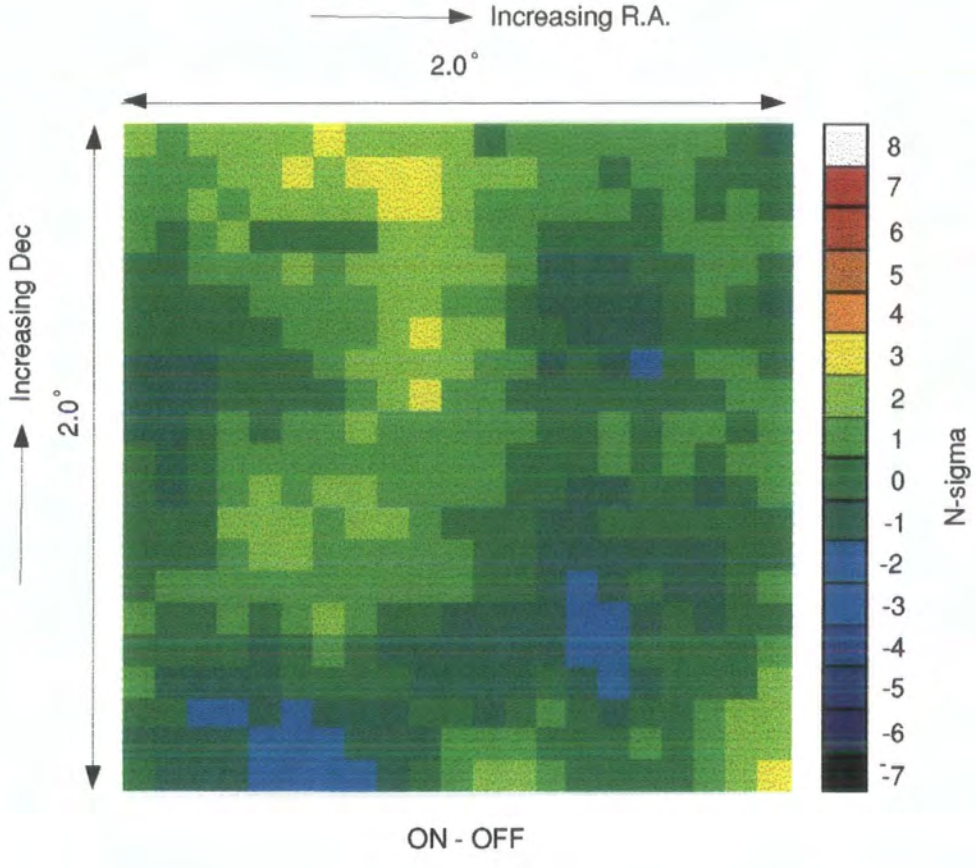

Figure 6.6: A false source analysis of the region surrounding PKS 2155-304. No significant deviation from the expected statistical distribution is observed.

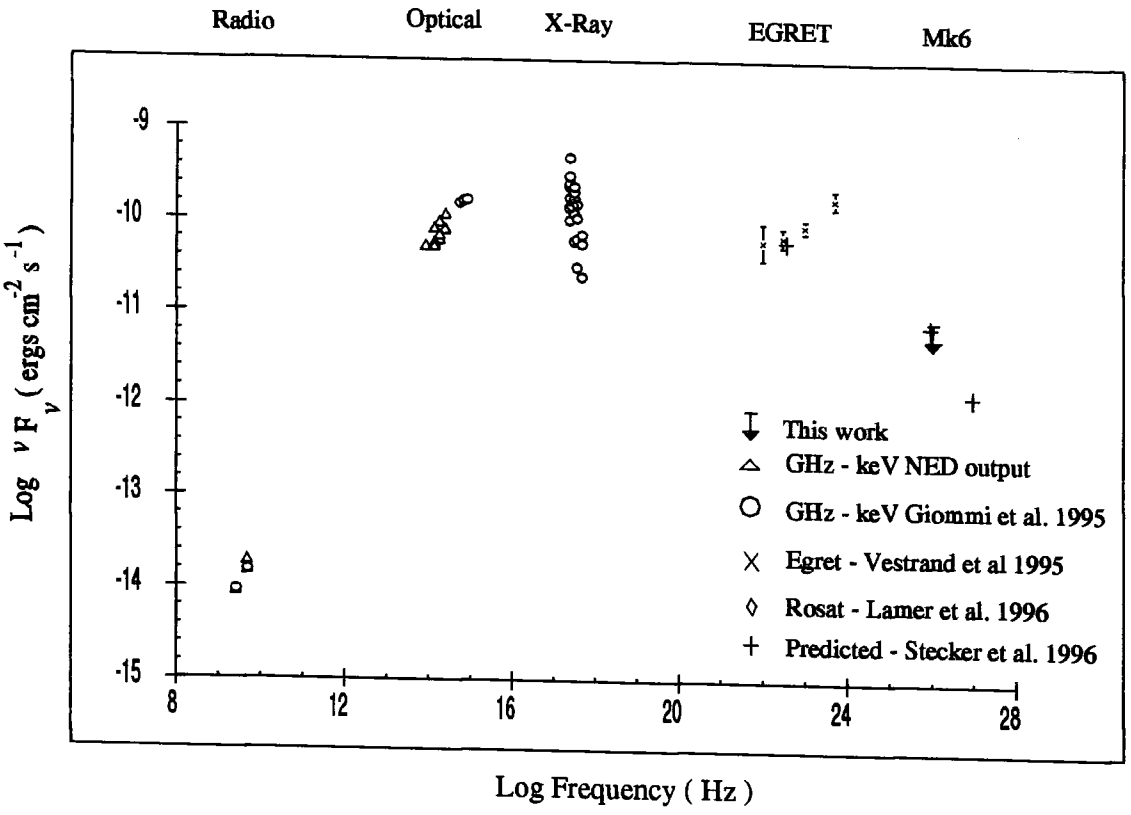

Figure 6.7: The spectral energy distribution of PKS 2155-304

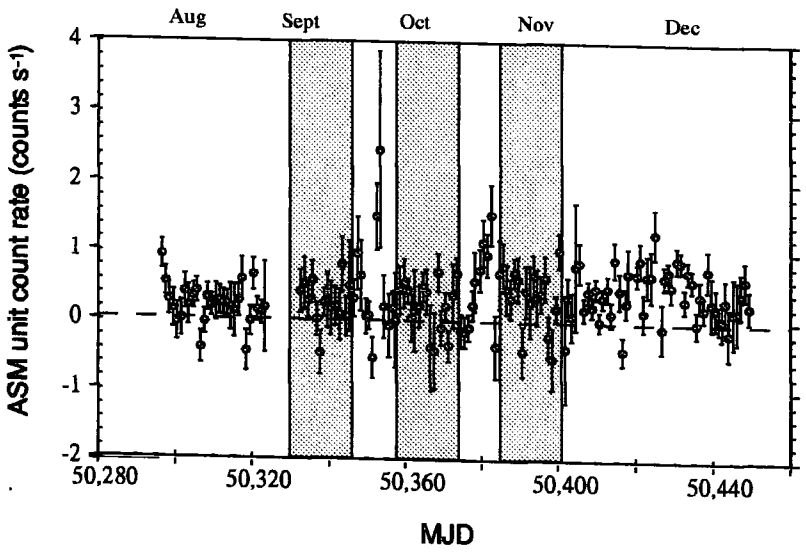

Figure 6.8: The daily X-ray flux from PKS 2155-304 as measured with the RXTE during late 1996. Shaded areas indicate dark moon periods when VHE gamma ray observations were possible from Narrabri.

6.2.3 PKS0548-322

The HBL PKS 0548-322 is one of the brightest BL Lacs in X-rays and has subsequently been extensively studied at this energy (Einstein IPC - Maccagni *et al.*, 1983; EXOSAT - Barr *et al.*, 1988; Ginga - Tashiro *et al.*, 1995; ROSAT - Lamer *et al.*, 1996). It has been concluded that although this object exhibits a relatively flat spectrum, significant flux and spectral index variations are observed. The large X-ray flux and low redshift (z= 0.069) make PKS 0548-322 a prime candidate for TeV emission.

A total of 50 pairs of ON/OFF scans (11.66 hrs), listed in Table 6.5, passed the initial selection criteria. The number of events passing the parameter selections are shown in Table 6.6 and the difference between the ON and OFF *alpha* distributions is shown in Figure 6.9. A false source analysis for the region surrounding PKS 0548-322 is shown in Figure 6.10. No evidence of VHE γ-ray emission was observed during these observations. The 3σ upper limit for the integral flux above 300 GeV is given by

$$F_{\gamma}(\geq 300 \text{ GeV}) \leq 3.0\,(\pm 1.2_{sys} \pm 1.0_{stat}) \times 10^{-11} \text{ cm}^{-2}\text{s}^{-1}. \qquad (6.3)$$

The position of this upper limit within the broadband energy spectrum is shown in Figure 6.11. No RXTE data were available during the period of our observations, but recently this object has been added to the 'quick look' program provided by this satellite.

Table 6.5: Mark 6 Observing log for PKS 0548-322 during 1996

Date	No. of scans	Date	No. of scans
Feb 18	6	Nov 7	6
Feb 19	6	Nov 10	5
Oct 10	4	Nov 11	2
Oct 12	5	Nov 12	7
Oct 14	1	Nov 13	6
Oct 15	2		
Total			50 (11.6 hr)

Table 6.6: Number of events remaining after parameter selections for PKS 0548-322

Parameter selections	ON source	OFF source	Difference
Raw counts	377304	378788	-1486 (-1.7σ)
Parameter Selected	6805	6847	-42 (-0.4σ)
Alpha < 22.5°	1823	1894	-71 (-1.2σ)

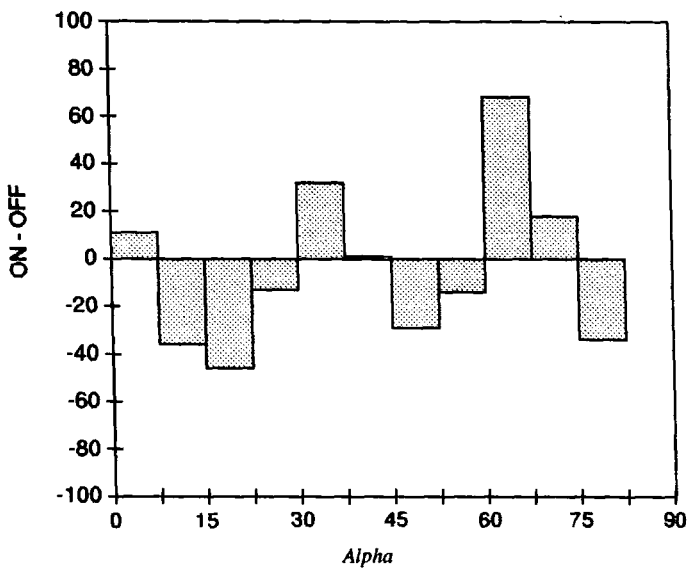

Figure 6.9: The difference between the *alpha* distributions ON and OFF source for PKS 0548-322.

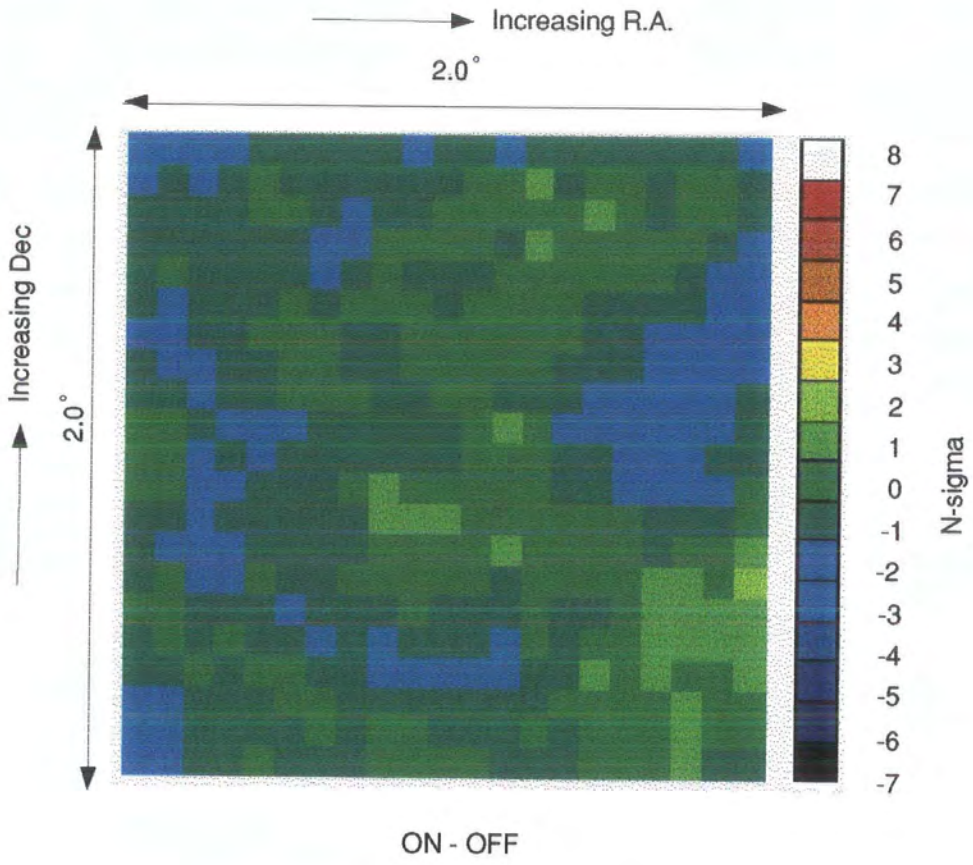

Figure 6.10: A false source analysis for PKS 0548-322. No significant deviation from the expected statistical distribution is observed.

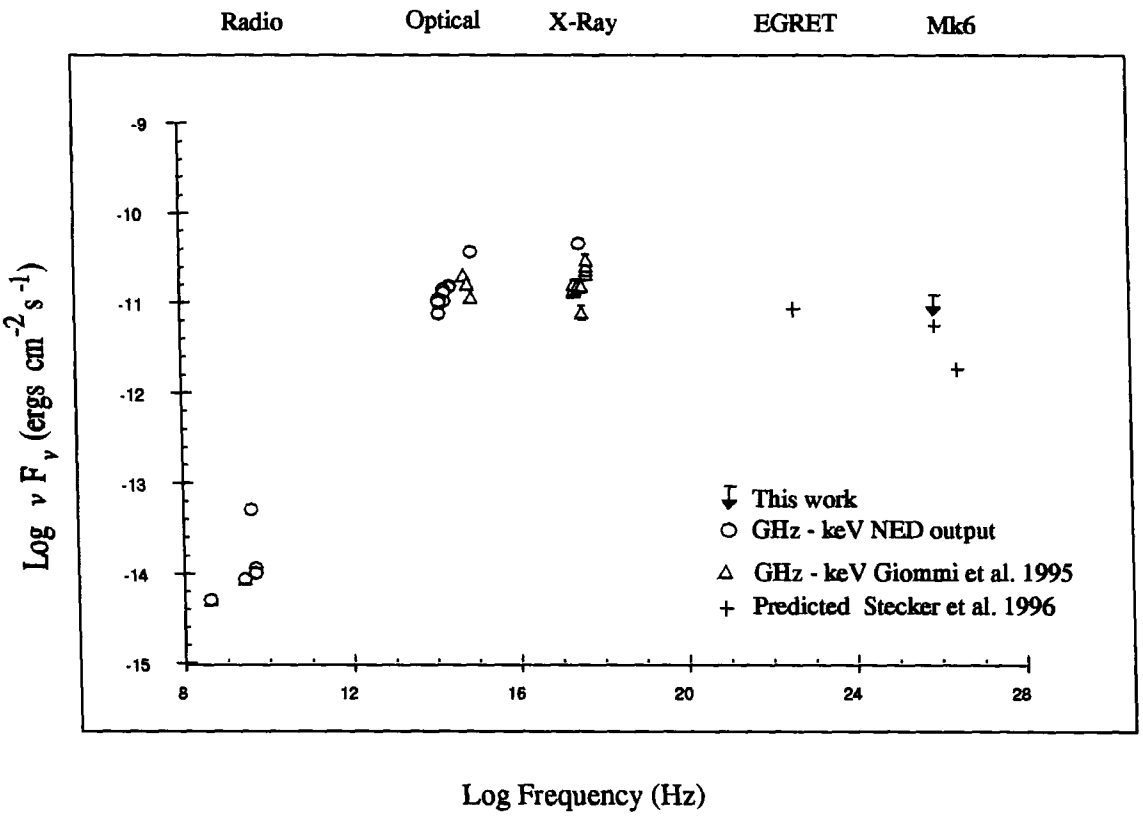

Figure 6.11: The spectral energy distribution of PKS 0548-322

Table 6.7: Mark 6 Observing log for PKS 1514-24 during 1996

Date	No. of scans	Date	No. of scans
April 14	4	April 19	11
April 15	7	April 20	8
April 16	10	April 21	4
April 17	8	April 22	9
April 18	9		
Total			70 (16.3 hr)

6.2.4 PKS1514-24

The LBL PKS 1514-24 (AP Librae) is one of the closest BL Lac objects visible from the southern hemisphere with a redshift of only, $z = 0.0486$. Optical observations have revealed a high degree of variability on the timescales of less than one day (Carini *et al.*, 1991). The proximity of this object prompted a series of observations to be undertaken with the Mark 6 telescope.

A total of 70 ON/OFF pairs of scans (16.3 hrs) from the 1996 observing season passed the initial selection criteria, these are listed in Table 6.7. The number of events passing the moment parameter selections are shown in Table 6.8 and the difference in the *alpha* distributions ON and OFF source is presented in Figure 6.12. A false source analysis for PKS 1514-24 is shown in Figure 6.13. There is no evidence for any TeV γ-ray emission during the period of the observations. The 3σ upper limit for the integral flux above 300 GeV is given by:

$$F_\gamma(\geq 300 \text{ GeV}) \leq 2.1\,(\pm 0.84_{sys} \pm 0.7_{stat}) \times 10^{-11} \text{ cm}^{-2}\text{s}^{-1}. \qquad (6.4)$$

The position of this flux limit within the broadband spectrum is shown in Figure 6.14.

Table 6.8: Number of events remaining after parameter selections for PKS 1514-24

Parameter selections	ON source	OFF source	Difference
Raw counts	293306	291857	1149 (1.5σ)
Parameter Selected	8508	8704	-196 (-1.6σ)
Alpha < 22.5°	2184	2292	-108 (-1.6σ)

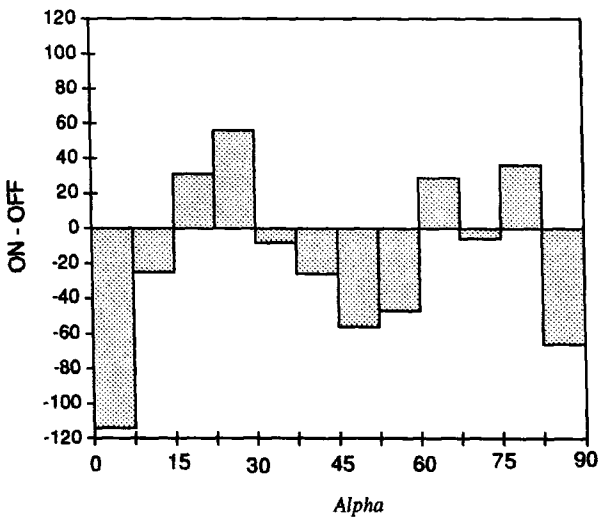

Figure 6.12: The difference between the *alpha* distributions ON and OFF source for PKS 1514-24.

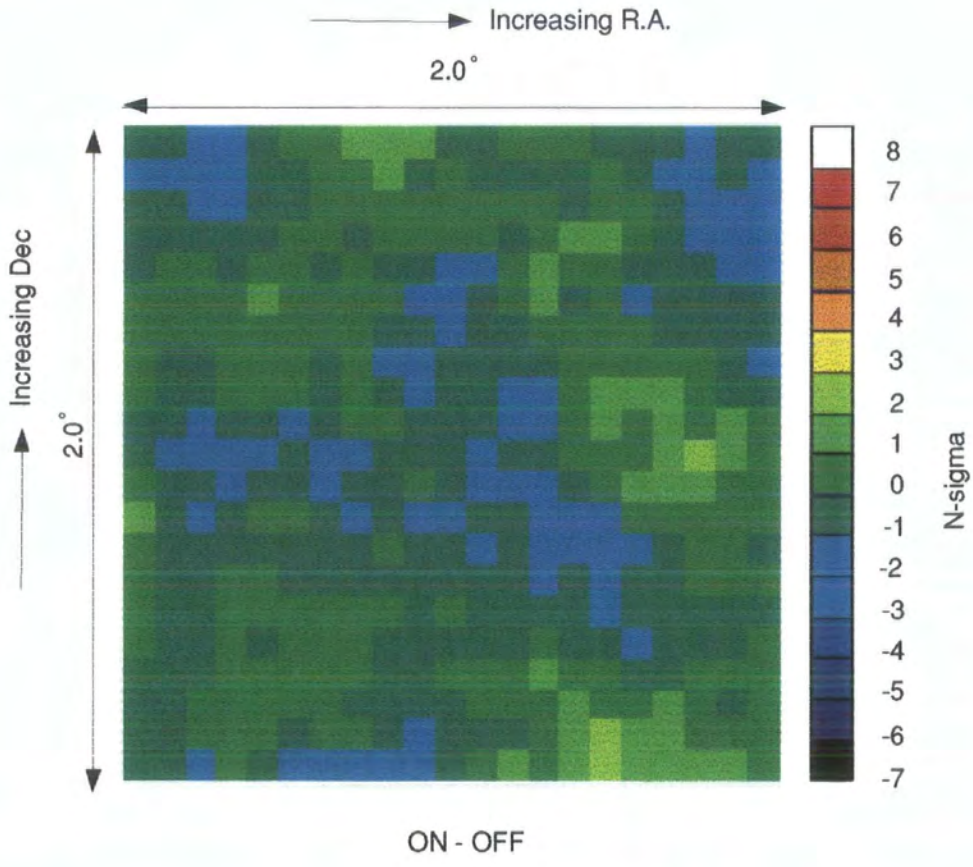

Figure 6.13: A false source analysis for the region surrounding PKS 1514-24. No significant deviation from the expected statistical distribution is observed.

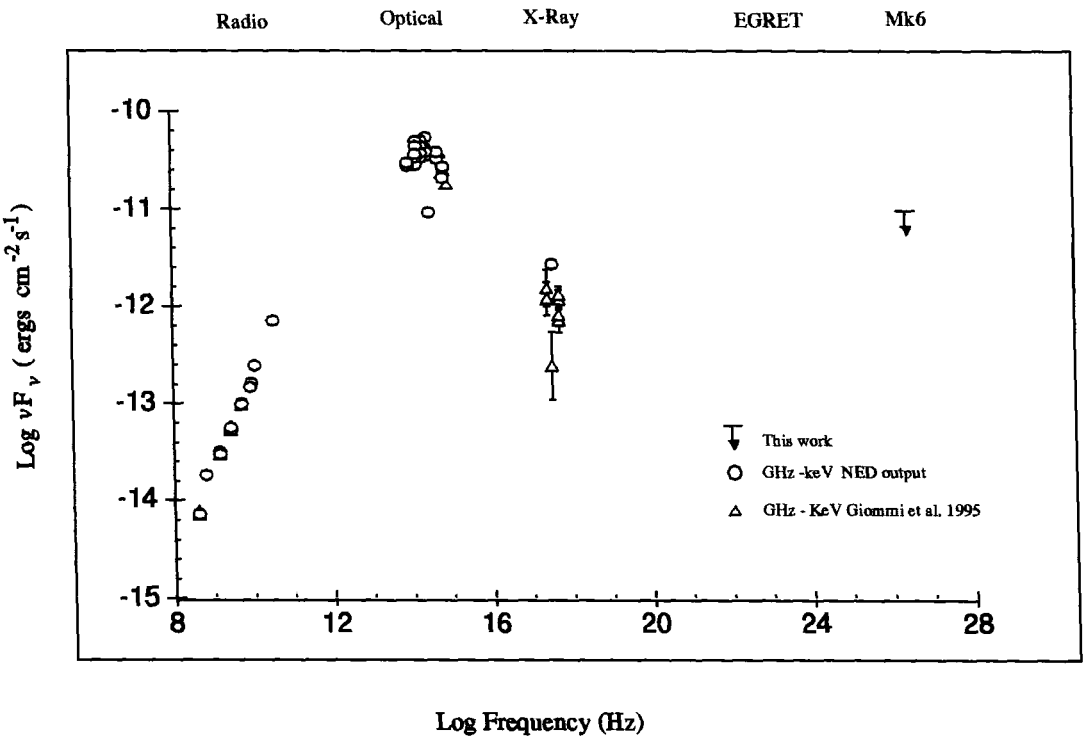

Figure 6.14: The spectral energy distribution of PKS 1514-24

Table 6.9: The predicted fluxes (from Stecker *et al.*, 1996) compared to the 3σ upper limits produced for the HBLs observed.

Source	Predicted flux > 300 GeV 10^{-11} cm^{-2} s^{-1}	3σ upper limit > 300 GeV 10^{-11} cm^{-2} s^{-1}
PKS 0548-322	1.3	3.0
PKS 2005-489	0.91	3.2
PKS 2155-304	1.7	1.9

6.3 Interpretation of these Observations

The observations of the three HBLs, PKS 0548-322, PKS 2005-489 and PKS 2155-304, have revealed no evidence for VHE γ-ray emission. The 3σ upper limits above 300 GeV are compared with the flux predictions made by Stecker *et al.* (1996) in Table 6.9. The flux upper limits produced for PKS 0548-322 and PKS 2005-489 are consistent with these predictions and correspond to approximately 65% and 70% of the average quiescent Mrk 421 flux respectively.

The upper limit produced for PKS 2155-304 is close to the flux predicted by Stecker *et al.* (1996). Table 5.4 reveals that the predicted γ-ray flux is becoming attenuated above 300 GeV (due to pair production with the IR background), compared to similar objects at lower redshifts. Figure 5.3 shows the effect of the IR background model used by Stecker *et al.*, in the calculation of these fluxes. Although the upper limit for PKS 2155-304 is not inconsistent with the predicted flux, its redshift of z=0.115 may rule out values of the infrared background significantly smaller than that used within the model (see Table 6.10). It should be noted that this conclusion is not fully supported by Stanev and Franceschini (1997) who have produced an upper limit for the IR background, based on recent TeV observations of Mrk 501, significantly lower at 10μm than that shown in Table 6.10.

The 3σ upper limit from PKS 2155-304 corresponds to a rate of less than 10 γ-rays per hour. For comparison, an object with a flux equivalent to the quiescent

Table 6.10: Values of the IR background used by Stecker *et al.* (1996) in the calculation of the predicted γ-ray fluxes from XBLs.

Wavelength μm	Energy Density 10^{-9} W m^{-2} sr^{-1}	Characteristic Absorbed γ-ray Energy (TeV)
1	10	0.3
2.5	9	1
10	5	4
30	6	10

level of Mrk 421 would have produced a 6.5σ detection for an observation of the duration obtained on PKS 2155-304. A flare on the scale of that observed by the Whipple group from Mrk 421 on May 14^{th}-15^{th} 1994 lasting for 2 hours would have produced a 14σ detection.

The LBL, PKS 1514-24, also shows no evidence of VHE γ-ray emission. No predictions concerning the expected TeV flux from this object have been presented within the literature.

To test for flaring activity, the selected data have been examined on a night-by-night basis. The significance of the number of ON source events over the background has been calculated for each observation. A histogram of these combined daily significances from the 4 objects is shown in Figure 6.15. The solid curve within the figure is the expected statistical distribution. It can be seen that there is no evidence for variability on any of the 49 nights. The mean of this distribution is $-0.046 \pm 0.146\,\sigma$. This also suggests that there is no low level γ-ray emission from these objects, which may have become evident from the improved statistics provided by combining the data from the four objects.

As it is suggested that the IR background will attenuate the higher energy γ - rays from distant extragalactic objects, the extensive air showers which produce the smaller signals recorded by the telescope have been analysed separately. It is

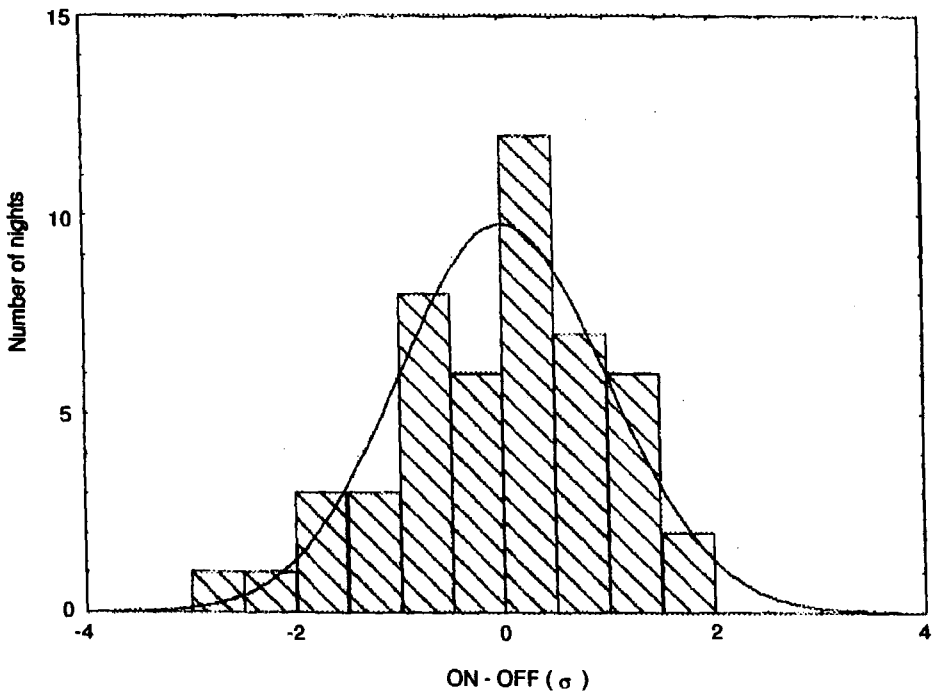

Figure 6.15: The distribution of significances of the daily excesses for PKS 0548-322, PKS 2005-489, PKS 2155-304 and PKS 1514-24. The solid curve is the expected statistical distribution. The mean of this distribution is $-0.046 \pm 0.146\,\sigma$.

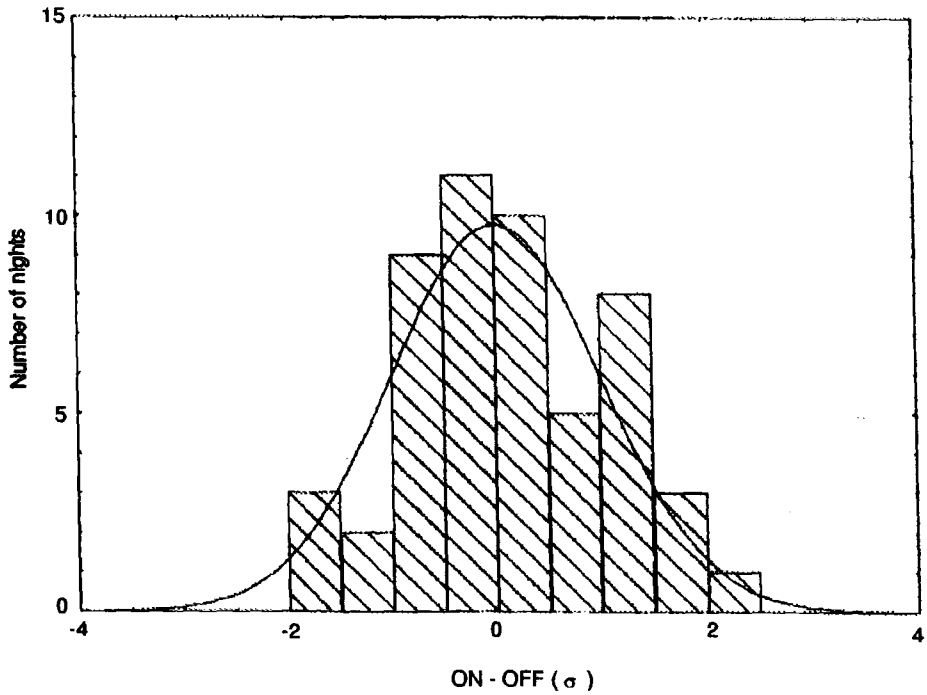

Figure 6.16: The distribution of the daily significances for events with values of the *Camera Sum* parameter between 200 and 800. The majority of these events are assumed to originate from low energy primary particles. The solid curve is the expected statistical distribution. The mean of this distribution is $0.122 \pm 0.137\,\sigma$.

assumed that the majority of these small events have originated from low energy primary particles (typically less than 500 GeV). They are defined as having values of the *Camera Sum* parameter between 200→800. The distribution of the ON-OFF significances produced from each observation for the 'small' selected events is shown in Figure 6.16. No evidence for γ-ray emission in this lowest *Camera Sum* size band is observed.

Chapter 7

Summary and Future Work

7.1 Summary

The field of VHE γ-ray astronomy has progressed dramatically since the detection of the Crab Nebula using imaging techniques developed by the Whipple Collaboration during the late 1980's. This detection allowed large improvements in background rejection techniques to be developed. The launch of the Compton Gamma Ray Observatory in 1991 provided a range of highly sensitive experiments which have bridged the gap between X-ray and VHE γ-ray observations. The EGRET experiment onboard this satellite revealed that a large number of active galactic nuclei, in particular blazars, are strong sources of MeV and GeV γ-rays. These observations stimulated a new observing philosophy within ground based γ-ray groups who had historically based their observations around galactic objects.

Four objects have currently been detected using imaging techniques with significances greater than 10σ. These sources have also been independently confirmed by observations made with one or more atmospheric Čerenkov telescopes. Of these four VHE γ-ray sources, two are extragalactic objects, Mrk 421 and Mrk 501, both of which have shown dramatic flaring activity on timescales of minutes to months. These observations, especially when in conjunction with a multiwavelength observa-

tion campaign, have been providing vital information regarding both the production mechanisms and physical environments within these objects.

The University of Durham γ-ray group constructed the Mark 6 atmospheric Čerenkov telescope in 1994. This telescope is designed to combine a low energy threshold with a high resolution imaging capability. A set of moment parameter selections have been developed to dramically enhance any γ-ray signal. This has resulted in a 5σ detection of the pulsar PSR 1706-44. The flux determined from PSR 1706-44 is in agreement with that expected from recent EGRET and CANGAROO observations (see Chadwick *et al.*, 1997).

The recent interest in TeV γ-ray observations of AGNs led the Durham group to observe a number of southern hemisphere blazars, producing 141 hours of data suitable for analysis (equivalent to $4 \rightarrow 5$ months observing with the typical Mark 6 duty cycle); PKS 0548-322, PKS 1514-24, PKS 2005-489 and PKS 2155-304. These objects were chosen on the basis of the detections made in the northern hemisphere and recent theoretical considerations. The results from these observations have been presented within this thesis. There is no evidence for any γ-ray emission, either as a steady flux or in the form of flares, from any of these objects. It should be noted that the X-ray data which are contemporaneous with the Mark 6 observations of these objects also do not show any evidence for variability. Flux predictions have been calculated for three of these blazars, based on data obtained from radio through to high energy γ-rays and in conjunction with a model of the intergalactic infrared background. The upper limits produced for PKS 0548-322 and PKS 2005-489 are in agreement with those predicted. The upper limit produced for PKS 2155-304 is very close to that predicted and may rule out values of the intergalactic infrared background significantly lower than those used within the model.

7.2 Future Work

7.2.1 Southern Hemisphere Blazars

Although no southern hemisphere blazars have shown any evidence for VHE γ-ray emission, the upper limits produced within this thesis are close to the predicted fluxes. The increased exposure time and the possibility of observing flaring activity during new observations, suggest that a detection may be possible in the near future. The daily X-ray flux measurements produced by the RXTE satellite of X-ray selected BL Lacs will be an invaluable aid in determining the current emission state of an object (e.g. quiescent or active). The X-ray and TeV flux correlations have been a key feature of the recent flaring activity from Mrk 501 during 1997. The Durham group is partaking in a multiwavelength observation campaign on the object PKS 2005-489 during 1998. This will involve thirteen ground based facilities and the ASCA, SAX, XTE, EUVE and CGRO satellites.

A VHE γ-ray detection of the bright BL Lac PKS 2155-304, would enable an accurate estimate of the intergalactic infrared background to be obtained. This is due to PKS 2155-304 being at a considerably higher redshift than the two BL Lacs detected in the northern hemisphere.

7.2.2 PSR 1706-44

Further observations have recently been obtained with the Mark 6 telescope of PSR 1706-44. The analysis of this data is currently being undertaking by members of the Durham group and the results will be presented elsewhere. The parameter selections derived from the data obtained during the 1996 observing season will be applied *a priori* to any new datasets. This allows the full statistical significance of the new observations to be obtained. It is important that this object is observed as a matter of high priority. The experience with the Crab Nebula in the northern hemisphere suggests that an accurate knowledge of a 'standard candle' is important

in determining correct flux measurements and source spectra.

7.2.3 Simulations

Further work is still needed to refine the simulations of the Mark 6 telescope, as there are a number of inconsistencies between simulated and real data. This is particularly obvious for the parameter *length*, where the mean of the recorded parameter distribution is larger than that produced by simulations. The 4-fold temporal trigger has yet to be implemented within the simulation code (at present the standard 3-fold trigger is used). This will affect the moment parameter distributions, but is unlikely to change the calculated Mark 6 threshold energy. This is due to the change from the 3-fold to the 4-fold temporal trigger only affecting the smallest recorded events. These events are well below the peak in the differential flux spectrum (see Figure 3.12). An accurate multidimensional representation of the Mark 6 central mirror's point spread function also needs to be implemented within the simulation code. At present it is approximated by a 2-dimensional Gaussian.

7.2.4 Hardware Upgrades

Various hardware upgrades are planned for the Mark 6 telescope during the next two to three years. These include, in order of implementation (the PMT upgrades are shown in Figure 7.1):

1. Replace the 2 inch 'guard ring' PMTs within the central detector package with 78 one inch PMTs, forming two extra complete rings. This will provide far greater information concerning images falling close to the edge of the present high resolution area of the central detector package. This is important for determining the parameter *alpha* for such events.
2. Replace the central Mark 6 flux collector with a new mirror of the same construction but with an improved point spread function. Heating elements are to be placed within the aluminium to stop water freezing on

the mirror surfaces during winter months. Following this the left and right flux collectors will also be replaced.

3. Replace the 19 hexagonal PMTs in the left and right detector packages with 91 one inch PMTs.

4. Replace the 169 element central detector package with 500 elements, each with a pitch angle of 0.1°.

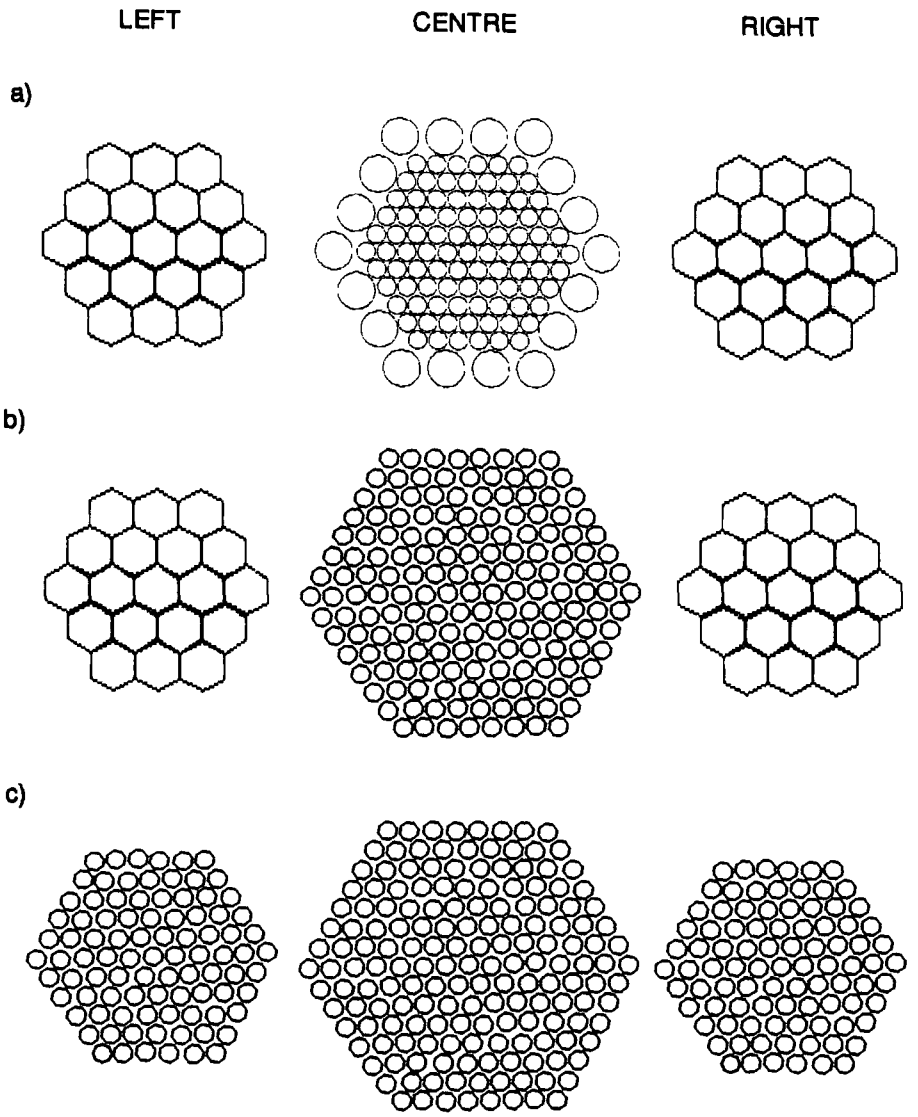

Figure 7.1: The PMT upgrades. a) Current configuration; b) Replacing the 2 inch 'guard ring' PMTs within the central detector package with 78 one inch PMTs; c) Replace the 19 hexagonal PMTs in the left and right detector packages with 91 one inch PMTs.

Chapter 8

References

Aharonian, F., *et al.*, *J. Phys. G.:Nucl. Part. Phys*, **21**, 419 (1995).

Aharonian, F., *et al.*, *astro-ph/9706019.*

Aiso, S., *et al.*, *Proc. of the 25th ICRC*, Durban, **5**, 373 (1997).

Antonucci, R., and Ulvestad, J., *Astrophys. J.*, **294**, 158 (1985).

Antonucci, R., *Ann. Rev. Astron. Astrophys.*, **31**, 473 (1993).

Barr, P., *et al.*, *Astrophys. J.*, **324**, L11 (1988).

Barthel, P.D., *Astrophys. J.*, **336**, 606 (1989).

Barrau, A., *et al.*, *Proc. of the 25th ICRC*, Durban, **3**, 253 (1997).

Biller, S.D., *et al.*, *Astrophys. J.*, **445**, 227 (1995).

Blackett, P.M.S., *Emission Spectra of the Night Sky and Aurora*, Rep. Gassiot Comm. of the Roy. Soc., 34 (1948).

Blandford, R.D., *A.I.P. Conf. Proc.*, **280**, 533 (1993).

Bloom, S.D. and Marscher A.P., *Astrophys. J.*, **461**, 657 (1996).

Blumenthal, G.R., and Gould, R.J., *Rev. Mod. Phys.*, **42**, 238 (1970).

Bowden, C.C.G., *Ph.D. Thesis, University of Durham* (1993).

Bradbury, S.M., *et al.*, *Astron. Astrophys.*, **320**, L5 (1997).

Brunner, H., *et al.*, *Astron. Astrophys.*, **287**, 436 (1994).

Buckley, J.M., *et al.*, *Astrophys. J.*, **472**, L9 (1996).

Cameron, R.A., *et al.*, *The Compton Observatory Science Workshop*, NASA, Wash-

ington, 3 (1992).

Carini, M.T., *et al.*, *Astronomical J.*, **101**, 1196 (1991).

Carramiñana *et al.*, *Astron. Astrophys.*, **228**, 327 (1990).

Carramiñana, A., *Ph.D. Thesis, University of Durham* (1991).

Catanese, M., *et al.*, *Towards a Major Atmosphereic Čerenkov Telescope 4* (Ed. Cresti, M.), Padova, 335 (1995).

Catanese, M., *et al.*, *Proc. of the 25th ICRC*, Durban, **3**, 277 (1997).

Cawley, M.F., *Towards a Major Atmospheric Cherenkov Detector 2*, 176 (1994).

Cawley, M.F. and Weekes, T.C., *Exp. Ast.*, **6**, 7 (1995).

Chadwick, P.M., *Ph.D. Thesis, University of Durham* (1987).

Chadwick, P.M., *et al.*, *Towards a Major Atmosphereic Čerenkov Telescope 4* (Ed. Cresti, M.), Padova, 301 (1995).

Chadwick, P.M., *et al.*, *Space Sci. Rev.*, **75**, 153 (1996).

Chadwick, P.M., *et al.*, *In Preparation* (1997).

Čerenkov, P.A., *Phys. Rev.*, **52**, 378 (1934).

Chudakov, A.E., *et al.*, *Transl. Consultants Bureau, P.N.Lebedev Phys. Inst.*, **26**, 99 (1965).

Cocconi, G., *Proc. of the 7th ICRC*, Moscow, **2**, 309 (1959).

Dar, A. and Laor, L., *Astrophys. J.*, **478**, L5 (1997).

Daum, A., *et al.*, *astro-ph/9704098* (1997)

Dawson, B.R., *Ph.D. Thesis*, University of Adelaide (1985).

de Jager, O.C., *et al.*, *Nature*, **369**, 294 (1994).

Dermer, C.D., *et al.*, *Astron. Astrophys.*, **256**, L27 (1992).

Dickinson, J.E., *Ph.D. Thesis, University of Durham* (1995).

Edelson, R., *et al.*, *Astrophys. J.*, **438**, 120 (1995).

Falomo, R., *et al.*, *Astrophys. J.*, **318**, L39 (1987).

Fazio, G.G., *et al.*, *Astrophys. J.*, **175**, L117 (1972).

Fegan, D.J., *Towards a Major Atmospheric Cherenkov Detector 1*, 3 (1992).

Fegan, D.J., *et al.*, *Towards a Major Atmospheric Cherenkov Detector 3*, 149 (1995).

Fichtel, C.E., *et al.*, *Astrophys. J. Supp..*, **94**, 551 (1994).

Fichtel, C., *Astron. Astrophys. Supp.*, **120**, 23 (1996).

Frank, I.M. and Tamm, I.G., *Dokl. Acad. Nauk.*, **14**, 109 (1937).

Gaidos, J.A., *et al.*, *Nature*, **383**, 319 (1996).

Gaisser, T.K., *Cosmic Rays and Particle Physics*, Cambridge University Press, Cambridge (1990).

Galbraith, W., and Jelly, J.V., *Nature*, **171**, 349 (1952).

Giommi, P., and Padovani, P., *MNRAS*, **268**, 51 (1994).

Gibson, A.I., *et al.*, *Nature*, **296**, 883 (1982).

Giommi, P., *et al.*, *Astron. Astrophys. Sup. Ser.*, **109**, 267 (1995).

Gould, R.J., *Phys. Rev. Lett.*, **15**, 511 (1965).

Gould, R.J. and Schréder, G.P., *Phys. Rev. Lett.*, **16**, 252 (1966).

Greisen, K., *Progress in Elementary Particles and Cosmic Ray Physics* (Ed. J.G.Wilson), North Holland (1956).

Greisen, K., *Ann. Rev. Nucl. Sci.*, **10**, 93 (1960).

Grindlay, J.E., *et al.*, *Astrophys. J.*, **197**, L9 (1975).

Hartman, R.C., *et al.*, *Astrophys. J.*, **461**, 698 (1996).

Hauser, M.G., *A.I.P. Conf. Proc.*, **222**, 161 (1991).

Heitler, W., *Quantum Theory of Radiation*, Oxford University Press, Oxford (1948).

den Herder J.W., *et al.*, *The Compton Observatory Science Workshop*, NASA, Washington, 85 (1992).

Hess, V.F., *Phys. Zeits.*, **12**, 998 (1912).

Hewitt, A. and Burbidge, G., *Astrophys. J. Sup. Ser.*, **87**, 451 (1993).

Hillas, A.M., *J. Phys. G.:Nucl. Part. Phys*, **8**, 1475 (1982).

Hillas, A.M., *Proc. of the 19^{th} ICRC*, La Jolla, **3**, 445 (1985).

Hillas, A.M. and Patterson, J.R., *Very High Energy γ-ray Astronomy* (Ed. Turver, K.E.), D.Reidel, Dordecht, 243 (1987).

Hillas, A.M., *Space Sci. Rev.*, **75**, 17 (1996a).

Hillas, A.M., *Privite communication; Talk presented at the Whipple collaboration meeting (University of Leeds, 1996b).*

Holder, J., *Ph.D. Thesis, University of Durham* (1997).

Inoue, S. and Takahara, F., *Astrophys. J.*, **463**, 555 (1996).

Jelley, J.V., *Čerenkov Radiation and its Applications*, Pergaman Press, London

(1958).

Jones, F.C., *Phys. Rev.*, **167**, 1159 (1968).

Kanbach, G., *et al.*, *Space Sci. Rev.*, **49**, 69 (1988).

Kaspi, V.M., *et al.*, *GRO/Radio Timing Database*, Princeton University (1995).

Kerrick, A.D., *et al.*, *Astrophys. J.*, **438**, L59 (1995a).

Kerrick, A.D., *et al.*, *Astrophys. J.*, **452**, 588 (1995b).

Kifune, T., *et al.*, *Towards a Major Atmospheric Čerenkov Telescope 2* (Ed. Weekes, T.C.), Calgory, 39 (1993).

Kifune, T., *et al.*, *Astrophys. J.*, **438**, L91 (1995).

Kniffen, D.A., *et al.*, *Astrophys. J.*, **411**, 133 (1993).

Köhler, C., *et al.*, *Astropart. Phys.*, **6**, 77 (1996).

Lamer, G., *et al.*, *Astron. Astrophys.*, **311**, L384 (1996).

Leahy, D.A., *et al.*, *Astrophys. J.*, **272**, 256 (1983).

Ledded, J.E. and O'Dell, S.L., *Astrophys. J.*, **298**, 630 (1985).

Lin, Y.C., *et al.*, *Astrophys. J.*, **401**, L61 (1992).

Lin, Y.C., *et al.*, *Astron. Astrophys. Sup. Ser.*, **120**, 499 (1996).

Lin, Y.C., *et al.*, *Astrophys. J.*, **476**, L11 (1997).

Longair, M.S., *High Energy Astrophysics* Vol. 1 (2^{nd} Ed.), Cambridge University Press, Cambridge (1992).

Longair, M.S., *High Energy Astrophysics* Vol. 2 (2^{nd} Ed.), Cambridge University Press, Cambridge (1994).

Maccagni *et al.*, *Astrophys. J.*, **273**, 70 (1983).

Macomb, P.J., *et al.*, *Astrophys. J.*, **449**, L99 (1995).

Mannheim, K. and Biermann, P.L., *Astron. Astrophys.*, **253**, L21 (1992).

Mannheim, K., *et al.*, *Astron. Astrophys*, **315**, 77 (1996).

Mannings, V., *Ph.D. Thesis, University of Durham* (1990).

Marscher, A.P. and Bloom, S.D., *Proc. Compton Obs. Sci. Workshop*, **304**, 572 (1993).

Maraschi, L., *et al.*, *Astrophys. J.*, **397**, L5 (1992).

Maraschi, L., *et al.*, *Astrophys. J.*, **435**, L91 (1994).

Marshall, H.L., *et al.*, *Astrophys. J.*, **439**, 90 (1995).

Mattox, J. *et al.*, *Astrophys. J.*, **476**, 692 (1997a).

Mattox, J.R., *et al.*, *Astrophys. J.*, **481**, 95 (1997b).

McEnery, J.E., *et al.*, *Proc. of the 25th ICRC*, Durban, **3**, 257 (1997).

Morris, S.L., *et al.*, *Astrophys. J.*, **380**, 49 (1991).

Nel, H.I., *et al.*, *Astrophys. J.*, **418**, 836 (1993).

Nolan, P.L., *et al.*, *Astrophys. J.*, **409**, 697 (1993).

Orford, K.J., *Astropart. Phys.*, **4**, 235 (1996).

Padovani, P. and Urry, C.M., *Astrophys. J.*, **356**, 75 (1990).

Padovani, P. and Giommi, P., *MNRAS.*, **279**, 526 (1996).

Petry, D., *et al.*, *Astron. Astrophys.*, **311**, L13 (1996).

Punch, M., *et al.*, *Nature*, **358**, 477 (1992).

Punch, M., *Ph.D. Thesis, University College Dublin* (1993).

Quinn, J., *et al.*, *Astrophys. J.*, **456**, L83 (1996).

Quinn, J., *et al.*, *Proc. of the 25th ICRC*, Durban, **3**, 249 (1997).

Ramana Murthy, P.V., and Wolfendale, A.W., *Gamma Ray Astronomy*, Cambridge University Press, Cambridge (1986).

Roberts, I.D., *Ph.D. Thesis, University of Durham* (1997a).

Roberts, M.D., *et al.*, *Proc. of the 25th ICRC*, Durban, **3**, 281 (1997b).

Robson, I., *Active Galactic Nuclei*, Wiley (1996).

Rossi, B., *High Energy Particles*, Prentice-Hall Inc. (1952).

Salamon, M.H., *et al.*, *Astrophys. J*, **423**, L1 (1994).

Sambruna, R.M., *et al.*, *Astrophys. J.*, **449**, 567 (1995).

Sambruna, R.M., *et al.*, *Astrophys. J.*, **463**, 444 (1996).

Schubnell, M.S., *et al.*, *Astrophys. J.*, **460**, 644 (1996).

Schubnell, M.S., *To appear in the Proc. 4th Comp. Sym.*, Williamsburg (1997).

Shaw, S.E., *Private Commumication* (1997).

Shklovsky, I.S., *Dokl. Akad. Nauk. SSSR*, **90**, 983 (1953).

Sikora, M., *Astrophys. J. Sup. Ser.*, **90**, 923 (1994a).

Sikora, M., *et al.*, *Astrophys. J.*, **421**, 153 (1994b).

Simpson, J.A., *et al.*, *Phys. Rev.*, **90**, 934 (1953).

Standish, E.M., *Astron. Astrophys.*, **114**, 297 (1982).

Stanev, T. and Franceschini, A., *Submitted to Astrophys. J. Lett.* (1997)

Stecker, F.W., *Cosmic Gamma Rays*, Mono Book Corp., Baltimore (1971).

Stecker, F.W., *et al.*, *Astrophys. J.*, **390**, L49 (1992).

Stecker, F.W., *et al.*, *Astrophys. J.*, **415**, L71 (1993).

Stecker, F., *et al.*, *Astrophys. J.*, **473**, L75 (1996).

Stecker, F.W. and de Jager, O.C., *Astrophys. J.*, **476**, 712 (1997).

Stecker, F.W. and Salamon, M.H., *Proc. of the 25th ICRC*, Durban, **3**, 317 (1997).

Stickel, M., *et al.*, *Astrophys. J*, **374**, 431 (1991).

Sturrock, P.A., *Astrophys. J.*, **164**, 529 (1971).

Swanenburg, B.N., *et al.*, *Nature*, **275**, 298 (1978).

Takahashi, T., *et al.*, *Astrophys. J.*, **470**, L89 (1996).

Tashiro, M., *et al.*, *PASJ*, **47**, 131 (1995).

Thompson, D.J., *Astrophys. J. Supp..*, **101**, 259 (1995).

Treves, A., *et al.*, *astro-ph/9702084*.

Urry, C.M., *et al. Astrophys. J.*, **382**, 501 (1991).

Urry, C.M. and Padovani, P., *Publ. Astr. Soc. Pacific.*, **107**, 803 (1995).

Urry, C.M., *astro-ph/9609023*.

Vacanti, G., *et al.*, *Astrophys. J.*, **377**, 467 (1991).

Vestrand, W.T., *et al.*, *Astrophys. J.*, **454**, L93 (1995).

Wall, J.V., *et al.*, *Australian J. Phys., Astrophys. Suppl.*, **34**, 55 (1975).

Wall, J.V., *et al.*, *MNRAS*, **219**, 23 (1986).

Weekes, T.C. and Turver, K.E., *Proc. of the 12th Eslab Symp.*, Frascati, ESA SP-124, 279 (1977).

Weekes, T., *Private Commumication* (1985).

Weekes, T.C., *et al.*, *Astrophys. J.*, **342**, 379 (1989).

Weekes, T.C., *Space Sci. Rev.*. **75**, 1 (1996).

Westfall, G.D., *et al.*, *Phys. Rev. C.*, **19**, 1309 (1979).